Comfort-oriented control for forecast-free building demand response

Zur Erlangung des akademischen Grades einer

DOKTORIN DER INGENIEURWISSENSCHAFTEN (Dr.-Ing.)

von der KIT-Fakultät für Maschinenbau des
Karlsruher Instituts für Technologie (KIT)

angenommene

DISSERTATION

von

M.Sc. Jovana Vučinić
geb. Kovačević

Tag der mündlichen Prüfung:	13.07.2026
Hauptreferent:	Prof. Dr. Veit Hagenmeyer
Korreferent:	Prof. Dipl.-Ing. Andreas Wagner

Abstract

Integrating renewable energy systems into the energy supply requires improving the alignment between energy generation and demand, given the inherent intermittency of renewable energy generation. Enhancing demand-side flexibility through controllable loads and energy storage systems is therefore essential. As the building sector accounts for a significant share of global energy consumption, the electrification of thermal building loads provides a substantial opportunity for energy flexibility. This dissertation contributes to two key areas of building energy flexibility: building energy modeling and advanced control strategies for demand response. In the domain of building energy modeling, this thesis investigates uncertainties in gray-box thermal building models and proposes an ensemble modeling approach to account for variations in occupant behavior. The proposed approach achieves improved indoor air temperature forecasting accuracy across all rooms. Furthermore, motivated by the advantages of simplified models, the impact of model complexity reduction on the dynamic behavior of building heating system is analyzed. Using a real-world facility as a case study, a detailed model is developed, followed by a systematic assessment of model simplifications. The results demonstrate that increased model complexity does not necessarily lead to improved representation of real-world system behavior. The second part of the dissertation investigates the potential of forecast- and model-free fuzzy logic control strategies for demand response. Two fuzzy logic controllers targeting cost and comfort optimization are developed and evaluated in a simulation framework. Based on the performance analysis and identified improvement potential, a refined fuzzy logic controller is derived and subsequently validated in a real-world experimental case study. The results show that the proposed approach enhances building flexibility compared to baseline control. The case study is further extended to a building equipped with distributed energy resources, including a battery energy storage system and hydrogen storage. Comparative evaluations against rule-based and model predictive control demonstrate that the fuzzy logic controller achieves better performance than the rule-based controller while maintaining low input and modeling requirements, unlike the model predictive control approach.

Kurzfassung

Die Integration erneuerbarer Energiesysteme in die Energieversorgung erfordert angesichts der natürlichen Schwankungen der Erzeugung erneuerbarer Energien eine bessere Abstimmung zwischen Energieerzeugung und -nachfrage. Die Verbesserung der Flexibilität auf der Nachfrageseite durch steuerbare Lasten und Energiespeichersysteme ist daher entscheidend. Da der Gebäudesektor einen erheblichen Anteil am weltweiten Energieverbrauch ausmacht, bietet die Elektrifizierung der thermischen Gebäudelasten erhebliche Möglichkeiten zur Steigerung der Energieflexibilität. Diese Dissertation leistet einen Beitrag zu zwei Schlüsselbereichen der Energieflexibilität im Gebäudebereich: der Gebäudemodellierung und den fortschrittlichen Regelungsstrategien für die Laststeuerung. Im Bereich der Gebäudeenergiemodellierung untersucht diese Arbeit Unsicherheiten in thermischen Graubox-Gebäudemodellen und schlägt einen Ensemble-Modellierungsansatz vor, um Schwankungen im Nutzerverhalten zu berücksichtigen. Der vorgeschlagene Ansatz verbessert die Vorhersagegenauigkeit der Lufttemperatur in allen Räumen. Darüber hinaus wird, motiviert durch die Vorteile vereinfachter Modelle, der Einfluss einer Reduzierung der Modellkomplexität auf das dynamische Verhalten von Gebäudeheizungssystemen analysiert. Anhand einer realen Anlage als Fallstudie wird ein detailliertes Modell entwickelt, gefolgt von einer systematischen Bewertung von Modellvereinfachungen. Die Ergebnisse zeigen, dass eine erhöhte Modellkomplexität nicht zwangsläufig zu einer besseren Darstellung des realen Systemverhaltens führt. Der zweite Teil der Dissertation untersucht das Potenzial prognose- und modellfreier Fuzzy-Logik-Regelungsstrategien für die Laststeuerung. Zwei Fuzzy-Logik-Regler, die auf Kosten- und Komfortoptimierung abzielen, werden entwickelt und in einem Simulationsumfeld bewertet. Auf der Grundlage der Leistungsanalyse und des identifizierten Verbesserungspotenzials wird ein verfeinerter Fuzzy-Logik-Regler abgeleitet und anschließend in einer praxisnahen experimentellen Fallstudie validiert. Die Ergebnisse zeigen, dass der vorgeschlagene Ansatz die Flexibilität eines Gebäudes im Vergleich zur Basisregelung erhöht. Die Fallstudie wird auf ein Gebäude ausgeweitet, das mit dezentralen Energiequellen ausgestattet ist, darunter ein Batteriespeichersystem und ein Wasserstoffspeicher. Vergleichende Bewertungen mit regelbasierter und modellprädiktiver Regelung zeigen, dass der Fuzzy-Logik-Regler im Vergleich zum regelbasierten Regler eine bessere Leistung liefert und insbesondere im Gegensatz zur modellprädiktiven Regelung geringere Anforderungen an die Eingabedaten und die Modellierung aufweist.

Acknowledgments

This dissertation is the result of research conducted at the Institute for Automation and Applied Informatics (IAI) at the Karlsruhe Institute of Technology. It would not have been possible without the help of several colleagues, whom I would like to acknowledge and thank.

First, I want to thank my supervisors: Prof. Veit Hagenmeyer, for the great support, guidance, and feedback given throughout the years. Hüseyin K. Çakmak for a constant wellspring of ideas, excellent support and fast feedback, and Prof. Jörg Matthes for his constructive feedback and ideas. In addition, I would like to thank Prof. Veit Hagenmeyer, Hüseyin K. Çakmak, and Andreas Hofmann for giving me the opportunity to conduct my dissertation research at the IAI. My sincere thanks to Prof. Andreas Wagner for being a reviewer of my dissertation and for our insightful discussions about my work.

I would like to thank my colleagues and IAI employees Burak Dindar, Alexander Kocher, Anne-Christin Süß, Erfan Tajalli-Ardekani, Johannes Galenzowski, Moritz Weber, Haozhen Cheng, Fatih Tüzün, Mostafa Mekky, Jannik Sidler, Chang Li, Frederic Linde, Simon Waczowicz, Luigi Spatafora, Prof. Ralf Mikut, Marina Djordjevic, and Bernadette Lehmann for support, exciting discussions, teamwork, and off-work talks. Special thanks go to Moritz Frahm, who introduced me to the topic of building energy control. I am also particularly grateful to Felix Langner, a colleague whose influence on my work was substantial and whose support made the dissertation process much easier. Thank you for the great discussions, insightful feedback, and numerous philosophical walks.

I truly appreciate meeting Prof. Mihailo Jovanović, whose sincere love for science inspired me to pursue a PhD path. Finally, I would like to thank my family, Dragan, Sladjana, Milica, Pavle, Milijana, Ivan, Marija, Luka, Vuk, and Lav for their continued support through both challenges and successes, and for always being by my side. Most of all, I am deeply grateful to my husband, Veljko Vučinić, for his unwavering support during tough times and for encouraging me throughout the dissertation process. I am especially thankful for his critical thinking and the valuable discussions we had on the dissertation topics.

Preface

"As complexity rises, precise statements lose meaning and meaningful statements lose precision."

Lotfi A. Zadeh

Contents

1 Introduction

Global warming is widely attributed to the increasing concentrations of Carbon Dioxide (CO_2) and other greenhouse gases emitted in the atmosphere. The transition away from fossil fuels toward zero-carbon energy systems on the energy supply side is driven by the large-scale integration of renewable energy technologies, including wind turbines and Photovoltaics (PV) systems. A key challenge associated with weather-dependent Renewable Energy Sources (RES) is their inherent supply intermittency. As a result, system flexibility must increasingly be provided by the demand side. This shift changes the operation of the energy systems, whereby electricity generation is no longer continuously adjusted to meet demand; instead, variability in generation from RES is balanced through a combination of flexible demand and energy storage technologies. From the demand-side perspective, the green transition is characterized by widespread electrification across major end-use sectors. In the building sector, this involves replacing conventional gas- and oil-based heating systems with electrified heating technologies, while in the transport sector, it is reflected in the increasing adoption of electric vehicles, gradually displacing traditional internal combustion engine vehicles.

Buildings have been identified as significant energy consumers, placing considerable pressure on modern grids. In particular, space heating and the provision of Domestic Hot Water (DHW) account for nearly half of global building-related energy consumption (IEA 2025b). In response to this green transition, low-carbon heating technologies are increasingly deployed, driven by continuous efficiency improvements and declining investment costs. While the energy demand of an individual household has a negligible impact on overall grid operations, the collective behavior of many buildings can significantly affect aggregated consumption by enabling the flexible energy utilization. In this context, the International Energy Agency (IEA) defines building energy flexibility as “the ability to manage its demand and supply according to local climate conditions, user needs, and energy network requirements”, (IEA 2025a, Li et al. 2022a). Building energy flexibility can be realized through several complementary strategies. These include (i) the integration of on-site, small-scale RESs such as PV and wind turbines; (ii) the intelligent scheduling of Heating Ventilation and Air Conditioning (HVAC) systems and the management of flexible electrical loads; and (iii) the deployment of short- and long-term energy storage solutions. Figure 1.1 presents an overview of building supply and demand interactions in a distribution-level electricity grid with integrated RES.

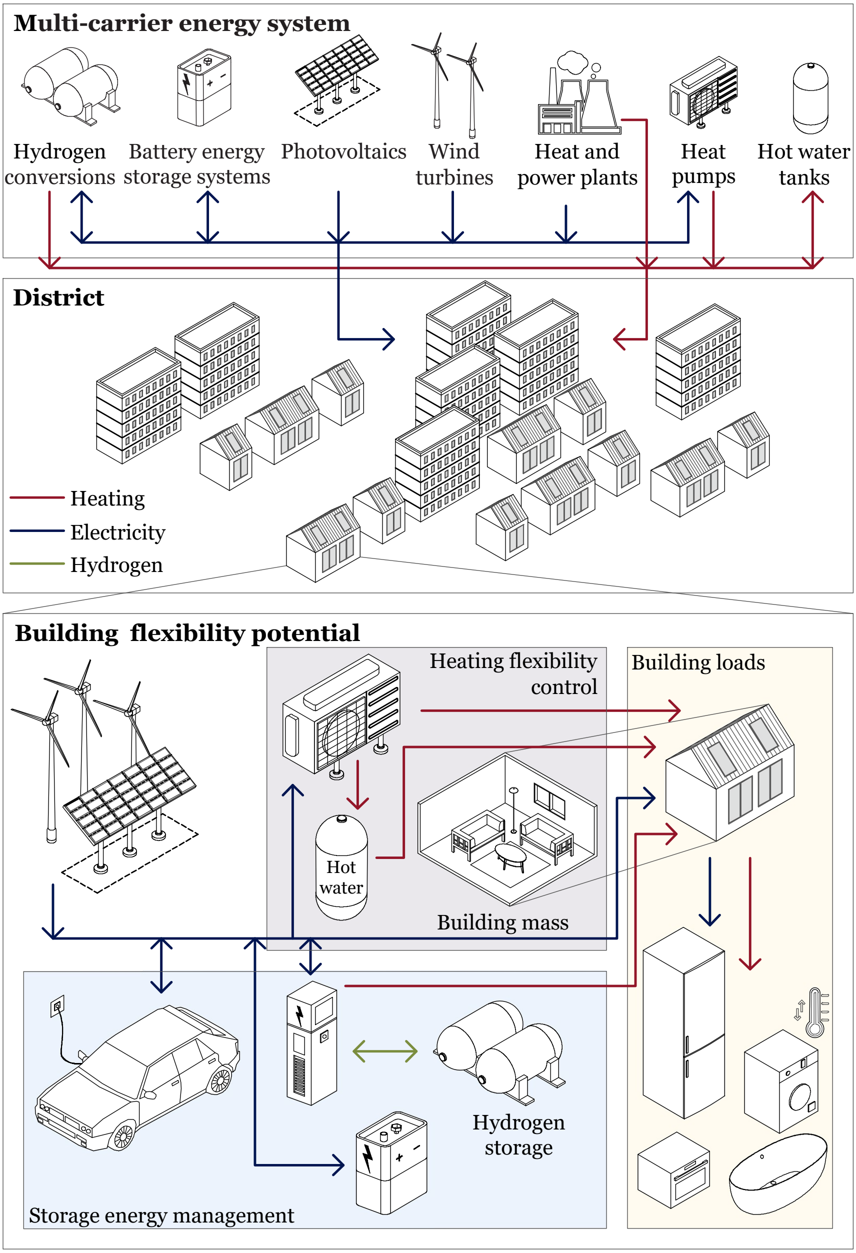

Figure 1.1: The energy flexibility on the distribution grid and building level. The figure is inspired by Li et al. (2022a).

To unlock energy flexibility, advanced control strategies that account for external signals, such as electricity prices, are required to optimize resource management. Beyond optimization-based strategies, practical deployment of control solutions requires approaches that are robust, interpretable, and compatible with the technical and operational constraints of real buildings. Advanced control of space heating can utilize building thermal mass as an auxiliary storage system without additional financial costs, enabling load shifting, for example, preheating when grid conditions are favorable and reducing heating during unfavorable periods.

1.1 Literature review

This subsection comprises two parts: a review of building energy modeling in Section 1.1.1, followed by an overview of advanced control strategies for demand response in buildings with distributed energy resources in Section 1.1.2. Based on the reviewed literature, the research gaps are identified and summarized.

1.1.1 Building energy modeling

Control algorithms for building energy systems are predominantly evaluated in simulation environments (Hu and You 2023, Hua et al. 2024, Keshtkar et al. 2015, Talebi and Hatami 2020), rather than through real-world experiments (Knudsen et al. 2021, Van Puyvelde et al. 2024). In this context, the accurate dynamic representation of building energy models may be overlooked, which can lead to misleading conclusions. A critical requirement for deriving reliable insights from simulations is model validation. While highly detailed models tend to be computationally intensive, they do not necessarily guarantee better representation of real-world systems (Robinson 2023). Conversely, overly simplified models may fail to capture essential operational characteristics (Zhu et al. 2025). Furthermore, variations in model assumptions and simplifications can lead to inconsistent results among various studies (Wang and Dong 2024). Therefore, achieving an optimal balance between model complexity and computational costs is critical.

Reduced-order thermal building modeling

Reduced-order gray-box thermal building models encompass a wide range of simplified physical representations (Drgoňa et al. 2020). Their parameters are typically identified from measurement data or derived from detailed white-box building models. A common representation of these models uses an Resistance-Capacitance (RC) analogy, where R denotes thermal resistance, and

C represents thermal capacitance, which stores thermal energy (detailed in Chapter 2). The complexity of the models increases as the number of R and C components increases. These models are typically used to develop and test various model-based or forecast-free algorithms (Joe 2022, De Coninck et al. 2016).

Parameter identification of reduced-order thermal building models can be affected by disturbances such as ambient temperature, solar radiation, and occupant-related activities. Several studies have highlighted the challenges associated with the reduced-order building modeling approach (Li et al. 2021b, Broholt et al. 2022). Li et al. (2021b) emphasize that the structure and development process of gray-box reduced order models often lack clarity. They also state that the classification of gray-box models is inconsistent, as they may represent a single component (e.g., a wall or window), a single zone, or multiple zones. Broholt et al. (2022) address the issue of predictive robustness, showing that gray-box models calibrated on data from specific months may perform poorly when used to forecast thermal behavior across the entire year. Their comparison of gray- and black-box models reveals that gray-box models offer slightly better predictive performance. Hybrid modeling approaches combining simplified gray- and black-box models have been explored to enhance forecasting accuracy (Gray and Schmidt 2018, Cui et al. 2019). Gray and Schmidt (2018) compare pure gray- and black-box models with a hybrid approach using gray-box models and Gaussian process models, achieving the improvements in temperature and energy predictions. On the other hand, in their comparison, Cui et al. (2019) find that integrating gray-box models with extreme gradient boosting yields the best performance. Michalak (2017) improves gray-box models by using a time-variant state-space system that updates parameters hourly based on simulation data.

Several studies investigate optimal gray-box model structures (Harb et al. 2016, Klanatsky et al. 2023). Harb et al. (2016) compare multiple RC configurations, identifying the 4R2C model as favorable for predicting indoor temperature in occupied buildings. Furthermore, Klanatsky et al. (2023) incorporate a thermal building mass and glass facades into gray-box models, achieving a mean absolute error of 0.25 °C with a 3R3C structure. They introduce a startup phase to initialize realistic states before parameter identification. Baasch et al. (2021) assess robustness to diverse building properties across different gray- and black-box model structures, finding deep learning methods most effective. Zhang et al. (2022) highlight oversimplified solar gain modeling in gray-box approaches and propose dynamic improvements to address forecasting limitations.

One challenge in gray-box thermal building modeling is integrating Occupants' Behavior (OB) patterns to enhance forecast accuracy. OB influences the indoor air temperature through interaction with building systems (e.g., windows, lighting, HVAC), through internal heat gains from occupants and their presence. Due to complexity of OB and limited understanding, it is often oversimplified in building energy models (Hong et al. 2017). Frahm et al. (2022b) demonstrate that the choice of identification periods (e.g., occupied vs. unoccupied) has a greater impact on forecast accuracy than model structure. In buildings, temporal variations in occupancy introduce forecast errors in time-invariant state-space models, which are inherently limited in capturing such dynamics. Evaluation of the literature review on the gray-box thermal building models poses the first research gap.

Research gap 1: The methodology for integrating occupants' patterns into reduced-order gray-box thermal building models, by considering the identification period based on these patterns, is missing.

Building heating system modeling

To fully explore the potential of HVAC systems and their operation in the building sector, validated models of the components used for heating (heat pumps, thermal energy storage, pumps, and related components) are essential. For instance, these models can serve as a basis for developing advanced control strategies in the heating sector. The control of heat pump operation, is often used to minimize electricity consumption, CO_2 emissions, or perform demand response while satisfying the heating and cooling requirements of a single building, its individual rooms, or a building cluster.

Chen et al. (2021) examine the system comprising a solar-assisted geothermal heat pump with two water storages for DHW and space heating in various configurations in a Modelica environment. Furthermore, Li et al. (2022b) develop the heat pump model for its sizing in residential utilization. Abugabbara et al. (2021) propose the Modelica simulation framework incorporating the heat pumps into a building substation to facilitate the decarbonization of district heating and cooling networks. In their work, Pieper et al. (2020) present a detailed heat pump model to examine various methods for Coefficient of Performance (COP) estimation at the district heating level. Furthermore, Maccarini et al. (2023) investigates the fifth generation of heating and cooling networks, using the Modelica model to assess sizing and energy performance.

When the heating sector is integrated with other energy carriers, such as gas and electricity, to facilitate comprehensive energy planning and optimization at the district or urban scale, the resulting multi-physics simulation process becomes inherently computationally demanding (Palensky et al. 2017). One of the significant challenges in numerical modeling is achieving an optimal balance between model complexity and accuracy, as discussed in Andrade-Cabrera et al. (2018). Furthermore, the relation between model complexity and utility using the Gaussian first law is studied by Li (2026). Based on the literature discussed above, the second research gap is formulated.

Research gap 2: The detailed analysis of the relationship between model complexity and accuracy in the context of multi-physics building heating systems is missing.

1.1.2 Building advanced control

Advanced Energy Management System (EMS) can integrate external signals, dynamic day-ahead electricity prices, feed-in tariffs, and meteorological data with or without forecasting. It can optimize operational strategies to leverage the flexibility and economic opportunities offered by modern electricity markets. This subsection is divided into two parts. First, the focus is on thermal control in buildings. Thereafter, the scope is expanded to EMS for buildings with distributed energy resources.

Building thermal control

Demand-side management is, according to Gellings (1985), "planning, implementation and monitoring of utility activities designed to influence the customers' use of electricity in ways it will produce desired changes in the utility's load shape, i.e., changes in the time pattern and magnitude of a utility's load". The load shaping strategies within the demand-side management can be differentiated temporarily: time of day, day of week, and seasonal, and by the shaping: (i) peak clipping, (ii) valley filling, (iii) load shifting, (iv) strategic conservation, (v) strategic load growth, (vi) flexible load shape (Gellings 1985).

Demand response programs, as a demand-side management category, actively involve end users to adjust their consumption over time based on grid conditions. Here, advanced control strategies play a critical role in enabling demand response and optimizing energy consumption. A key challenge in thermal control of electrified heating systems is establishing an optimal trade-off among energy consumption, occupant thermal comfort, and operational costs under dynamic electricity pricing. Preheating and precooling are methods that can contribute to load shifting and reduce operational costs while maintaining thermal comfort in buildings (Woo-Shem et al. 2023). Zhao et al. (2025) propose a temperature control framework for office buildings that integrates occupants' thermal tolerance into the demand response control strategy. Zeng et al. (2022) integrates advanced Rule Based Control (RBC) for precooling to improve thermal resilience of buildings during heat waves. On the other hand, Lu et al. (2021) develop the RBC for evaluating the cooling system energy flexibility by leveraging the thermal building mass. They indicate that the energy flexibility is sensitive to structural thermal capacity, internal heat gains, and the type of cooling terminals. The study reports that the proposed RBC achieves a 55.6% reduction in peak power demand compared to a conventional night set-back controller. Clauß et al.

(2024) demonstrate space-heating load shifting in a real-world experiment within an educational building, illustrating how simplified control algorithms can exploit building energy flexibility. The approach achieves a 50% reduction in energy consumption during peak hours, while maintaining daily energy use at a comparable level.

The most significant potential for savings lies with an Model Predictive Control (MPC), as it incorporates models and predicts future system behavior. Joe (2022) examines the potential for operational cost reduction through precooling, employing an MPC strategy and a gray-box model for controller performance evaluation. The study reports savings potential of 30% during the cooling season and 20% during the intermediate season, compared with the feedback controller. Golmohamadi et al. (2021) propose an economic MPC framework for enhancing power flexibility in a Danish case study, incorporating two forms of thermal flexibility: thermal building mass and thermal energy storage. The proposed controller ensures system flexibility and achieves up to 37% weekly energy savings. On the other hand, Zhang and Kummert (2021) conduct a comparative analysis of MPC and RBC strategies for demand response in a building equipped with the HVAC system, leveraging the thermal building mass to quantify and exploit energy flexibility. Although MPC can achieve near-optimal system performance, it relies on forecasting models and demand profiles, which in turn increase the need for sensors and additional equipment within the controlled building. Therefore, there is a need for control strategies that reduce reliance on additional equipment while enhancing the performance of industry-standard control approaches, such as RBCs (de Chalendar et al. 2024).

As a trade-off between simplicity and optimality, one solution is Fuzzy Logic Control (FLC), as an advanced form of RBC. The advantages of incorporating soft-computing techniques, such as fuzzy logic control (FLC), become evident with the increasing complexity of modern energy systems. Largely, because their functionality does not rely on predictive modeling. Moreover, the FLC is characterized by a robust capacity to handle uncertainty, imprecise information, and noisy inputs effectively (Kaabinejadian et al. 2025). Talebi and Hatami (2020) propose a fuzzy-based demand response control strategy for HVAC in cooling mode, allowing occupants the option to select their level of participation in demand response. The simulation study aims to reduce energy consumption, enhance thermal comfort, and lower HVAC operating costs. The findings indicate that users participating in demand response and prioritizing cost savings can reduce their expenses by 15% and lower energy consumption by 14%. Li et al. (2021a) conduct an experimental, real-world study for FLC of indoor air temperature, by including the occupants and their feedback through a wristband. Yet they do not account for the state of the electricity grid by integrating dynamic electricity price signals. In their simulation study, Killian et al. (2016) propose integrating MPC and FLC strategies for multi-zone building heating and cooling control to enhance robustness across diverse buildings and heating and cooling system types, addressing the strong dependency of MPC on accurate building model forecasts. However, this approach does not treat FLC as an independent control strategy; instead, it uses FLC as a supplement to MPC. On the other hand, Duman et al. (2021) couples the Mixed-Integer Linear Programming (MILP) EMS with a smart fuzzy-logic-based thermostat that provides efficient demand response and thermal comfort. The study demonstrates that, in the Turkish electricity market, the proposed control strategy can reduce daily air conditioning costs by 24% compared to conventional thermostat control. Although they compare different household types in the simulation study, their analysis is limited to a single FLC design and does not evaluate or contrast multiple FLC algorithms. Given the state of the art, the third research gap is outlined.

Research gap 3: There is a lack of comprehensive analyses and systematic comparisons between different fuzzy logic control designs, as well as between fuzzy logic control and other control strategies, for demand response applications in both simulation studies and real-world experiments under similar conditions.

Building energy storage management

Hybrid Energy Storage System (HESS) are essential for enhancing energy autonomy and reducing operational costs in both large-scale power energy systems, as highlighted by Yang et al. (2024), and residential building applications, as reported by Go et al. (2023). Among the various operational configurations of HESS, extensive research confirms that Battery Energy Storage System (BESS) is suitable for short-term storage, while long-term storage is most frequently implemented through hydrogen systems in energy systems with high renewable energy generation (Le et al. 2023, Giovanniello and Wu 2023).

Go et al. (2023) examine the HESS, comprising BESS and hydrogen, to enhance the self-sufficiency of residential energy supply systems. The integration of hydrogen storage within HESS not only compensates for self-discharge losses inherent to BESS but also contributes to reducing CO_2 emissions. Additionally, thermal energy generated during fuel cell operation can be recovered and utilized to meet space heating and DHW demands. Ou et al. (2021) design and validate an optimal EMS to ensure reliable and efficient operation of a HESS incorporating fuel cell, BESS, and thermal energy storage. Their findings indicate that heat recovery from fuel cell operation can enhance overall system efficiency by approximately 20%. Gandiglio et al. (2014) investigate the heat recovery potential of a residential-scale 1 kW fuel cell integrated with an underfloor heating system, demonstrating that the proposed configuration achieves fuel cell system efficiency of 75%. Furthermore, Oh et al. (2012) assess the thermo-economic feasibility of implementing a fuel cell-based energy system in a residential apartment, concluding that combined heat and power generation achieves a 20% reduction in operational costs compared to conventional systems.

Wang et al. (2024) propose a dual-layer MPC framework for off-grid residential buildings in northern China, demonstrating the feasibility of economically optimized operation of a HESS comprising both BESS and hydrogen storage. Boynuegri and Tekgun (2023) explore load-shifting potential in an off-grid residential EMS using FLC, aiming to reduce hydrogen consumption in systems powered by renewable sources (PV and wind turbines). Their findings indicate that FLC-based EMS reduces hydrogen consumption by 7.03% and improves annual fuel cell efficiency by 4.6% compared to conventional EMS strategies, which activate fuel cell immediately following renewable generation shortfalls. However, the flexibility of the BESS and the heat recovery potential of fuel cell remain unaddressed. Šanić and Barbir (2022) evaluate a stand-alone micro-trigeneration system performance, which couples cooling, heating, and power. They control the system by an RBC-based EMS in a Croatian single-family house. Their results show that 80% of thermal loads can be met by utilizing waste heat from fuel cell and heat pump operating in cooling mode during summer in a Mediterranean climate, though the flexibility of thermal building mass is not considered. Furthermore, Vivas et al. (2022) develop an FLC-based EMS for a residential building with HESS, relying on demand profiles and without exploiting thermal flexibility. Duman et al. (2021) notice that EMS and thermal control are typically investigated independently. However, their integration can yield synergistic benefits and enhance overall building operational flexibility.

One conventional solution in microgrids is to couple heat pumps with fossil-fuel-driven combined heat and power units, which provide a flexible power supply and useful heat when RES generation is insufficient. The use of hydrogen-based systems in residential buildings is generally considered suboptimal due to high capital costs and low overall efficiency. Nevertheless, there are not many alternatives for long-term energy storage that are currently available (Esposito et al. 2024). Although economic feasibility has not yet been achieved, hydrogen systems are recognized as essential components of resilient energy systems, enabling buildings to achieve energy autonomy and continue operating during grid blackouts (Mena et al. 2024). Given the significant role of buildings in the sustainability transition, integrating hydrogen systems with RES has been shown to reduce greenhouse gas emissions (Naumann et al. 2024). As already mentioned, when operating in combined heat and power mode, recovering waste heat from the hydrogen conversion improves overall system efficiency by reducing the demand for heat pump operation. Based on the state of the art discussed in this subsection, the fourth research gap is defined.

Research gap 4: There is a lack of research on building energy management systems that leverage thermal building mass flexibility, where a fuel cell and a heat pump are coupled in a configuration combining photovoltaics, battery storage, hydrogen storage, and domestic hot water storage.

1.2 Research questions and contributions

This dissertation advances the literature on the research gaps outlined in Section 1.1 by addressing the following Research Questions (RQs) sorted according to the introduced research topics:

Research questions

Reduced-order thermal building modeling

RQ1: What impact does the occupant behavior, defined as the interaction of the occupants with energy control systems and building components (windows, lighting, and related components) and the heat emitted by the occupants, have on the thermal building model forecasts? How can the accuracy of the indoor air temperature forecast be improved?

Building heating system modeling

RQ2: How does model order reduction influence the dynamic behavior of the multi-physics building heating system model validated on a real-world facility?

Building thermal control

RQ3: How can fuzzy logic control be designed to exploit building thermal flexibility for demand response programs utilizing thermal building mass in simulation and real-world applications?

Building energy storage management

RQ4: How can the coupling of a heat pump and a hydrogen fuel cell contribute to the demand response in buildings with distributed energy resources comprising photovoltaics and electrical, thermal, and hydrogen energy storage systems?

RQ5: How can a fuzzy logic controller be implemented as a forecast- and model-free energy management system for residential buildings with distributed energy resources, as listed in research question 4?

Simulation and modeling are essential for developing new control strategies, evaluating them in initial testing stages, understanding system dynamics, planning, and anticipating potential future scenarios. The models can play an essential role in drawing conclusions and making decisions based on simulations. Thus, the models need to be approached critically. The first part of this dissertation focuses on the analysis and methodology for model uncertainty and on the potential for complexity reduction.

RQ1 questions the forecast accuracy of reduced-order gray-box thermal building models in occupied buildings, where great uncertainty comes from the OB and their interaction with building components. The forecasting accuracy is analyzed, and an ensemble method is proposed to improve the accuracy. Answering **RQ1** advances the literature by filling **research gap 1**.

More complex models do not necessarily yield more accurate representations of real facilities (Robinson 2023). Building on this observation, **RQ2** addresses **research gap 2** by examining how reducing the order of the heating system model influences system dynamics. The residential heating system, consisting of a heat pump, space heating, and DHW storages, is modeled in the Modelica environment and validated on a real-world facility. The reduction potential is identified, and the impact of reducing component complexity is analyzed.

Furthermore, recent studies have highlighted the need for less-invasive control approaches in buildings to enable the wider commercial implementation of energy flexibility (de Chalendar et al. 2024, Amato et al. 2023, Clauß et al. 2024). Thus, the second subset of the RQs examines the potential of forecast- and model-free control strategies for energy flexibility in buildings. Model predictive control strategy, a popular choice, requires forecasting models of buildings and systems to achieve optimization-based behavior. De Chalendar et al. (2024) emphasize the need for new approaches that complement rather than replace industrial standards, such as RBC strategies. In that sense, Figure 1.2 illustrates the simplicity-optimality relation among popular approaches for control algorithms in buildings (Talebi and Hatami 2020, Šanić and Barbir 2022, Sievers et al. 2025, Wang et al. 2024). Since the FLC entails a trade-off between simplicity and optimality, its performance will be assessed throughout this thesis. **RQ3** bridges **research gap 3** by examining the implementation of FLC as a forecast- and model-free controller to exploit building thermal flexibility in demand response, incorporating the thermal building mass as auxiliary storage. First, the comparative analysis is undertaken in simulation. In this context, two FLCs, an economic-energy-efficient and a comfort controller, are compared with a simple hysteresis controller. Moreover, to assess real-world performance, the FLC is implemented in a practical experiment and benchmarked against a conventional control strategy, questioning the FLC's feasibility for commercial implementation.

RQ4 investigates how coupling of a heat pump and fuel cell in residential buildings with distributed energy resources, including PV and thermal, electrical, and hydrogen storage, can enhance their contribution to demand response. To efficiently utilize energy, FLC is investigated for the setup described above. **RQ5** questions the feasibility of the advanced forecast- and model-free FLC strategy for managing distributed energy resources while preserving occupants' thermal comfort.

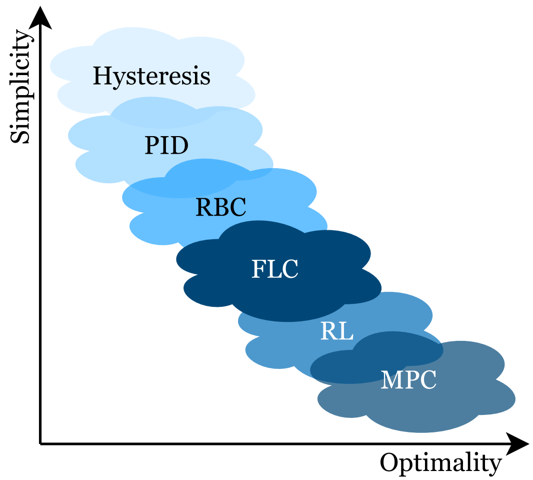

Figure 1.2: Illustration of simplicity-optimality relation among the most widely adopted building energy control strategies in the literature, including hysteresis control, Proportional–Integral–Derivative (PID), RBC, FLC, Reinforcement Learning (RL), and MPC.

The focus is on the controller's ability to manage energy flexibility across sector-coupled components, with the fuel cell and heat pump envisioned as complementary technologies. The controller is evaluated in heating mode in a residential building, while the heat recovery performance is assessed using the fuel cell system's efficiencies reported in the literature. Answering the **RQ4** and **RQ5** addresses the **research gap 4**.

This dissertation contributes to two key areas in the field of energy building flexibility. First, it investigates the influence of OB uncertainties on reduced-order thermal building models and proposes a method to improve predictive accuracy. It further critically evaluates building energy system models, analyzing the impact of model order reduction on system dynamics. Second, it advances a control strategy for exploiting sector-coupled energy flexibility while maintaining occupant thermal comfort. Two flexibility domains are addressed: thermal flexibility, enabled by thermal energy storage and thermal building mass, and electrical flexibility, achieved through short-term BESS and long-term hydrogen storage. For controller design, FLC is developed as an advanced form of RBC, preserving simplicity by minimizing data and forecasting requirements. Its performance is benchmarked against both conventional controllers and optimization-based strategies. **In summary, this dissertation investigates the uncertainty and complexity of building energy modeling and proposes and analyzes a forecast- and model-free FLC strategy for demand response in buildings.**

1.3 Thesis outline

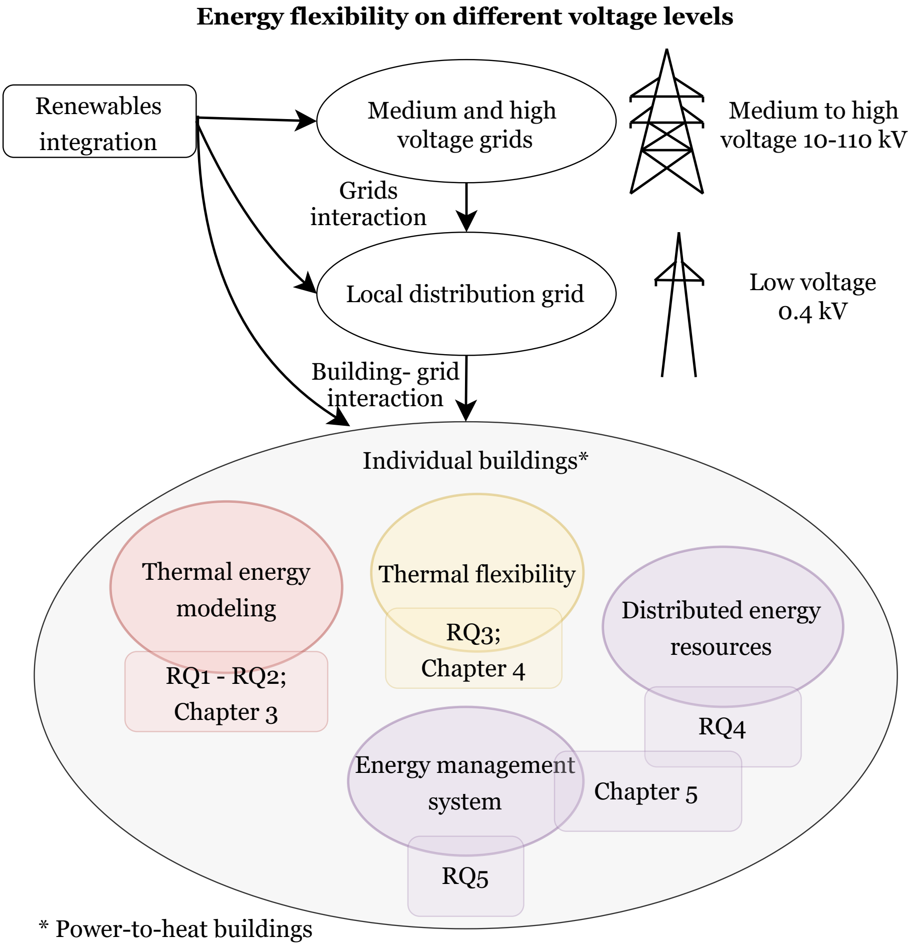

Figure 1.3: Contribution fields, classifying the addressed research questions to the corresponding chapters.

The structure of the dissertation includes the theoretical foundations relevant to the main research topics, as presented in Chapter 2. In Chapter 3, the research gaps related to building energy modeling are investigated. The first part of this chapter addresses **RQ1** by analyzing the influence of OB patterns on thermal building models and by proposing a method to improve the forecast of indoor air temperature. The second part examines **RQ2** by critically evaluating how simplifying the building heating system model affects overall model accuracy. Chapter 4 advances thermal building energy flexibility by proposing FLC algorithms for demand response in both simulation-based and real-world experiential settings. This chapter responds to **RQ3**. Chapter 5 further extends building flexibility by incorporating long- and short-term energy storage systems. Here, **RQ4** is addressed by analyzing the building setup with distributed energy resources, incorporating the heat pump and fuel cell as complementary components. Furthermore, **RQ5** is addressed by developing an EMS for the building with distributed energy resources, employing FLC as its core decision-making control strategy. Figure 1.3 illustrates the contribution field of the present dissertation with research questions addressed in the corresponding chapters. Finally, Chapter 6 concludes the dissertation and gives an outlook for future work.

2 Preliminaries

This chapter is organized into two sections. Section 2.1 presents the preliminaries of modeling, including the classification and characteristics of various energy system modeling types. Section 2.2 introduces the fundamental principles underlying the control strategies employed throughout the present dissertation.

2.1 Building Modeling

Farzaneh (2019) defines the process of modeling with the following steps: (i) identifying a problem and clarifying the objectives for creating the model, (ii) identifying what is already known, (iii) defining the physical principles and equations necessary for obtaining the required results, and (iv) creating the model. In the building sector, two major building modeling directions exist: (i) building information modeling and (ii) building energy modeling. Building information modeling provides a building model that is “ data-rich, object-oriented, intelligent and parametric digital representation of the facility, which can provide data appropriate to various users’ needs” (Gao et al. 2019). In addition to representing the physical facility, the building information model incorporates an operational knowledge base, enabling multidisciplinary expert collaboration and data-driven decision-making processes (Hammes et al. 2026). On the other hand, building energy modeling is used to analyze energy efficiency and building performance, evaluate architectural and mechanical design, and test alternative design possibilities (Gao et al. 2019). It offers an opportunity to save time and resources, providing representation, analysis, predictions, and a deeper understanding of real-world building systems. Throughout this dissertation, the field of building energy modeling is examined.

Building energy modeling can be categorized into three distinct classifications: white-, black-, and gray-box models (Balali et al. 2023). White-box modeling is a physics-based modeling approach that necessitates a comprehensive understanding of the underlying physical system. For example, in the case of the building envelope, this type of model includes building properties such as the building’s geometry, heat conduction, and material types (Balali et al. 2023). White-box models have proven helpful in improving the understanding of the interrelationships among different energy components. Nevertheless, the development and calibration of these models are challenging (Arendt et al. 2018), as their validation is time-consuming. Due to the complexity of these models, characterized by numerous equations and nonlinear characteristics, their implementation in model-based control strategies and optimization poses significant challenges (Drgoňa et al. 2020). However, they are most frequently utilized for large-scale energy planning (e.g., district heating) to investigate economic effects and sustainable power supply (Pieper et al. 2020).

Conversely, the black-box modeling approach is entirely data-driven, with behavior prediction derived from prior system states and the current input information. The physical structure is not taken into consideration, whereas the forecasting process is highly dependent on the training data (Li et al. 2021b). Nevertheless, the implementation of black-box models demands less time than that of white-box models when it comes to the development and calibration of models. On the other hand, black-box models require retraining when additional outputs are needed for analysis (Pachano et al. 2025).

The third method is gray-box modeling, which was envisioned to incorporate the strengths of white- and black-box approaches (Afroz et al. 2018). The presence of a physical structure enables the identification of parameters through the implementation of either a forward or an inverse approach. The forward approach utilizes physical models for parameter identification, whereas the inverse approach employs data-driven methods, such as curve fitting (Li et al. 2021b). Gray-box models achieve high accuracy while offering additional benefits such as simplicity and reduced computational cost, while preserving the fundamental physics of the system. However, the development of data-driven gray-box models demands expertise in both the physical structure of the energy system and parameter identification methods. Their prediction, however, depends heavily on the accuracy and quality of the underlying measurement data, as well as the accuracy of parameter estimation (Balali et al. 2023). Gray-box building models are primarily employed for two purposes: (i) thermal load calculation and (ii) heat dynamics analysis (Li et al. 2021b). These categories form the basis for advanced applications such as urban and district energy modeling, building-grid integration, and building control and optimization. The reduction potential between these different types of models is described in detail in Chapter 3.

2.1.1 Gray-box reduced-order modeling

Gray-box models rely on partial physical knowledge, which is often incomplete and uncertain. This dissertation focuses on the inverse gray-box modeling approach, emphasizing model identification based on measurement data. According to Sohlberg (2012), the inverse modeling procedure consists of: (i) basic modeling by defining a structure based on existing system knowledge, (ii) expanded modeling by introducing uncertain or unknown components, (iii) experimentation via collecting informative measurement data with sufficient input-output variation, (iv) identification with estimating of unknown parameters from measurements, (v) model analysis by evaluating performance indicators, loss functions, and parameter validation, and (vi) model appraisal by assessing the model and identifying opportunities for further refinement. One of the areas where gray-box modeling has found purpose is building envelope modeling, as evidenced by a large number of scientific papers in the field (Klanatsky et al. 2023, Harb et al. 2016, Drgoňa et al. 2020, Bird et al. 2022).

Gray-box models can have different structures and varying levels of complexity. For gray-box building envelope models, the RC analogy is typically employed. They are usually formatted as $x\mathrm{R}y\mathrm{C}$, where x and y denote the numbers of R- and C-elements, respectively. The universal RC model needs to satisfy the first law of thermodynamics and is presented as follows (Frahm et al. 2022a):

$$\underbrace{C_i \frac{\mathrm{d}T_i(t)}{\mathrm{d}t}}_{\substack{\text{derivative of internal} \\ \text{energy for node } i}} = \underbrace{\sum_j \dot{Q}_j(t)}_{\text{heat gains}} + \underbrace{\sum_z \frac{\Delta T_{i,z}(t)}{R_{i,z}}}_{\substack{\text{heat transfer between} \\ \text{node } i \text{ and adjacent node } z}} \tag{2.1}$$

where the T_i represents the temperature of the observed node i in $^\circ\mathrm{C}$. The thermal capacitance of the node i is denoted as C_i (measured in $\mathrm{J/K}$) and quantifies the material's ability to store heat. The external heat gains impacting the node i are presented with $\sum_j \dot{Q}_j(t)$ (measured in W). The term $\Delta T_{i,z}$ in $^\circ\mathrm{C}$ defines the temperature difference between node i and adjacent node z, while the opposition to heat flow between nodes i and z at different temperatures is known as thermal resistance $R_{i,z}$ (measured in $\mathrm{K/W}$).

The system's complexity depends on the set of differential equations, which is determined by the number of system states. The set of ordinary differential equations is formulated into the state-space system as follows:

$$\dot{x}(t) = Ax(t) + Bu(t) \tag{2.2}$$

$$y(t) = Cx(t) + Du(t) \tag{2.3}$$

where the state vector x contains the building temperatures, such as indoor air temperature, inner and outer wall temperature, building mass, and related temperatures. The input vector u comprises disturbances, such as relevant weather information and cooling- or heating-control signals. The output y denotes the relevant state variable, such as indoor air temperature. The state, input, output, and feed-forward matrices are represented as A, B, C, and D, respectively.

2.1.2 Energy modeling environments

A wide range of commercial and open-source tools support white-box modeling. The Modelica language (Fritzson 2015) enables object-oriented modeling of energy systems, with open-source libraries such as AixLib (Maier et al. 2024), Buildings (Wetter et al. 2014), BuildingSystems (Nytsch-Geusen et al. 2013), and IDEAS (Jorissen et al. 2018) providing extensive model collections. Modelica's modular structure allows components to be easily replaced, providing great flexibility and choice of components with different structural complexity. Dymola [1] (commercial) and OpenModelica [2] (open-source) are key Modelica-based environments. TRNSYS [3] is another widely used commercial tool offering capabilities for thermal, electrical, hydrogen, and traffic flow modeling. EnergyPlus [4] focuses on building components and simulates HVAC systems, loads, water demand, and related processes. For gray- and black-box modeling, Matlab and Python are commonly used. Matlab's System Identification Toolbox[5] and Python libraries such as SciPy and Scikit-learn enable curve-fitting approaches for system identification.

Comprehensive energy systems typically comprise diverse subsystems, including sector coupling (i.e., thermal, electrical, gas, and related), occupant behavior, and various load and generation components. This full range of applications cannot be addressed by a single software tool with the same level of detail, as most are designed for specific domains. To enable integrated analysis, co-simulation offers a viable solution by coupling different software environments (Palensky et al. 2017). This approach has the potential to support distributed simulation while preserving data and model confidentiality (Kocher et al. 2024).

2.2 Building energy management systems

In the year 1997, the IEA defined the building EMS as "an electrical control and monitoring system that has the ability to communicate data between control nodes (monitoring points) and an operator terminal. The system can have attributes from all facets of building control and management functions such as HVAC, lighting, fire, security, maintenance management and energy management" (IEA 1997). According to IEA, the objectives of building EMS are as follows: (i) provision of a healthy and comfortable indoor environment, (ii) ensuring the user and owner safety, and (iii) ensuring the economic operation with respect to occupant needs while

[1] https://www.3ds.com/de/products/catia/dymola
[2] https://openmodelica.org/
[3] https://www.trnsys.com/
[4] https://energyplus.net/
[5] https://de.mathworks.com/products/sysid.html

minimizing the energy consumption. Furthermore, the buildings managed by EMS are called "Smart building" (Luo et al. 2024). The building EMS functions as the central control unit of a building, reducing energy waste, minimizing occupant involvement in decision-making, and enabling bidirectional communication with the grid by managing building loads to meet occupant needs or support grid operations (Luo et al. 2024). Sections 2.2.1, 2.2.2, and 2.2.3 present the fundamental concept of feedback control theory and the control algorithms used throughout this thesis.

2.2.1 Feedback control

Figure 2.1 illustrates the structure of a feedback control system. The controlled system executes tasks in response to input signals, while the control loop integrates the controller, actuator, system, and sensors to achieve the desired system output (Sundararajan 2022).

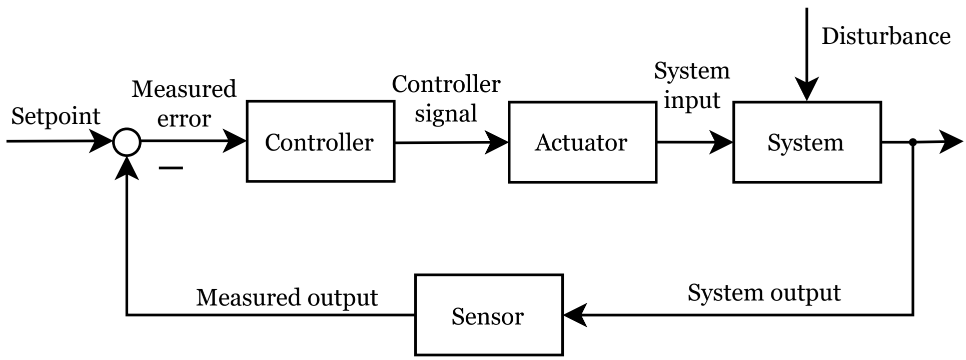

Figure 2.1: General structural diagram of the feedback control.

Three conventional types of feedback controllers are Proportional–Integral–Derivative (PID) controller, hysteresis, and RBC. In a PID controller, the proportional compensator is directly proportional to the current error signal; it increases the speed of the response, but it can not by itself eliminate the steady-state error. The integral compensator is proportional to the integral of the error; it can eliminate the steady-state error, but can also increase the overshoot and settling time. The derivative is proportional to the error derivative, which can reduce overshoot and settling time but amplify measurement noise. Tuning the PID controller parameters to achieve the desired behavior depends on the physical system's characteristics. On the other hand, a hysteresis controller is a two-point controller that switches the control input between two states. When the controlled state reaches its upper limit, the controller deactivates and reactivates when it reaches its lower limit. The RBC is designed by a set of IF-THEN rules. The advantage of this control type is its minimal information requirement and its ability to ensure reliable control. However, it cannot guarantee optimization-based behavior. One advanced form of RBC is Fuzzy Logic Control (FLC).

2.2.2 Fuzzy logic control

Fuzzy logic, founded by Lotfi A. Zadeh (Zadeh 1965, 1973), is a method of reasoning that is analogous to human reasoning. FLC can be regarded as an advanced form of RBC, as it relies on a rule dataset consisting of an antecedent IF part and a consequent THEN part. FLC extends the traditional RBC by allowing partial truth (Altas 2017). Three most popular fuzzy reasoning algorithms are: Mamdani (Mamdani 1977), Takagi–Sugeno (Takagi and Sugeno 1985), and Tsukamoto (Tsukamoto 1979). The difference between these approaches lies only in the consequent part. Mamdani FLC comprises three main layers: (i) fuzzification, which converts crisp input values into corresponding fuzzy values; (ii) an inference engine that consists of a rule base; and (iii) defuzzification, which transforms the conclusion from fuzzy set into a crisp value (Altas 2017). The Takagi–Sugeno inference system differs from the Mamdani approach in the output representation. Instead of producing a fuzzy set, the Takagi–Sugeno inference system generates a crisp output expressed as a crisp function $f(x, y)$, which is directly dependent on the corresponding input variables x and y. Tsukamoto method, on the other hand, uses fuzzy sets in the consequent part, similar to the Mamdani approach. However, each activated fuzzy rule produces a crisp value, and the weighted average presents the output of the FLC. Throughout the remainder of the dissertation, the Mamdani fuzzy logic is utilized and referred to as FLC.

Figure 2.2 illustrates the universe of discourse of indoor air temperature T. The membership functions “cold” and “warm” serve as a bridge between crisp values and the fuzzy world. Suppose that the indoor air temperature is $T = 20\,^{\circ}\mathrm{C}$. The concept of fuzziness makes it possible to describe a temperature as being 20% “warm” and 80% “cold”. This flexibility is not achievable with the traditional RBC approach, where the temperature must be classified as either “warm” or “cold” in this case. This highlights a major drawback of classical RBC, where even a small temperature change can completely switch the active rule. For instance, if we define indoor air as “cold” up to $21\,^{\circ}\mathrm{C}$ and “warm” at $21\,^{\circ}\mathrm{C}$ and above, the control signal depends entirely on this state. A minor increase from $20.9\,^{\circ}\mathrm{C}$ to $21.1\,^{\circ}\mathrm{C}$ would trigger a full change in the control signal, even though the actual temperature difference is negligible.

Fuzzy sets represent the degree of membership of the elements in a corresponding set:

$$A = \{(x, \mu_{\mathrm{A}}(x)) \mid x \in X\} \tag{2.4}$$

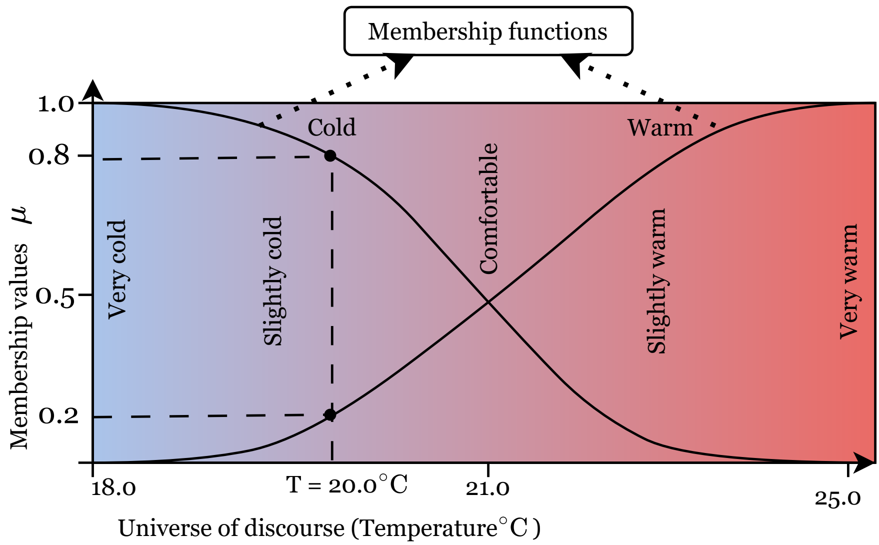

Figure 2.2: Fuzzy sigmoid membership functions. Figure is inspired by Altas (2017).

where x is an element of the universe X, $\mu_{\mathrm{A}}(x)$ is membership value of element x in a fuzzy set A (Altas 2017). The higher the membership value $\mu_{\mathrm{A}}(x)$ of an element x is, the more it belongs to the respective set. Common membership function shapes include triangular, trapezoidal, sigmoid, and Gaussian (Altas 2017). Fuzzy sets are defined for all input and output variables. In order to manipulate fuzzy sets, the operators are defined, where the following relations can be utilized: (i) intersection $\cap$, (ii) union $\cup$, and (iii) negation $\neg$. Table 2.1 presents two types of fuzzy operators: one, originally defined by Zadeh, and the other, probabilistic (Dernoncourt 2013).

Table 2.1: Fuzzy MIN/MAX and probabilistic operators for two fuzzy sets A and B. Table is derived from Dernoncourt (2013).

Method	Intersection (AND)	Union (MAX)	Negation (NOT)
Min-Max	$\min(\mu_{\mathrm{A}}(x), \mu_{\mathrm{B}}(x))$	$\max(\mu_{\mathrm{A}}(x), \mu_{\mathrm{B}}(x))$	$1 - \mu_{\mathrm{A}}(x)$
Probabilistic	$\mu_{\mathrm{A}}(x) \times \mu_{\mathrm{B}}(x)$	$\mu_{\mathrm{A}}(x) + \mu_{\mathrm{B}}(x) - \mu_{\mathrm{A}}(x) \times \mu_{\mathrm{B}}(x)$	$1 - \mu_{\mathrm{A}}(x)$

The following is an example of how the rules are designed:

$$\underbrace{\text{IF the indoor air temperature is “cold” AND the solar radiation is “low”}}_{\text{antecedent}}$$
$$\underbrace{\text{THEN set the heating to “high”.}}_{\text{consequent}}$$

where “cold”, “low”, and “high” represent the fuzzy sets in the following universes: “indoor air temperature”, “solar radiation”, and “heating”, respectively. Operator “AND” in antecedent part defines how the two conditions (*indoor air temperature is cold* and *solar radiation is low*) are combined (see Table 2.1). The total number of possible rules depends on the number of input variables n_x and the number of membership functions m:

$$\text{Total number of possible rules} = \prod_{i=1}^{n_x} m_i \tag{2.5}$$

Then, the conclusion is derived. It has also different forms, with the most common (Dernoncourt 2013):

(i) Mamdani implication – $\mu'_{\mathrm{B}}(y) = \min(\mu_{\mathrm{A}}(x_0), \mu_{\mathrm{B}}(y))$,

(ii) Larsen Implication – $\mu'_{\mathrm{B}}(y) = \mu_{\mathrm{A}}(x_0) \cdot \mu_{\mathrm{B}}(y)$,

where x_0 is corresponding input value, A is universe of the input variable x and B is universe of the output variable y. The $\mu'_{\mathrm{B}}(y)$ is fuzzy conclusion. If there are multiple inputs and outputs, more than one rule will usually be activated, and the fuzzy output can be derived by combining the activated consequent sets, typically via aggregation. To translate the fuzzy conclusion, which is represented as an area, into a single crisp value, a defuzzification method must be selected. Some of the standard methods for defuzzification are as follows: (i) lower maximum - smallest value where membership is maximum, (ii) upper maximum - largest value where membership is maximum, (iii) mean of maxima - average of all points where membership is maximum, (iv) equal areas - the conclusion area is divided into two equal areas, and (v) center of gravity - abscissa of the area of aggregated activated consequent fuzzy sets. A detailed example explaining the FLC operation is provided in Appendix A.

2.2.3 Model predictive control

MPC is an advanced control methodology that determines control actions by solving an optimization problem over a finite prediction horizon. Crucially, MPC utilizes a system model and forecasts of external time-varying parameters, such as weather conditions and system constraints, to predict future system states (Drgoňa et al. 2020). By using these predictions, MPC can respond to anticipated disturbances rather than waiting until they have already affected the system, like conventional controllers.

The "optimal" control action is the one that achieves the smallest possible objective value among all feasible solutions, provided the constraints are satisfied. The general MPC formulation can be described as follows (Drgoňa et al. 2020):

$$\min_{u_0,\ldots,u_H} \sum_{k}^{H} \ell_k \left(x_k, u_k, d_k\right) \tag{2.6}$$

$$\text{s.t.: } x_{k+1} = f(x_k, u_k, d_k), \quad k \in \mathbb{N}^H \tag{2.7}$$

$$y_k = g(x_k, u_k, d_k), \quad k \in \mathbb{N}^H \tag{2.8}$$

$$\text{for: } x_k \in \mathcal{X}, \quad u_k \in \mathcal{U}, \quad k \in \mathbb{N}^H \tag{2.9}$$

$$d_k = d(t + kt_{\mathrm{s}}), \quad k \in \mathbb{N}^H \tag{2.10}$$

$$x_0 = \hat{x}(t) \tag{2.11}$$

where the system states is represented with x_{k}, input signals with u_{k} and disturbances with d_{k} for the time step k and sample time t_{s}. The cost function ℓ_{k} is minimized under the input and state constraint sets $\mathcal{U}$ and $\mathcal{X}$, respectively. The forecast of disturbances is defined by Equation (2.10), while the initial states are represented by Equation (2.11). MPC solves the optimization problem for the finite horizon H in an open loop. To address uncertainty, a receding-horizon strategy is introduced. At each control step, MPC computes an optimal sequence of control actions over a prediction horizon H. However, rather than applying the entire sequence, only the first control input is used. Subsequently, the system state is updated using the new measurements, and the optimization is repeated for the next horizon. This process creates a feedback loop, ensuring that the controller continuously adapts to disturbances and modeling errors.

2.3 Statistical indicators

This section introduces the standard statistical indicators used throughout this thesis for quantitative evaluation. The first part focuses on the error metrics used to evaluate the proposed model's performance, providing insight into its predictive accuracy. The second part outlines the statistical indicators used to quantitatively evaluate the controller's characteristics and effectiveness, thereby ensuring a comprehensive understanding of its operational features.

2.3.1 Error measures

Mean Absolute Error (MAE) defines the absolute average error between two sets of values, (Karunasingha 2022):

$$\text{MAE} = \frac{1}{n}\sum_{k=1}^{n} |\hat{x}_k - x_k| \tag{2.12}$$

where x_k represents the measured value and $\hat{x}_k$ the proposed solution value at the timestep k. The total number of values is presented with n. Root Mean Square Error (RMSE) penalizes large outliers as the errors are squared before averaging, and it can be presented as follows (Karunasingha 2022):

$$\text{RMSE} = \sqrt{\left(\frac{1}{n}\sum_{k=1}^{n}(\hat{x}_k - x_k)^2\right)} \tag{2.13}$$

Mean Absolute Percentage Error (MAPE) is another popular metric for evaluating the prediction accuracy, and it is defined as follows (Khair et al. 2017):

$$\text{MAPE} = \frac{1}{n}\sum_{k=1}^{n}\left|\frac{\hat{x}_k - x_k}{x_k}\right| \cdot 100\% \tag{2.14}$$

This error is more intuitive to interpret because it is defined as a percentage. However, when the measured value x_k is close to zero, the error becomes impractical because x_k appears in the denominator, causing the MAPE to produce an excessively large value. Mainly, the above-mentioned error measures are used in Chapters 3 and 4 to evaluate the building energy models.

2.3.2 Control quality indicators

The performance indicators considered throughout the dissertation include thermal discomfort, electricity (or heating), and reimbursement costs. These indicators are inherently interdependent, exhibiting a trade-off relationship whereby the improvement of one metric often results in the deterioration of another. The main objective is to achieve a simultaneous reduction in thermal discomfort and operational costs. The thermal discomfort d, as defined in Equation (2.15), is quantified by multiplying the magnitude of the temperature constraint violation, $T_{\mathrm{air,min}}$ or $T_{\mathrm{air,max}}$, by the duration of the violation, i.e., sample time t_{s} (Mork et al. 2022):

$$d = t_{\mathrm{s}} \cdot \sum_k d_k \tag{2.15}$$

$$d_k = \begin{cases} T_{\mathrm{air,min},k} - T_{\mathrm{air},k}, & \text{if} \quad T_{\mathrm{air},k} < T_{\mathrm{air,min},k}, \\ T_{\mathrm{air},k} - T_{\mathrm{air,max},k}, & \text{if} \quad T_{\mathrm{air},k} > T_{\mathrm{air,max},k}, \\ 0, & \text{otherwise.} \end{cases} \tag{2.16}$$

The energy costs σ_{buy} and reimbursement costs σ_{sell} are defined as the sum of the multiplications of the purchased P_{buy} or sold P_{sell} power, the current price p_{buy} or reimbursement price p_{sell} signal and sample time t_{s}, respectively:

$$\sigma_i = t_{\mathrm{s}} \cdot \sum_k p_{i,k} \cdot P_{i,k}, \ \text{for } i \in \{\text{“buy”, “sell”}\} \tag{2.17}$$

These indicators are mainly used in Chapters 4 and 5 for evaluating control strategies.

2.3.3 Empirical cumulative distribution function

The Empirical Cumulative Distribution Function (ECDF) $\hat{F}(x)$ is calculated as follows:

$$\hat{F}(x) = \frac{1}{n} \sum_{i=1}^{n} 1_{X_i \leq x} \tag{2.18}$$

where $\hat{F}(x)$ is the proportion of the sample points that are less than or equal to x for the sample of data $X_1 ... X_n$ and $1_{X_i \leq x}$ is the indicator of the event. It is the empirical distribution function, which increases by $1/n$ for each sampling point.

ECDF of day-ahead price signal is used in Chapters 4 and 5 as an input information for FLC. This function provides relevant contextual information by characterizing the relative position of the current price signal within the distribution of day-ahead prices. Consequently, the controller is informed about whether the present price level is comparatively high or low with respect to prices over the day-ahead horizon. The example of the ECDF for the day-ahead price signal is illustrated in Figure 2.3. The quantity $\hat{F}(p_{\text{buy}})_k$ denotes the proportion of day-ahead price observations that are less than or equal to the price value $p_{\text{buy},k}$ at time step k.

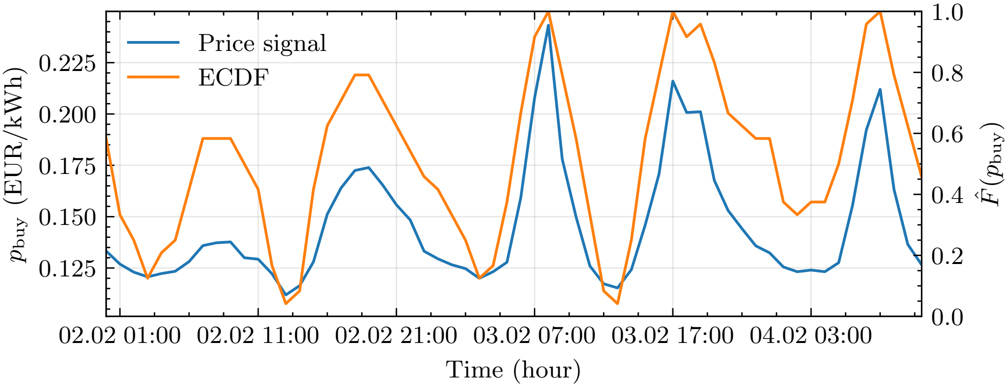

Figure 2.3: Empirical cumulative distribution function of the day-ahead electricity prices.

For example, considering the second electricity price peak depicted in Figure 2.3, occurring on February 2 between 11:00 and 21:00, the corresponding ECDF signal indicates that, although the price has a local maximum during this interval, it does not represent the highest value when evaluated relative to the distribution of the subsequent day-ahead price signals.

3 Building energy modeling

Publications supporting the chapter content

- Jovana Kovačević, et al. Improving Reduced-Order Building Modeling: Integration of Occupant Patterns for Reducing Energy Consumption. In Proceedings of the 15th ACM International Conference on Future and Sustainable Energy Systems, pages 569–579, 2024a. doi: 10.1145/3632775.3662163.
- Jovana Kovačević, et al. The Impact of Model Complexity Reduction on System Dynamics: A Modelica Case Study of a Residential Heating System. In 2025 IEEE Conference on Technologies for Sustainability (SusTech), pages 1–8. IEEE, 2025a. doi: 10.1109/SusTech63138.2025.11025706.

Numerous research studies are trying to reduce the building energy consumption (Yari et al. 2024, Bevilacqua 2021, Yang et al. 2021) by enhancing the architectural design, HVAC operation, and design, building performance ratings, and retrofit analysis (Li et al. 2021b). Moreover, advanced energy management strategies are being developed to support the grid by enabling demand-side flexibility. Modeling the building's energy systems provides the basis for developing and enhancing new control algorithms and energy system configurations.

Figure 3.1 illustrates the typical building energy modeling approaches and potential avenues for model reduction. One potential approach involves implementing physicality reduction, here defined as the horizontal reduction, which entails transforming physical white-box models into gray-box models with reduced physical details or black-box models with no physical structure. This approach can benefit from training gray- or black-box models on a significantly larger amount of data obtained from white-box models, rather than using real-world data. It is evident that white-box models have the capacity to be simulated in a variety of scenarios with a wide range of input data. Consequently, the identification of gray-box or training of black-box models would be rendered more extensive. This is beneficial, however, only if the white-box models are validated under real-world conditions. Furthermore, intragroup complexity is observed across all modeling types. It is possible to perform a reduction in a vertical manner, which applies to its own modeling type.

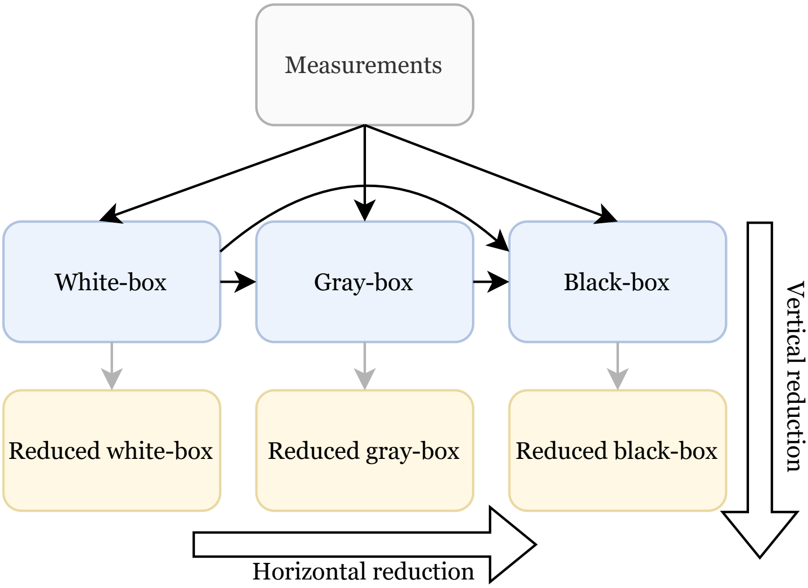

Figure 3.1: Horizontal and vertical model reduction potential. Section 3.1 utilizes a gray-box modeling approach identified on measurements, while the Section 3.2 investigates the white-box vertical reduction.

This chapter contributes to both gray-box and white-box modeling approaches for building energy systems. First, in Section 3.1, the computationally inexpensive gray-box modeling approach for thermal building models is assessed. In this context, the accuracy of the model's forecasts for the occupied building is analyzed, and a method for improvement is proposed. Specifically, by separating the identification period of gray-box models based on typical occupant patterns, the prediction accuracy can be improved. With the proposed methodology and analysis, the research question **RQ1** and **research gap 1** are addressed, which concern the challenge of thermal building forecasting under the uncertainty of OB patterns.

White-box energy system models have great potential for model reduction in Modelica and its open source libraries, such as Buildings (Wetter et al. 2014) and AixLib (Maier et al. 2024), since the components are designed to be modular and easily replaceable. These open-source libraries typically provide a wide range of components, varying in complexity.

It is important to keep white-box models as simple as possible to reduce computational complexity while remaining accurate enough to maintain interpretability. Thus, the Section 3.2 analyzes the link between the white-box building heating system model reduction and the accuracy of the model prediction. The reference model is designed in Modelica utilizing the AixLib library based on the real-world facility (Meyer 2013). It is modeled with the highest level of detail. Then, the potential for component reduction is sought, and the reduction is evaluated through seven steps by neglecting and replacing components. This section addresses research question **RQ2** and **research gap 2** by analyzing the reduction of building heating system models and their impact on dynamic behavior, and by comparing these models with the real-world facility.

3.1 Method: Integrating occupant patterns into reduced-order building models to improve forecasting accuracy

This dissertation introduces a new method that improves gray-box modeling by identifying distinct models for working days and weekends, thereby splitting the impact of occupant behavior patterns on models. This method is validated using five weeks of measured data from a real office building at the Living Lab Energy Campus (LLEC) at the Karlsruhe Institute of Technology (KIT) Wiegel et al. (2022). The proposed ensemble structure is benchmarked against the classically identified thermal building model approaches (Harb et al. 2016, Frahm et al. 2022a), demonstrating improved robustness in indoor air temperature prediction across varying occupancy conditions.

3.1.1 Methodology

In this section, the structural formulation of the RC thermal building model is presented, including its underlying equations. Subsequently, the methodology employed for parameter identification is discussed in detail, outlining the ensemble model structure.

Model structure

To address the sensitivity of thermal building models to occupant-related heat gains, the following model structure is proposed:

$$\begin{aligned} C_{\mathrm{air},j}\frac{\mathrm{d}T_{\mathrm{air},j}}{\mathrm{d}t} = \frac{2\cdot(T_{\mathrm{w},j}-T_{\mathrm{air},j})}{R_{\mathrm{w},j}} + \frac{(T_{\mathrm{amb}}-T_{\mathrm{air},j})}{R_{\mathrm{inf},j}} + \\ \frac{T_{\mathrm{m},j}-T_{\mathrm{air},j}}{R_{\mathrm{m},j}} + \dot{Q}_{\mathrm{conv},j} + g_{\mathrm{sol},j}\dot{q}_{\mathrm{sol}} + \dot{Q}_{\mathrm{ig},j} \end{aligned} \tag{3.1}$$

$$C_{\mathrm{m},j}\frac{\mathrm{d}T_{\mathrm{m},j}}{\mathrm{d}t} = \frac{(T_{\mathrm{air},j} - T_{\mathrm{m},j})}{R_{\mathrm{m},j}} + \dot{Q}_{\mathrm{rad},j} \tag{3.2}$$

$$C_{\mathrm{w},j}\frac{\mathrm{d}T_{\mathrm{w},j}}{\mathrm{d}t} = \frac{2\cdot(T_{\mathrm{air},j} - T_{\mathrm{w},j})}{R_{\mathrm{w},j}} + \frac{2\cdot(T_{\mathrm{amb}} - T_{\mathrm{w},j})}{R_{\mathrm{w},j}} \tag{3.3}$$

$$\frac{\mathrm{d}\dot{Q}_{\mathrm{ig},j}}{\mathrm{d}t} = 0 \tag{3.4}$$

where the index $j \in \mathcal{J}$ and set $\mathcal{J} = \{\mathrm{R}_1,\ \mathrm{R}_2,\ \mathrm{R}_3\ ,\mathrm{R}_4\ ,\mathrm{R}_5,\ \mathrm{K},\ \mathrm{B}\}$ refers to the individual rooms. The kitchen is denoted by K and the bathroom by B. Variables $T_{\mathrm{w},j}$, $T_{\mathrm{air},j}$ and $T_{\mathrm{m},j}$ represent the wall, indoor air, and thermal building mass temperatures, respectively. The occupant-related heat load that impacts indoor air temperature is denoted $\dot{Q}_{\mathrm{ig},j}$ and is calculated in W.

The thermal capacitance of the indoor air, wall and thermal building mass are denoted as $C_{\mathrm{air},j}$, $C_{\mathrm{w},j}$ and $C_{\mathrm{m},j}$, respectively. In this context, the thermal building mass comprises building elements characterized by slow thermal dynamics, such as roofs, floors, and internal concrete cores. The parameters $R_{\mathrm{m},j}$, $R_{\mathrm{w},j}$, and $R_{\mathrm{inf},j}$ are the thermal resistances against heat transfer (i) between the thermal building mass and indoor air, (ii) between ambient and indoor air, and (iii) infiltration resistance, respectively. The input vector is defined as: $\mathbf{u}_j = [T_{\mathrm{amb}} \quad \dot{Q}_{\mathrm{h},j} \quad \dot{q}_{\mathrm{sol}}]^T$. The elements of the input vector are ambient temperature T_{amb}, the heat flow from the heat pump $\dot{Q}_{\mathrm{h},j}$ and the solar radiation $\dot{q}_{\mathrm{sol}}$ in $\mathrm{W/m^2}$. The solar heat gain factor $g_{\mathrm{sol},j}$, in Equation (3.1), is measured in m^2. The heat flow $\dot{Q}_{\mathrm{h}}$ is supplied by a ground source heat pump, with measurements at the building level. The heat flow allocated to each room $\dot{Q}_{\mathrm{h},j}$ is estimated proportionally using the volume ratio of the j room volume V_j to the sum of all room volumes $\sum_j V_{\mathrm{j}}$:

$$\dot{Q}_{\mathrm{h},j} = \text{Volume ratio} \cdot \dot{Q}_{\mathrm{h}} \tag{3.5}$$

$$\text{Volume ratio} = \frac{V_j}{\sum_j V_j} \tag{3.6}$$

Furthermore, the heat flow is assumed to consist of 80% convective heat $\dot{Q}_{\mathrm{conv},j}$ and 20% radiant heat $\dot{Q}_{\mathrm{rad},j}$ (Jiang et al. 1992).

The RC network representation of the thermal building model is illustrated in Figure 3.2. The original model comprises only three thermal states: the wall temperature $T_{\mathrm{w},j}$, indoor air temperature $T_{\mathrm{air},j}$, and the temperature of the building mass $T_{\mathrm{m},j}$ (De Coninck et al. 2016). To account for occupant-related heat gains, a fourth state is introduced, following the approach of Coffman and Barooah (2018), where the temporal variation of this state is assumed to be constant. This assumption is based on the premise that occupants exhibit similar patterns throughout the day, to some extent. As a result, the internal heat gain due to occupants $\dot{Q}_{\mathrm{ig},j}$ is no longer treated as an unmeasured input but is instead modeled as an additional state variable. To extend the model to

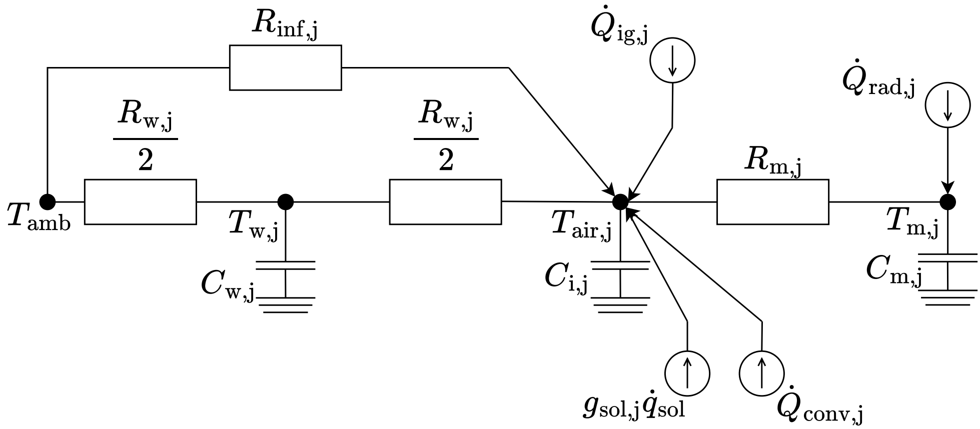

Figure 3.2: Proposed 4R3C gray-box thermal building model for room j - predefined model structure. The figure is adapted from Kovačević et al. (2024a).

a multi-zone configuration, a decentralized approach is adapted from Frahm et al. (2022b). This approach models each room independently, without thermal coupling between rooms or across floors.

Parameter identification approach

To improve the robustness of thermal building models to changes in OB patterns, the identification process is separated into two distinct periods: working days (5 days) and weekends (2 days). This distinction is motivated by the differing OB patterns in LLEC buildings across these periods (Frahm et al. 2022b). By isolating the identification to each period, the working-day model captures weekday-specific occupancy dynamics. In contrast, the weekend model reflects reduced occupancy and its lower impact on indoor air temperature. To ensure continuity between models, a transition is implemented via linear interpolation between the final two hours of the working-day model and the initial two hours of the weekend model, and vice versa. This switching between models provides the basis for the proposed *ensemble model*, which contrasts with the classical RC model identified over a full week. While the classical model assumes uniform OB, the ensemble model explicitly accounts for temporal OB variations by combining separately identified models. The ensemble modeling approach can be extended to incorporate additional temporal patterns, such as seasonal variations, by integrating more than two independently identified RC building models.

The methodology is illustrated in Figure 3.3, where subscripts “wd” and “we” denote parameters identified for working days and weekends, respectively, using the predefined model structure

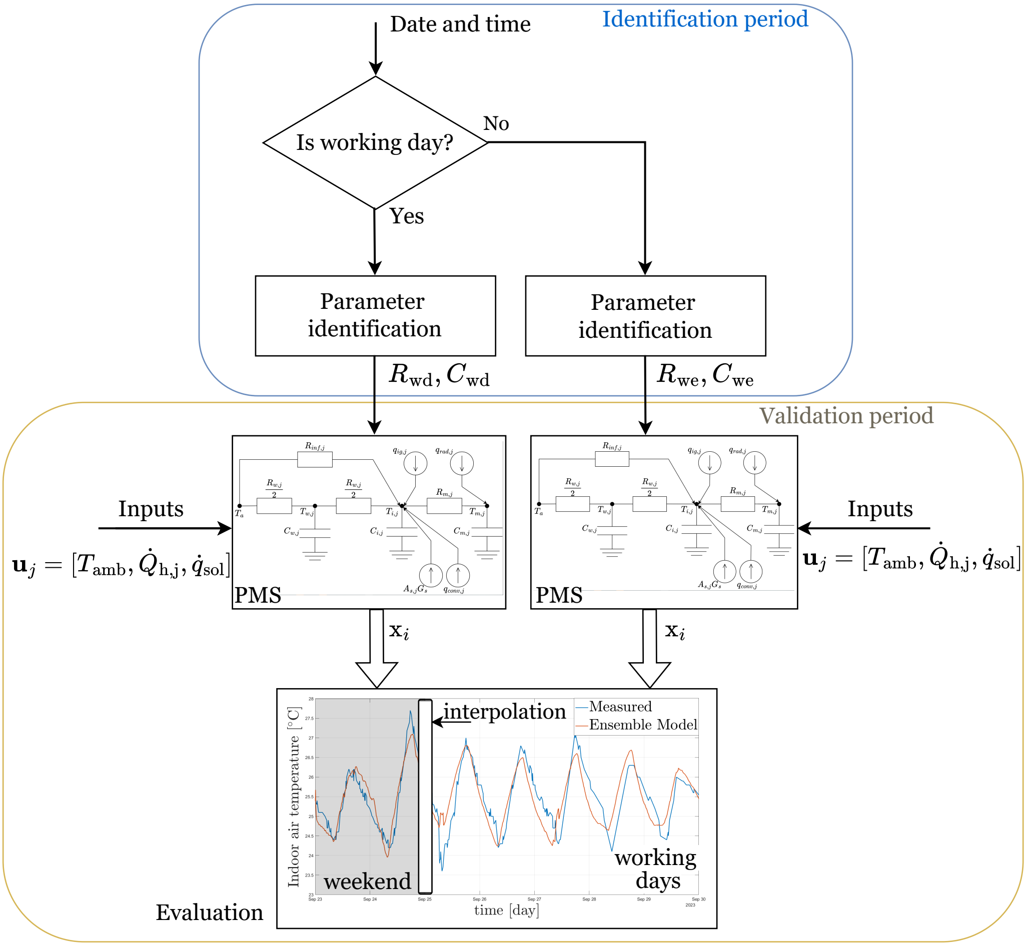

Figure 3.3: Identification and validation process of the ensemble model. The figure is adapted from Kovačević et al. (2024a).

shown in Figure 3.2. To facilitate a fair comparison, both the classical and ensemble models share the same RC structure.

3.1.2 Case study

The study focuses on five rooms, a kitchen, and a bathroom, excluding hallways and service rooms due to a lack of heating, as illustrated in Figure 3.4. Since heat flow is measured at the building level, room-level heating is estimated using volume-based allocation, as given in Equations (3.5)-(3.6). In addition to heat flow $\dot{Q}_\mathrm{h}$, ambient temperature T_amb, solar radiation $\dot{q}_\mathrm{sol}$, and indoor air temperature T_air of each room are measured. The dataset spans from September 23, 2023, to November 4, 2023. Identification is performed over two periods: September 25-30, 2023, for the working-day model and September 23-25, 2023, for the weekend model. The remaining data are used for long-range validation to assess model applicability beyond a single week. Due to limited winter data, the study focuses on fall conditions. Model identification and validation are conducted using MATLAB's System Identification Toolbox (The MathWorks Inc.). To demonstrate the model's applicability, a decentralized multi-zone structure is used, treating each room as an independent zone.

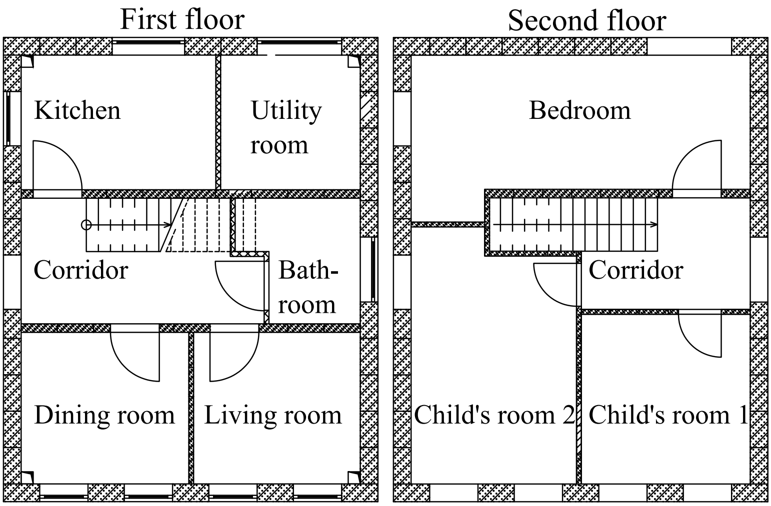

Figure 3.4: The plan of the LLEC building at KIT. Figure is from Langner and Kovačević et al. (2025).

3.1.3 Results and discussion

Input data used for validation are represented in Figure 3.5, where the weather data - ambient temperature T_amb and solar radiation $\dot{q}_\mathrm{sol}$ are shown on the top subplot and the heat flow from the heat pump for the corresponding room on the bottom subplot. Figure 3.6 illustrates the indoor air temperature dynamics in rooms 4 and 5 and the bathroom during the validation period. The measured temperature is shown in blue, while predictions from the ensemble and classic models are shown in red and yellow, respectively. Moreover, weekend periods are shaded in gray.

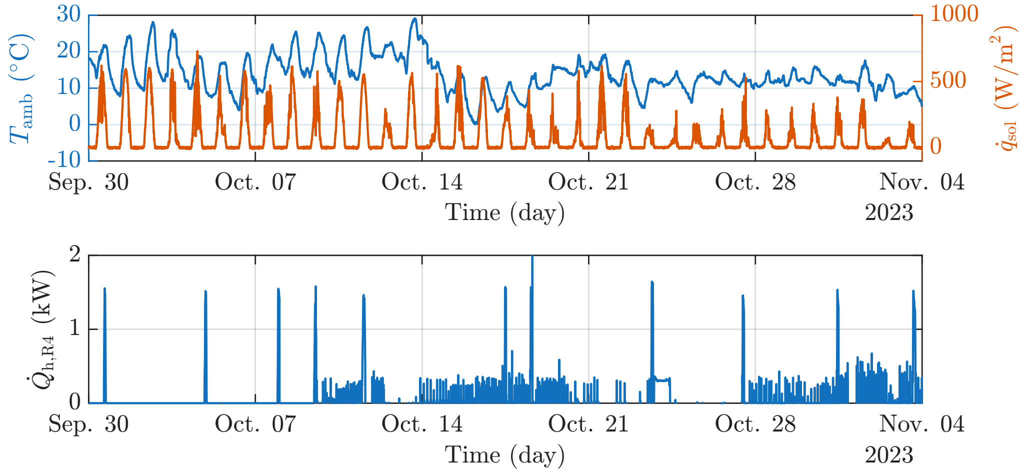

Figure 3.5: Weather and heat flow input data for room 4. The figure is derived from Kovačević et al. (2024a).

Each room is modeled using the system of differential equations defined in Equations (3.1)-(3.4). By separating model identification into working days and weekends, the ensemble model achieves improved forecasting accuracy. Although the ensemble model initially overestimates indoor temperature during the first four days, it better captures system dynamics throughout the remainder of the validation period compared to the classical model. Due to the time-invariant nature of the state-space formulation, the classical model struggles to account for unmeasured time-varying disturbances, particularly during weekends (October 7–8, 14–15, 21–22, 28–29) and certain working days (October 16–20, October 30 – November 3). In contrast, the ensemble model, which comprises two separately identified models, demonstrates greater capability to adapt to temporal variations in OB patterns.

Key performance indicators

To evaluate the predictive accuracy of the proposed ensemble model for indoor air temperature, three statistical metrics are employed: (i) RMSE, which is sensitive to outliers, (ii) MAE, representing the average deviation between predicted and observed values and (iii) MAPE, expressing error as a percentage of actual values. Table 3.1 summarizes the error analysis for both identification and validation periods across all rooms. During validation, the ensemble model consistently outperforms the classic model according to all three indicators. Specifically, MAPE for the ensemble model ranges from 1.4–2.8%, compared to 2.9–5.3% for the classic model. MAE spans 0.32–0.53 °C versus 0.65–1.13 °C, while RMSE is slightly higher for both models due to its sensitivity to outliers, 0.43–0.89 °C and 0.84–1.41 °C, respectively. The poorest performance

(a) Predicted indoor air temperatures for room 4.

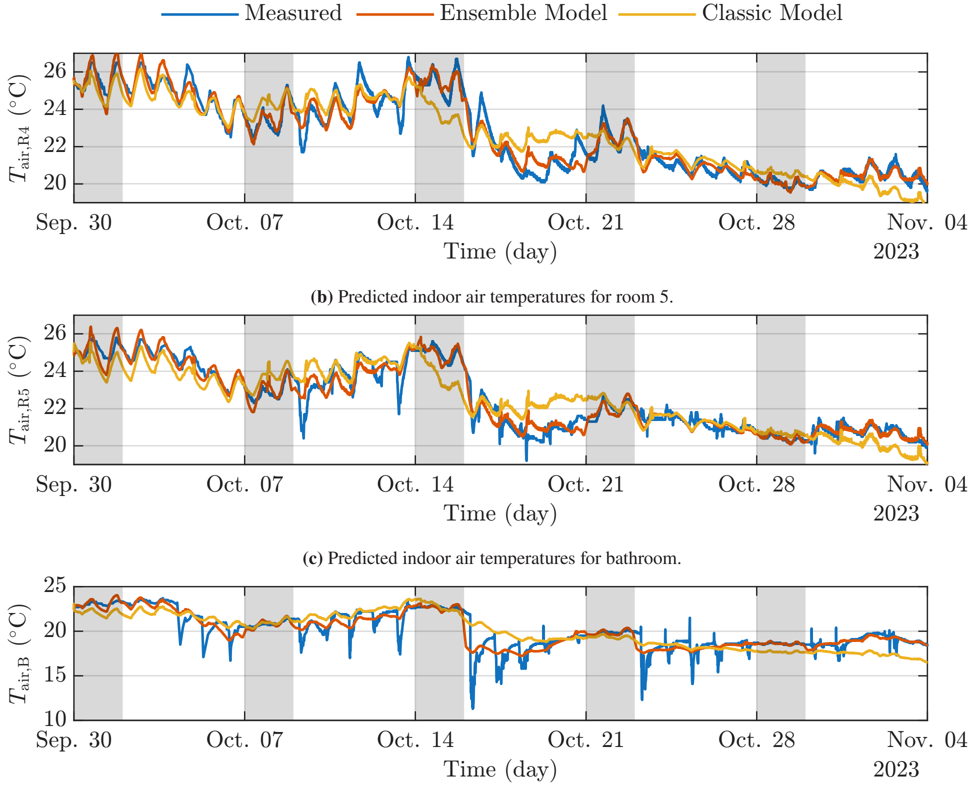

(b) Predicted indoor air temperatures for room 5.

(c) Predicted indoor air temperatures for bathroom.

Figure 3.6: Prediction and measurements for three rooms. Gray-shaded regions correspond to weekends.

occurs in the bathroom, where rapid temperature drops driven by unmeasured disturbances are not captured by either model (see Figure 3.6c). During identification, the classic model performs better only in room 5. However, the ensemble model achieves superior accuracy in all other rooms during the identification period. Interestingly, during validation of room 5 (see Figure 3.6b), the ensemble model yields lower errors, despite its initial disadvantage under the classic model during identification.

Distribution of prediction residuals

Beyond statistical metrics, residual distributions are examined using histograms for all rooms and both models, with Euclidean norm comparisons within and across model classes, as illustrated in Figure 3.7. Residuals exhibit stochastic rather than systematic behavior, influenced by weather and occupancy. In all cases, the ensemble model aligns more closely with a normal distribution

Table 3.1: Indoor air temperature error analysis. The MAE, RMSE and MAPE of classic and ensemble models for the identification and validation period for all zones. Table is derived from Kovačević et al. (2024a).

		MAE (°C)	RMSE (°C)	MAPE (%)	MAE (°C)	RMSE (°C)	MAPE (%)
Zone	Algorithm	Identification period			Validation period		
Room 1	Classic	0.3549	0.4145	1.3840	1.1311	1.3774	5.0135
	Ensemble	0.2550	0.3098	0.9995	0.4247	0.5842	1.9082
Room 2	Classic	0.4469	0.5606	1.7427	0.8928	1.1046	3.7803
	Ensemble	0.4196	0.5431	1.6526	0.3912	0.5026	1.6710
Room 3	Classic	0.6363	0.8305	2.5114	0.8065	1.0126	3.6309
	Ensemble	0.4658	0.5915	1.8482	0.4684	0.6421	2.0650
Room 4	Classic	0.4747	0.5514	1.8675	0.7139	0.9051	3.1753
	Ensemble	0.3482	0.4150	1.3769	0.3463	0.4576	1.5125
Room 5	Classic	0.3864	0.5028	1.5842	0.6529	0.8446	2.9213
	Ensemble	0.4121	0.5200	1.6906	0.3219	0.4282	1.4230
Kitchen	Classic	0.5604	0.7593	2.2440	0.8727	1.1015	3.7413
	Ensemble	0.5277	0.7445	2.1086	0.4349	0.6315	1.8676
Bathroom	Classic	0.7293	1.1242	3.5351	0.9972	1.4081	5.3254
	Ensemble	0.6939	1.0876	3.3665	0.5307	0.8856	2.8292

than the classic model. For room 4, 95% of residuals fall within -1.77 to 1.77 °C for the classic model and -0.89 to 0.89 °C for the ensemble model, indicating higher precision. Corresponding standard deviations are 0.91 °C and 0.46 °C, respectively, with near-zero means for both models. The smaller ensemble model deviation confirms its superior accuracy. To assess histogram similarity, a Euclidean-norm-based index was defined and visualized as a heatmap (see Appendix B.1 Figure B.1). The distance matrix is symmetric and excludes self-comparisons. Overall, histograms within the same model class, ensemble (EM_i, EM_j) or classic (CM_i, CM_j), exhibit high similarity, whereas cross-model comparisons (EM_i, CM_j) show the greatest divergence. Specifically, ensemble-to-ensemble (EM_i, EM_j) distances range from 363 to 1303 (mean: 785; median: 884), while cross-model (EM_i, CM_j) distances span 1395 to 3510 (mean: 2284; median: 2237). Classic-to-classic (CM_i, CM_j) comparisons fall between 685 and 1972 (mean: 1148; median: 1290). The smaller norms in the ensemble group show greater internal consistency than those of the classic model.

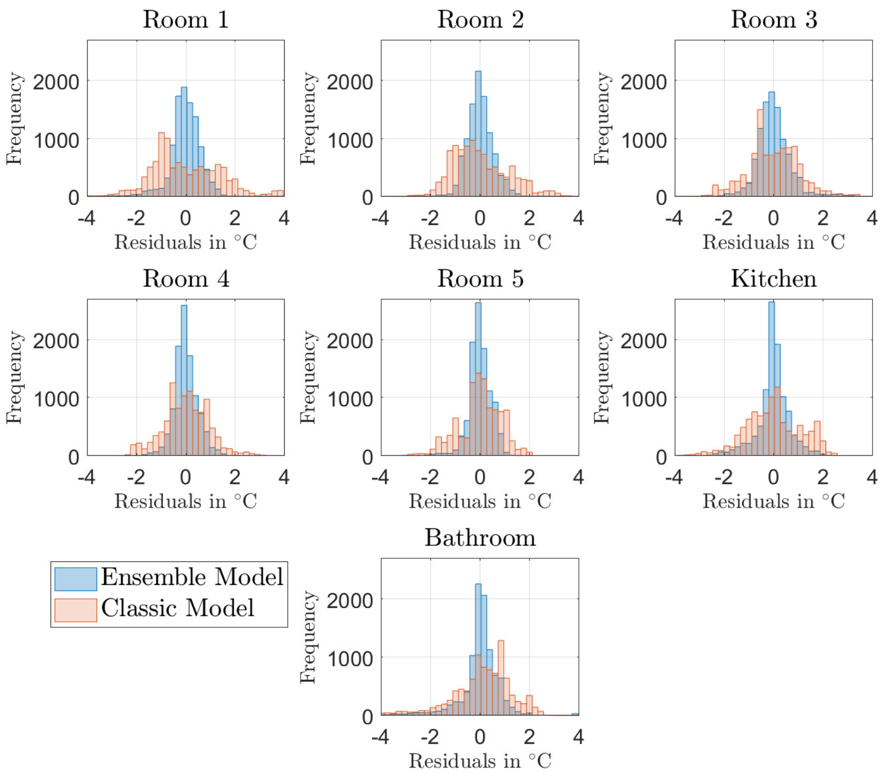

Figure 3.7: Residual error distributions for the classic and ensemble models across all zones. The figure is from Kovačević et al. (2024a).

Transmission heat flow across building envelope

Indoor air temperature T_{air} forecasts were used to quantify transmission heat gains and losses through external walls and roofs across all zones. Heat transfer through the building envelope comprises conduction, convection, and radiation. Calculations are performed at each time step, where convection and radiation effects are assumed to be negligible. Consequently, conductive heat transfer is computed using Fourier's law:

$$\dot{Q}_{\text{cond},k} = \frac{\lambda \cdot A \cdot \Delta T_k}{d} \tag{3.7}$$

where λ in $\mathrm{W/(mK)}$ and denotes thermal conductivity, A in m^2 is the surface area of walls and roofs, d in m is the thickness, and ΔT_k the temperature difference between indoor and ambient air at timestep k. Figure 3.8a compares the time-step differences in conductive heat power between measurements and forecasts from the classic model (left) and the ensemble model (right). For the ensemble model, the interquartile range (IQR) spans -43 W to 40 W, compared to -95 W to 76 W for the classic model. Positive values indicate heat loss, negative values heat gain.

(a) Time-step difference between conductive heat transfer through the external walls and the roof of measurement data and both ensemble and classic model forecasts summed for all zones.

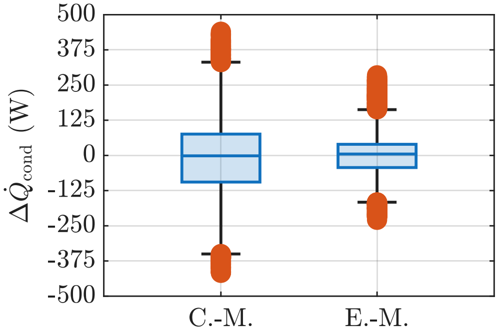

(b) Difference in conductive energy between measurements and model forecasts through external walls and roof, aggregated across all zones.

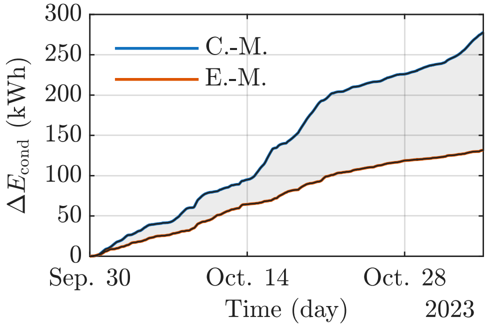

Figure 3.8: Transmission heat across building envelope. Abbreviations stand for: C. - classic, E.- ensemble, and M.- measurements. Figures are derived from Kovačević et al. (2024a).

Figure 3.8b shows accumulated prediction errors in heat energy over five weeks: 278 kWh for the classic model versus 132 kWh for the ensemble model. These results demonstrate the ensemble model's superior accuracy and reduced cumulative error in estimating heat transfer $\dot{Q}_{\mathrm{cond}}$ through external walls and roof.

In summary, the small difference between MAE and RMSE indicates stable performance for both models, with no significant outliers. Nevertheless, all three metrics in Table 3.1 confirm that the ensemble model consistently achieves lower forecast errors than the classic model during validation. Heatmap analysis (see Appendix B.1, Figure B.1) demonstrates that the ensemble structure is more resilient to room variability and unmeasured disturbances, such as occupant-related heat loads influencing indoor temperature. Furthermore, accumulated energy errors (see Figure 3.8b) show a reduction of 146 kWh over five weeks, confirming the ensemble model's improved accuracy.

Direct comparison with existing gray-box models is not feasible due to variations in datasets and identification horizons. For reference, Harb et al. (2016) report RMSE of 0.2 for a 26-day identification period, while Gray and Schmidt (2018) and Klanatsky et al. (2023) achieve RMSE of 0.2 °C and MAE of 0.25 °C over the year, respectively, using adaptive parameter updates over 1–4 weeks. The proposed approach segments identification into weekdays and weekends to capture occupancy patterns, requiring one week for accurate five-week forecasts. Compared to the classic model, the ensemble approach reduces all three statistical indicators during validation, demonstrating its superiority for high-precision prediction. However, the ensemble model overestimates temperatures sometimes (see Figure 3.6a) due to ambient fluctuations and heat pump inactivity. Similarly, rapid temperature drops in the bathroom (see Figure 3.6c) represent unmodeled disturbances, as both models fail to capture fast dynamics. Room 5 exhibits mixed results: the classic model performs better during identification, while the ensemble model excels in validation (see Table 3.1). These discrepancies may stem from complex occupancy patterns and minimal solar gains in room 5, the largest room facing northwest.

3.2 Analysis: Impact of model complexity reduction on heating system dynamics

For large-scale simulations and model-based control design, it is essential to employ system models that are sufficiently simple to minimize computational costs yet accurately capture the system's dynamic behavior. This part of the dissertation examines how reducing model complexity affects simulation accuracy using a real-world residential heating system as a case study. To conduct this analysis, a high-detail reference model is first developed and validated using data from a real-world facility. Subsequently, systematic reduction steps are applied to the validated model, and the simulation accuracy of the simplified models is evaluated. The core contribution lies in a detailed evaluation of how white-box model simplification impacts overall heating system model performance. The present case study employs vertical reduction within the white-box modeling approach, as illustrated in Figure 3.1.

3.2.1 Methodology

Modelica language and its commercial software, Dymola, are chosen for modeling the building heating system. The open-source library AixLib (Maier et al. 2024) is selected because it incorporates all necessary components and models at varying levels of detail and provides comprehensive documentation. Moreover, AixLib is widely used in the field of building energy modeling (Mork et al. 2022, Schneider et al. 2017, Urrutia et al. 2025). To investigate the reduction potential, it is essential to create a suitable reference model. The system has been designed to be as realistic as possible, with components for the model being provided by the AixLib library and characterized by high levels of detail. Henceforth, the reference model is validated on real-world data. This process is followed by the exploration of reduction possibilities within Modelica and AixLib.

The real-world heating system from Meyer (2013) is selected as a case study. It comprises three main components: a heat pump and two storage tanks for DHW and space heating. The initial step in the modeling process is selecting the most detailed components from AixLib that correspond to the real heating system description. The following models are chosen: (i) `Fluid.HeatPumps.ScrollWaterToWater` for the ground-source heat pump, (ii) `Fluid.Storage.StratifiedEnhanced` for the space heating storage and (iii) `Fluid.Storage.StratifiedEnhancedInternalHex` for the DHW storage. The comprehensive description of the corresponding models coupling follows in Section 3.2.2. Subsequently, the reduction steps are undertaken utilizing the reference model as a foundation, as shown in Figure 3.9.

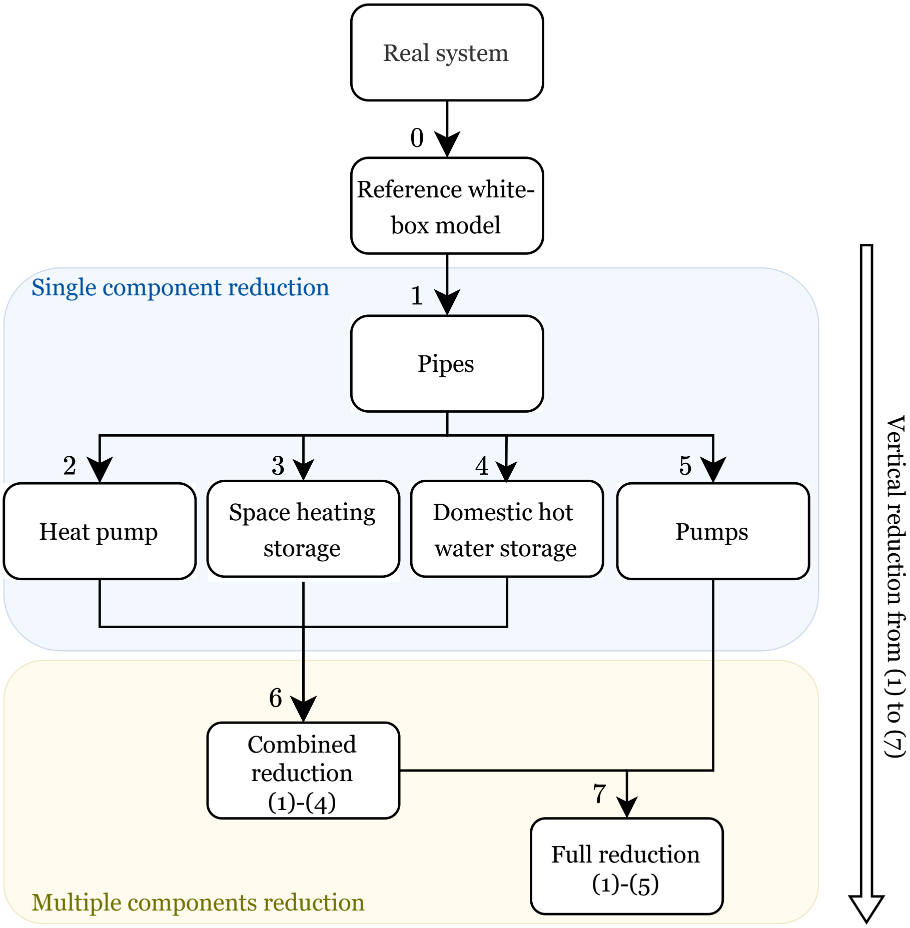

Figure 3.9: Model reduction methodology of the white-box residential heating system model consisting of seven reduction steps. Figure is adapted from Kovačević et al. (2025a) and Brecher (2024).

The potential for reducing the complexity of a modeled heating system has been identified in omitting or simplifying specific components, namely the heat pump, thermal energy storage systems, piping network, and circulation pumps. In the initial reduction step (reduction step one), only the piping system is excluded. Steps two through five involve the simplification of individual components: the heat pump, space heating storage, DHW storage, and circulation pumps. Herein, each reduction step replaces only one component from the reference model with a less detailed representation. In step six, simplified models of the heat pump and both storage units are integrated. Finally, step seven further reduces model complexity by incorporating all previous simplifications.

As illustrated in Table 3.2, the detailed components of AixLib that are utilized in the reference model are outlined, along with their simpler replacement models and corresponding reduction steps. For instance, the simpler replacement model `Carnot_y` of the heat pump is employed in the reduction steps 2, 6, and 7. In contrast, the detailed model `ScrollWaterToWater` is utilized in the remaining steps. It should be noted that only the latter part of the components' description is used hereafter, e.g. `StratifiedEnhanced` for space heating storage detailed component from AixLib.

Table 3.2: A list of reference model components and their simplified replacements, along with the steps in which they are simplified. The heat pump, space heating storage, DHW storage, and circulation pumps components are in `AixLib.Fluid` respective sublibraries `HeatPumps`, `Storage`, `Movers`. Simplified circulation pumps are available in `Modelica.Fluid.Sources`. Table is adapted from Kovačević et al. (2025a).

Component	Reference model name	Simpler model name	Reduced in step
Heat pump	`ScrollWaterToWater`	`Carnot_y`	2, 6, 7
Space heating storage	`StratifiedEnhanced`	`Stratified`	3, 6, 7
DHW storage	`StratifiedEnhanced-InternalHex`	`Storage`	4, 6, 7
Pumps	`FlowControlled_m-_flow`	`MassFlowSo-urce_T`	5, 7

3.2.2 Case study

Reference heating system model

The development of the reference residential heating system model is approached via a bottom-up strategy, wherein components from AixLib are selected as the most complex models, exhibiting the highest level of detail. Figure 3.10 illustrates the reference heating system model. The dashed lines indicate the subsystems relevant to the present case study. The remaining subsystems are shown for completeness but are not explained in detail. The systems' core components are a heat pump and two stratified storage systems for space heating and DHW.

The green block in Figure 3.10 denotes the heat pump system, comprising two major subsystems: the water-to-water ground source heat pump and the brine circulation pump, named `heatPump` and `pumpBrine`, respectively. The heat pump employs a scroll-type compressor, while the brine fluid is a mixture of water and ethylene glycol with a 20 % concentration. The `ScrollWaterToWater` heat pump is selected because it aligns with the real-world system and is the highly detailed model in AixLib. For the brine circulation pump, the `FlowControlled_m_flow` is applied, and measured brine temperature data are used as input to the simulation. A refrigerant model for R134a is implemented using the hybrid equation-based approach described by Sangi et al. (2014). Since the geothermal borehole is not explicitly modeled, two boundary conditions are defined to represent temperature and pressure constraints, i.e., `sourceGround` and `sinkGround` components.

The yellow block in Figure 3.10 depicts the space heating storage system. The heated water from the heat pump is transferred into the space heating storage (named `storageSH`) with the assistance of the circulation pump `pumpSH`. The type of the circulation pump utilized from AixLib is `FlowControlled_m_flow`. For the space heating storage component, the detailed `StratifiedEnhanced` model is chosen for the reference model. Furthermore, the heating distribution system is presented as a boundary condition in Figure 3.10, marked as `sinkSH` in the yellow block. The pipelines for supply and return water, named `pipeSHSupply` and `pipeSHReturn`, respectively, are represented with `Fluid.FixedResistances.PressureDrops` components. The three valves modeled with `Fluid.Actuators.Valves.TwoWayQuickOpening` are used for water distribution. The representation of valve control is illustrated in the orange block. Due to the absence of direct measurements for the volume flow rate of the circulation pump `pumpSHRad`, which transports heated water to the radiators and to the boundary condition in the simulation, the flow rate is approximated using the temperature difference between the radiator inlet and outlet. This subsystem is visually indicated with a brown background in Figure 3.10. An additional simplification applied to this component is the omission of the three-way valve present in the actual installation (Meyer 2013), as its control logic is not documented.

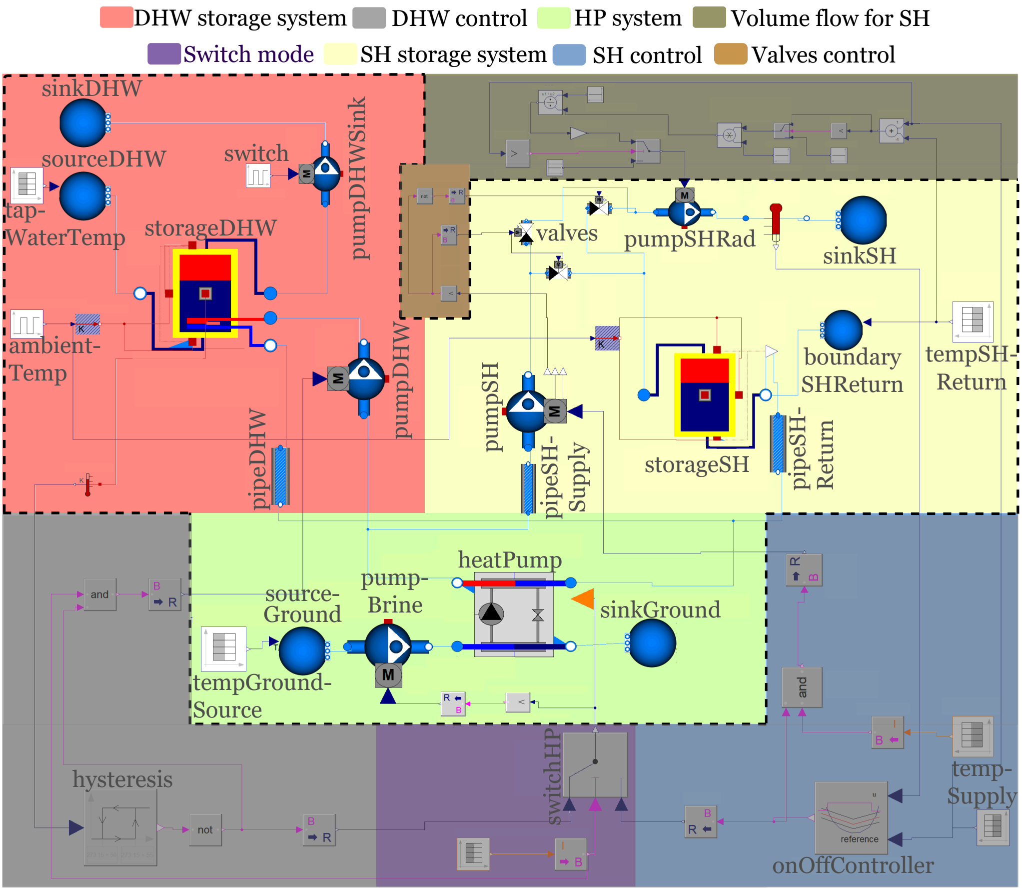

Figure 3.10: The reference heating system model, based on a real-world facility from Meyer (2013). The subsystems relevant to the introduced model reduction are outlined by the dashed lines. The figure is adapted from Kovačević et al. (2025a) and Brecher (2024).

Similarly to the space heating subsystem, the DHW storage subsystem is illustrated within the red block in Figure 3.10. The heated water from the heat pump is transported into the DHW storage (named `storageDHW`) internal heat exchanger by the circulation pump named `pumpDHW`. The pump component is of the same type as the two pumps previously referenced. The `StratifiedEnhancedInternalHex` is the AixLib component utilized for the indirect stratified storage for DHW. Furthermore, the boundary conditions `Fluid.Sources.Boundary_pT` for the drinking water sink `sinkDHW` and the freshwater inlet temperature `sourceDHW` from measurements are utilized. The volume flow of drinking water $\dot{V}_{\mathrm{DHW}}$ (m^3/s) is calculated based on the measured heat flow for each heating cycle of drinking water $\dot{Q}_{\mathrm{DHW}}$ (W), the density $\rho_{\mathrm{H_2O}}$

$(\mathrm{kg/m^3})$ and specific heat capacity $c_{\mathrm{H_2O}}$ $(\mathrm{J/kg \cdot K})$ of the water and temperature difference between tap and heated water of the DHW ΔT_{DHW} measured in K:

$$\dot{V}_{\mathrm{DHW}} = \frac{\dot{Q}_{\mathrm{DHW}}}{\rho_{\mathrm{H_2O}} \cdot c_{\mathrm{H_2O}} \cdot \Delta T_{\mathrm{DHW}}} \tag{3.8}$$

As described by Meyer (2013), the DHW storage is scheduled for heating every two days for 24 h, with no heating during the weekends. Since there is no information on occupant behavior within the building, the DHW load distribution is estimated utilizing a pulse signal with a 16 $\mathrm{h/day}$ time span. This estimation corresponds to the household demand for two days, $V_{\mathrm{DHW}} = 0.36\,\mathrm{m^3}$. The blue, gray, and purple block in Figure 3.10 depict the space heating supply control, DHW supply control and control between two modes (space heating or DHW), respectively. The on/off controller `Modelica.Blocks.Logical.OnOFFController` is utilized for controlling the heat pump for space heating, while the DHW storage charging is controlled by hysteresis `Modelica.Blocks.Logical.Hysteresis`. A comprehensive description of the components can be found in Maier et al. (2024).

Reduction steps

The pipelines, named `pipeSHSupply`, `pipeSHReturn`, and `pipeDHW` in Figure 3.10, are neglected in the first reduction step (see Figure 3.9). The second step reduces the `ScrollWaterToWater` heat pump by replacing it with simpler `Carnot_y` (see Table 3.2). In terms of model complexity, this replacement reduces the number of equations, as the power consumption and heat flows of the heat pump are calculated more simply than in the reference model. The reduction step three reduces the space heating storage `StratifiedEnhanced` to `Stratified` AixLib component. In this context, the difference between the components mentioned above lies in how the stratification is carried out. In the reference space heating storage `StratifiedEnhanced`, a third-order stratifier is utilized, whereas in the simpler component `Stratified`, stratification is designed as individual fluid volumes. This contributes to reducing the number of unknowns and equations. In the reduction step four, `StratifiedEnhancedInternalHex` is replaced by `Storage`, within the DHW subsystem. These two components are chosen as both can implement the heat exchanger, which aligns with the real system. Moreover, the simpler `Storage` component has simplified stratification. The circulation pumps are replaced with simpler `MassFlowSource_T` components from the Modelica main library (see Table 3.2) in step five. Due to the physical meaning of the simpler `MassFlowSource_T`, as they can be located only at the end of the connection, the `pumpSH` and `pumpDHW` are still modeled with `FlowControlled_m_flow`. The reduction step six combines reduced heat pump, space heating storage, DHW storage, and pipeline neglect. The last reduction step combines all single component reduction steps (1)-(5) (see Table 3.2).

Measurements

The measurements serve as inputs for the model's boundary conditions and for validation of the residential building heating system located in Switzerland (Meyer 2013). The boundary conditions are derived from measurement data: (i) the ground probe temperature - the input to the brine circulation pump, (ii) the space heating return temperature of water - the input to the space heating storage, and (iii) the fresh water inlet temperature - the input to DHW storage. On the other hand, for the model validation, the following measurements are used: (i) the total electricity consumption - calculated as the sum of the consumption of the corresponding components, and (ii) COP - calculated based on the generated heat power and the consumed electricity.

3.2.3 Results and discussion

For the quantitative evaluation of the reference model and models derived from all reduction steps, the RMSE, which is sensitive to outliers, and the MAE, which defines the average error are utilized. The models are evaluated utilizing power consumption and COP measurements for the entire year of 2022. The following three cases regarding the power consumption and COP are discussed: (i) total power consumption including the consumption of the circulation pumps P_{T} and the corresponding $\mathrm{COP}_{\mathrm{T}}$ over $15\,\mathrm{min}$ time step, (ii) power consumption $P_{\mathrm{el,HP}}$ and $\mathrm{COP}_{\mathrm{HP}}$ of only heat pump in $15\,\mathrm{min}$ resolution and (iii) average power consumption $P_{\mathrm{el,HP,24h}}$ and average $\mathrm{COP}_{\mathrm{HP,24}}$ per day. Furthermore, the deviations between the reference model and reduced models, namely Δ_{RMSE} and Δ_{MAE}, are discussed. The reduction is evaluated as the decrease in the number of unknowns and equations of the system represented by the Differential-Algebraic System of Equations (DAE). The number of unknowns and equations in the DAE is independent of the computer's characteristics or state, and thus serves as an objective metric for evaluating the model's complexity. In addition, computational costs are evaluated based on Central Processing Unit (CPU) time. As the simulation's CPU time depends on the computer's performance and overall utilization, the average CPU time across three simulation runs is calculated.

Reference model and final reduction model validation

Figure 3.11 presents the accuracy of the reference model and final reduction model, i.e., the model at reduction step seven. Two types of error are shown: RMSE, sensitive to outliers, and MAE, representing the mean error. The MAE of the power consumption $P_{\mathrm{el,HP}}$ for the reference model is $268.8\,\mathrm{W}$, which is considered relatively accurate for a one-year evaluation. This deviation could occur because the volume flows for space heating and the DHW are estimated rather than measured. Moreover, neglecting the three-way valve can also contribute to discrepancies between the model and measurements. The temporal shift between the simulation and measurements,

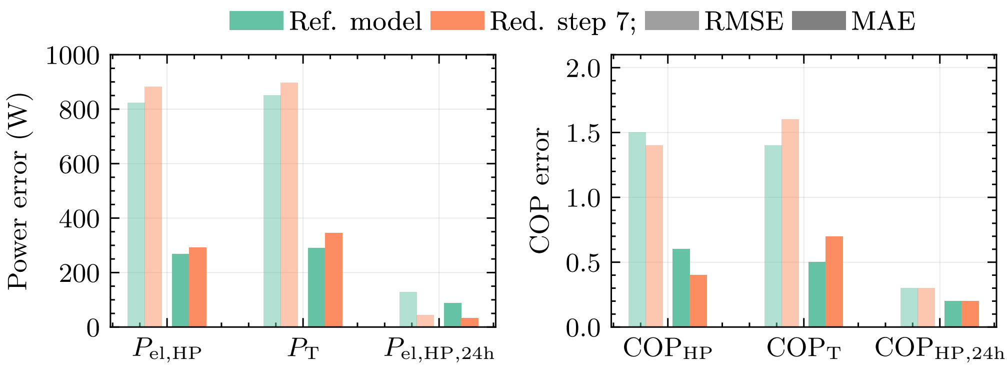

Figure 3.11: Error analysis for the reference model and the model at the reduction step seven, evaluated for the entire year of 2022. Models are compared with the measurement. The transparent bars represent the RMSE, while bars with no transparency show the MAE.

due to the lack of measurement data, can reflect in a relatively large RMSE of $P_{\mathrm{el,HP}}$ 823.4 W. Specifically, the simulation may not reflect the correct time at certain time steps. In these instances, the measurements may show zero power consumption, whereas the simulation could result in 4.5 kW in the worst case. This temporal shift arises from gaps in the measurement data utilized as the simulation input. Furthermore, this temporal shift is also evident in the reduced model in step seven (see the orange bars of $P_{\mathrm{el,HP}}$ in the Figure 3.11). The evaluation excludes the two most significant measurement gaps; however, many smaller gaps cannot be addressed in this way. Interestingly, when considering the RMSE of average power consumption per 24 hours, both models have significantly smaller RMSE. Namely, RMSE of 128.4 W for the reference model and 43.6 W for the model from the reduction step seven. Notably, the impact of the temporal shift vanishes when averaging power consumption over a 24 h time span $P_{\mathrm{el,HP,24h}}$. The same applies to COP. The average $\mathrm{COP}_{\mathrm{HP,24h}}$ RMSE is significantly smaller than the RMSE of $\mathrm{COP}_{\mathrm{HP}}$ and $\mathrm{COP}_{\mathrm{T}}$ as shown in the Figure 3.11 in the right subplot. In particular, the RMSE of $\mathrm{COP}_{\mathrm{HP}}$ is 1.5 and 1.4 for the reference and reduced models in step seven, respectively, while the RMSE of $\mathrm{COP}_{\mathrm{HP,24h}}$ is 0.3 for both models. This leads to reductions of 1.2 and 1.1 in RMSE compared to $\mathrm{COP}_{\mathrm{HP}}$ for the reference model and the most reduced model, respectively. Furthermore, the RMSE of $\mathrm{COP}_{\mathrm{T}}$ for reference and model from reduction step seven are 1.4 and 1.6, respectively. In addition to the previously discussed factors contributing to deviations in power consumption, which also influence the COP, further discrepancies in COP may arise from the omission of thermal losses in the storage system. As a result, the simulated heat output of the heat pump exceeds that of the actual facility. Moreover, the observed difference between the heat pump power consumption $P_{\mathrm{el,HP}}$ and the total power consumption P_{T} in the compared models stems from the

Table 3.3: The power difference between the reference model and the models from all reduction steps. Negative values denote that the corresponding model aligns better with measurements. The table is derived from Kovačević et al. (2025a) and Brecher (2024).

Reduction step	Power	Δ_{RMSE}	Δ_{MAE}
1	$P_{\mathrm{el,HP}}$ in W	1.2	-0.2
	$P_{\mathrm{el,HP,24h}}$ in W	2.7	0.8
2	$P_{\mathrm{el,HP}}$ in W	52	20.3
	$P_{\mathrm{el,HP,24h}}$ in W	-90.8	-61
3	$P_{\mathrm{el,HP}}$ in W	3.6	2.2
	$P_{\mathrm{el,HP,24h}}$ in W	-4.7	-2.6
4	$P_{\mathrm{el,HP}}$ in W	7.2	6.5
	$P_{\mathrm{el,HP,24h}}$ in W	-3.7	-2.1
5	$P_{\mathrm{el,HP}}$ in W	2	1.3
	$P_{\mathrm{el,HP,24h}}$	-0.9	-0.7
6	$P_{\mathrm{el,HP}}$ in W	53.6	20.4
	$P_{\mathrm{el,HP,24h}}$ in W	-83.5	-53.9
7	$P_{\mathrm{el,HP}}$ in W	58.5	23.5
	$P_{\mathrm{el,HP,24h}}$ in W	-84.8	-55.2

inclusion of circulation pump energy use in the latter, which is not explicitly parameterized in the current modeling approach.

Model accuracy for reduction steps

Tables 3.3 and 3.4 show the deviation of RMSE Δ_{RMSE} and MAE Δ_{MAE} between the reference model and reduced models for power consumption and COP, respectively. Here, the negative values indicate greater alignment with the real-world facility. The first reduction step (see Figure 3.9) does not result in significant deviations from the reference model, since both Δ_{RMSE} and Δ_{MAE} are relatively small values. Therefore, in all subsequent reduction steps, the same pipes are neglected. The reduction step one comprises 2784 unknowns and equations of the DAE, reducing the model complexity by 1.7% compared to the reference model, as shown in Figure 3.12.

The reduction step two, comprising the replacement of the detailed heat pump `ScrollWater-ToWater` with simpler `Carnot_y` model, results in the $P_{\mathrm{el,HP}}$ and $\mathrm{COP}_{\mathrm{HP}}$ Δ_{RMSE} of 52 W and

Table 3.4: The COP difference between the reference model and the models from all reduction steps. Negative values denote that the corresponding model aligns better with measurements. The table is derived from Kovačević et al. (2025a) and Brecher (2024).

Step	COP	Δ_{RMSE}	Δ_{MAE}
1	$\mathrm{COP}_{\mathrm{HP}}$	1.2	-0.2
	$\mathrm{COP}_{\mathrm{HP,24h}}$	0	0
2	$\mathrm{COP}_{\mathrm{HP}}$	-0.1	-0.1
	$\mathrm{COP}_{\mathrm{HP,24h}}$	0	0
3 - 5	$\mathrm{COP}_{\mathrm{HP}}$	0	0
	$\mathrm{COP}_{\mathrm{HP,24h}}$	0	0
6 - 7	$\mathrm{COP}_{\mathrm{HP}}$	-0.1	-0.1
	$\mathrm{COP}_{\mathrm{HP,24h}}$	0	0

-0.1, respectively. Interestingly, the deviations Δ_{RMSE} and Δ_{MAE} of $P_{\mathrm{el,HP,24h}}$ and $\mathrm{COP}_{\mathrm{HP}}$ are negative, showing that the model accuracy is closer to the measurements. The $P_{\mathrm{el,HP,24h}}$ and $\mathrm{COP}_{\mathrm{HP,24h}}$ values reduce the influence of the time shift by averaging the consumption over one day. The compressor, which is not modeled in the reduced heat pump, is likely the reason for the better accuracy of the reduction step two, given the average consumption $P_{\mathrm{el,HP,24h}}$. The difference between the reference model and the model in the reduction step two lies in the consumed power, which is modeled as the nominal compressor power in the latter model. Consequently, the calculated heat flow from the heat pump is smaller than that of the reference model. This aligns the model from the reduction step two closer to the measurements. However, the number of unknowns and equations of DAE is reduced by 4.6% compared to the reference model, which is not yet significant. The replacements of the space heating storage, the DHW storage, and the circulation pumps separately in the reduction steps three to five have been shown to have a negligible impact on model accuracy. The respective values of Δ_{MAE} of $P_{\mathrm{el,HP}}$ are 2.2 W, 6.5 W and 1.3 W, respectively. Furthermore, there is no deviation of Δ_{MAE} for $\mathrm{COP}_{\mathrm{HP}}$ and $\mathrm{COP}_{\mathrm{HP,24h}}$ between the reference model and the above-mentioned reduction steps. Interestingly, reduction step four yields a substantial decrease in the number of unknowns and equations in the DAE, amounting to 23.2% compared to the reference model. This demonstrates that simplifying the DHW storage significantly reduces the model complexity, as measured by the number of unknowns and equations in the DAE. A comparable effect is observed in step five, where simplifying circulation pumps results in a 13.6% reduction. Furthermore, reduction step six, which integrates the reduced heat pump, DHW, and space heating storages, the deviation from the reference model aligns with that of reduction step two, with Δ_{RMSE} values of 53.6 W and -83.5 W for $P_{\mathrm{el,HP}}$ and $P_{\mathrm{el,HP,24h}}$, respectively. This outcome is plausible as the reduced heat pump model exerts the most pronounced influence on simulation accuracy. Moreover, the reduction of the DAE number of unknowns and equations of 29.4% is justified as it aggregates reduced components from steps one to four. The reduction step seven, which combines the simplified circulation pumps with the reduced models from step six, results in a slight deviation in accuracy relative to the reference model compared to step six. This corresponds to Δ_{RMSE} values of 58.5 W and -84.8 W for $P_{\mathrm{el,HP}}$ and $P_{\mathrm{el,HP,24h}}$ respectively, while COP values remain largely unaffected. The final reduction step involves 1664 unknowns and equations in the DAE, resulting in a 41.3% reduction in DAE unknowns and equations compared to the reference model, as illustrated in Figure 3.12.

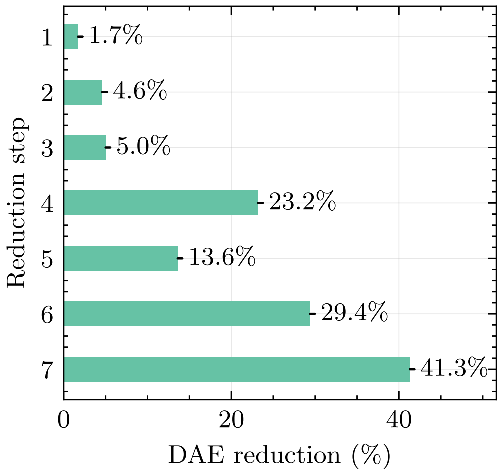

Figure 3.12: Model reduction in percentage relative to the reference model, which comprises 2833 unknowns and equations of the DAE. The figure is derived from Kovačević et al. (2025a) and Brecher (2024).

Computational costs

Figure 3.13 presents the averaged CPU time of three simulation runs for the reference model and each reduction step. The computer used for the simulation has Intel® Core™ i7-1255U CPU@1.70GHz with 16GB installed RAM. The solver in Dymola environment is Dassl (Petzold 1982) with a tolerance of 0.01. Remarkably, the reduced model in step two has the most significant impact on CPU time, achieving a 91.7% reduction compared to the reference model. This substantial decrease can be explained by the fact that the simplified heat pump model `Carnot_y` excludes the compressor and considers only heat-exchange processes, i.e., the condenser and evaporator. The compressor power is derived from the heat pump performance curve, rendering the heat pump component computationally more efficient. Reduced models from steps one, three, and four also contribute to CPU time reduction, though to a lesser extent, with reductions of 14.6%, 8%, and 6.2%, respectively, compared to the reference model. Interestingly, simplifying circulation pumps in step five does not reduce the average CPU time, despite a 13.6% reduction in the number of DAE unknowns and equations. In fact, this model from the reduction step five requires, on average, 125.5 s more than the reference model. Steps six and seven have nearly identical average CPU times, i.e., 59.8 s and 59.7 s, respectively. These two reduction steps have the most significant impact on CPU time reduction, i.e., 94.9% for both. They combine the most extensive DAE simplifications with the greatest CPU time savings. However, for models from steps one to five, CPU time does not consistently correlate with the percentage reduction in DAE unknowns and equations. For instance, while step four achieves the largest DAE reduction, step two delivers the smallest CPU time. This discrepancy may stem from component-specific structures, such as the heat pump model discussed earlier. Still, it could also relate to solver characteristics, simulation management, C-code generation, and optimization strategies. These factors require further investigation.

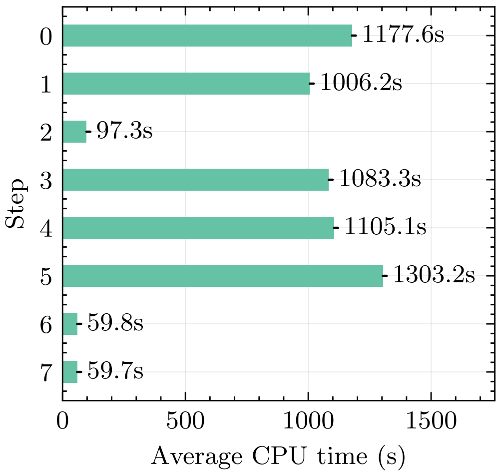

Figure 3.13: The average CPU time (s) of the reference mode and all models from reduction steps. The average CPU time is calculated based on the results of three simulation runs. The figure is derived from Kovačević et al. (2025a).

Heat pump power consumption

Figure 3.14 comprises the comparison of a daily average heat pump power consumption, $P_{\mathrm{el,HP,24h}}$, to mitigate temporal shift effects and better evaluate model dynamics against measurements. Notably, the model from the reduction step seven demonstrates superior accuracy

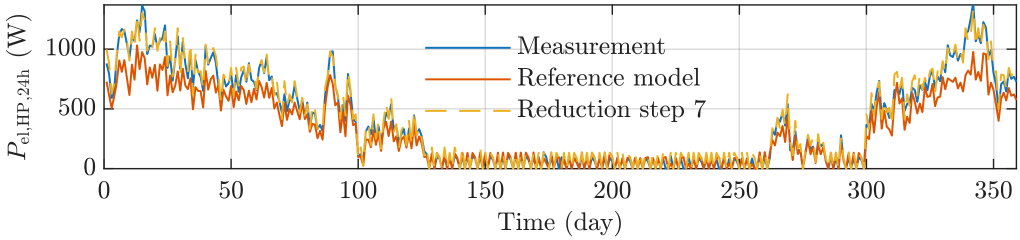

Figure 3.14: Heat pump power consumption averaged on 24 h for the entire evaluation period. The figure is derived from Kovačević et al. (2025a) and Brecher (2024).

in average consumption, particularly during winter. This improvement arises from deviation in heat flow simulation between the detailed `ScrollWaterToWater` and simplified `Carnot_y` heat pump models, with the latter exhibiting lower efficiency and therefore yielding electrical power consumption closer to that observed in the real facility. However, similar conclusions cannot be drawn from $P_{\mathrm{el,HP}}$ and P_{T} due to uncompensated temporal shifts.

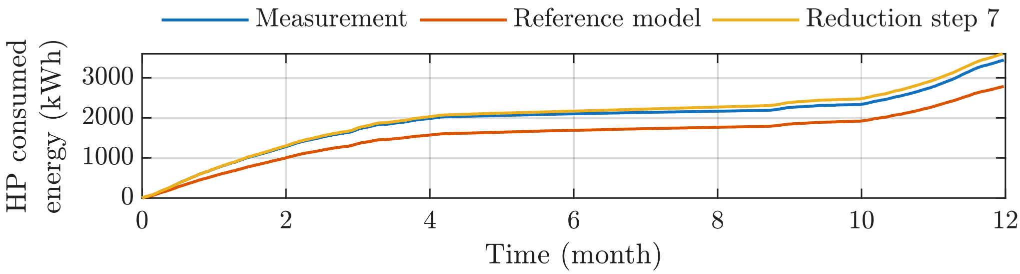

Figure 3.15: Consumed energy of the heat pump for the year 2022. The figure is derived from Kovačević et al. (2025a) and Brecher (2024).

Figure 3.15 illustrates the annual accumulated energy consumption of the heat pump for the year 2022. Measurements, reference and most reduced models indicate 3447 kWh, 2785 kWh and 3610 kWh annual consumed energy, respectively. The model from the reduction step seven shows better alignment with the real-world facility, likely because its lower efficiency more closely reflects the actual heat pump performance, possibly influenced by aging effects. However, this observation cannot be generalized, as it is related to the specific condition of the real system. For instance, the detailed `ScrollWaterToWater` model could better represent optimal performance in a new heat pump, as it computes higher heat flows and thus greater efficiency than the simplified `Carnot_y` component.

3.3 Contributions

This chapter addresses the research gaps in the field of building energy modeling by answering the research questions **RQ1** and **RQ2** (see Section 1.2). The RQs examine how uncertainty and complexity reduction affect the accuracy of the building energy models. The first section of this chapter examines uncertainty in occupants' behavior in gray-box reduced-order thermal building models. It addresses **RQ1** by introducing an ensemble approach for parameter identification that accounts for occupants' behavior patterns. Using the proposed methodology, the improved robustness of the gray-box thermal building model against variations in occupants' behavior patterns becomes evident. The contribution of this part lies in (i) analyzing the forecast accuracy of the gray-box thermal building models in occupied buildings identified in a classical way and (ii) proposing the methodology for improving the robustness of the models to changes in occupants' behavior patterns. As the data used for parameter identification and validation are from the German fall period, further development should focus on detailed analysis during winter and summer, when heating (i.e. cooling) demand is much higher. The unmeasured disturbances and their handling by the control algorithm, shown for the bathroom in Figure 3.6c, are addressed later in this dissertation within a real-world experiment (see Section 4.2).

Motivated by the advantages of the simplified models, such as gray-box models, the second part of this chapter examines how complexity reduction influences the dynamic behavior of the building heating system. It is based solely on comparative analysis and addresses **RQ2**. The analysis demonstrates that complex models are not always superior in representing real systems. This part of the dissertation contributes to (i) an in-depth analysis of building heating system models at varying levels of detail, as well as (ii) an assessment of reduction potentials within Modelica and the open-source AixLib library.

4 Fuzzy logic thermal building control

Publications supporting the chapter content

- Jovana Kovačević, et al. A fuzzy logic approach for economic energy-efficient heat pump operation in thermal building control. In 2024 IEEE PES Innovative Smart Grid Technologies Europe (ISGT EUROPE), pages 1–6. IEEE, 2024b. doi: 10.1109/ISGTEUROPE62998.2024.10863470.
- Felix Langner, Jovana Kovačević, et al. Experimental evaluation of model predictive control and fuzzy logic control for demand response in buildings. Applied Energy, 401:126666, 2025. ISSN 0306-2619. doi: 10.1016/j.apenergy.2025.126666.

Demand response, as a subcategory of demand-side management, exhibits significant potential for flexible energy consumption by actively engaging end users and encouraging them to adjust their demand in response to grid conditions over time (Siano 2014, Gelazanskas and Gamage 2014). Load shifting contributes to demand response by rescheduling energy consumption from on-peak to off-peak periods (Gellings 1985). On the other hand, peak shaving, also known as load shedding, aims to temporarily curtail peak load during unfavorable periods in the grid (Gellings 1985).

To integrate demand response into buildings, advanced control strategies that enable flexible HVAC operation are necessary. This dissertation contributes to the field of energy flexibility in buildings by proposing FLC algorithms for demand response programs, addressing **RQ3** and fulfilling **research gap 3**. In the Section 4.1, two FLCs are evaluated in a simulation-based environment. They differ in objective, where one is modeled as comfort-oriented, while the other is economic-oriented. The development and comparison of the two control strategies with opposite characteristics help identify the trade-offs and additional information required for a real-world experiment. Thereafter, Section 4.2 presents a real-world experiment that employs the FLC control strategy for flexible load shifting. To enable the load shifting, day-ahead electricity prices, and predefined temperature constraints are considered. All FLC controller strategies are developed as forecast-[6] and model-free[7] strategies.

4.1 Analysis: Comfort- and economic-oriented thermal building control

In this section, two FLC algorithms with different objectives, comfort- and economic-oriented, are designed for thermal building control in demand response programs. They both contain minimal information required for the operation. In addition to indoor air temperature, they require current dynamic electricity price signals and the current heat pump COP based on the ambient temperature.

4.1.1 Methodology

The Mamdani fuzzy logic controller (see Section 2.2.2) is employed to implement comfort- and economic-oriented control strategies. The minimum operator is applied for set intersections, while the maximum operator is used for set unions. During fuzzification, crisp input values are transformed into fuzzy membership values defined by the corresponding membership functions. The membership functions are designed based on Occupants' Thermal Satisfaction (OTS) levels.

OTS levels are based on the Predicted Mean Vote (PMV) index (Fanger 1970). This index evaluates the thermal comfort of building occupants in the same environment by predicting the mean thermal vote for a large group of people, based on the human body's heat balance. The complementary index is the Predicted Percentage Dissatisfied (PPD), which defines the percentage of thermally dissatisfied occupants. Table 4.1 outlines the OTS levels applied in the present use case for winter clothing. For instance, OTS level I specifies a narrower acceptable temperature range which spans 22.6 °C and 24 °C compared with OTS level II, which spans 21.5 °C and 25 °C.

[6] Day-ahead electricity prices are considered fixed, predefined price signals for the next 24 hours; they are not considered as forecast.

[7] The control models are not used within the control strategy.

Table 4.1: Two OTS levels used for defining membership functions based on standard EN-16798 and winter clothing. The parameters are from Frahm et al. (2023) calculated using the CBE Thermal Comfort Tool (Tartarini et al. 2020).

OTS	PMV	PPD	$T_{\mathrm{air,min}}$	$T_{\mathrm{air,max}}$
I	± 0.2	$< 6\%$	$22.6\,°\mathrm{C}$	$24\,°\mathrm{C}$
II	± 0.5	$< 10\%$	$21.5\,°\mathrm{C}$	$25\,°\mathrm{C}$

Design of fuzzy logic thermal building controllers

Both control algorithms are formulated with minimal information required, i.e. four inputs: (i) the electricity price signal $p_{\mathrm{buy},k}$ expressed in $\mathrm{EUR/kWh}$, (ii) the coefficient of performance of the heat pump COP$_k$, which is determined by the ambient temperature $T_{\mathrm{amb},k}$, (iii) the temperature error e_k, defined as the difference between the reference temperature $T_{\mathrm{air,ref},k}$ and the indoor air temperature $T_{\mathrm{air},k}$, and (iv) the change in indoor air temperature error, $\Delta e_k = e_k - e_{k-1}$. The operation of the heat pump transforms the electrical input power $P_{\mathrm{el},k}$ into the delivered heat flux $\dot{Q}_{\mathrm{h},k}$ defined for the time step k as:

$$\dot{Q}_{\mathrm{h},k} = \mathrm{COP}_k \cdot P_{\mathrm{el},k} \tag{4.1}$$

Figure 4.1 illustrates membership functions of both FLCs, where the μ presents the fuzzy membership value. Figure 4.1(a-b) illustrate the defined membership functions for the indoor air temperature error of the comfort-oriented e_{com} and economic-oriented e_{eco} algorithms. Figure 4.1c depicts the change in indoor air temperature error Δe. Figures 4.1(d-f) illustrate the defined COP membership functions based on ambient temperature T_{amb}, dynamic electricity price signals p_{buy}, and the control signal α, respectively. The two controllers differ in the design of the membership functions for the temperature error and in the composition of the rule base (see Figure 4.1(a-b) and Tables C.1 and C.2). The comfort-oriented controller is configured to prioritize occupant thermal comfort by assigning greater emphasis to the temperature error $e_{\mathrm{com},k}$ and its rate of change $\Delta e_{\mathrm{com},k}$. For the temperature error membership functions e_{com}, the zero-error membership function is strictly defined such that the peak is at $T_{\mathrm{air}} = T_{\mathrm{ref}}$. Furthermore, the zero-error membership function is designed to represent OTS level I, whereas the "small warm" and "small cold" membership functions are constructed to align with OTS level II. The OTS constraints are translated into the corresponding indoor air temperature error values. The midpoint of the temperature range of the zero membership function, i.e., the midpoint of OTS level I temperature range, is used as setpoint temperature $T_{\mathrm{ref}} = 23.3\,°\mathrm{C}$ for heating hours.

In contrast, in the economic-oriented controller, high electricity prices and low heat pump efficiency are more penalized. The temperature-error membership functions e_{eco} of the economic-oriented controller are derived from OTS levels I and II. In this design, the zero-error membership function has a trapezoidal shape with intentionally wider top base on the positive side, where $\mu_{\mathrm{e_{eco}}} = 1$, while the other end of the top base on the negative side is more restrictive. This structure provides stricter control once the indoor air temperature approaches T_{ref}. As a result, a positive value in the membership function leads the economic-oriented controller to intentionally allow lower temperatures in order to reduce operational costs (see Figure 4.1b).

The change-of-temperature error Δe membership functions are implemented using triangular shapes. The "zero" membership function spans the interval from -0.5 to 0.5 $^\circ\mathrm{C}$. In contrast, the widest, i.e. "faster warmer" and "faster colder", reach full activation ($\mu_{\Delta\mathrm{e}} = 1$) at the magnitude of $\pm 1\,^\circ\mathrm{C}$.

The COP is modeled as a function of ambient temperature T_{amb}. For the ground-source heat pump, the COP varies from 3.06 to 4.86 when the ambient temperature T_{amb} ranges from -7 $^\circ\mathrm{C}$ to 12 $^\circ\mathrm{C}$ (NIBE Systemtechnik GmbH). Based on this operating range, three membership functions "low", "average", and "optimal" are defined. Time-varying electricity prices are incorporated using external data obtained from aWATTar GmbH. The membership function "average" price is determined using the mean of 0.0796 $\mathrm{EUR/kWh}$ and median of 0.0842 $\mathrm{EUR/kWh}$ electricity prices over the evaluation period described in Section 4.1.2. Additionally, two further membership functions, "low" and "high", are constructed to capture variations in price levels. The output of the FLC controllers α_{com} and α_{eco} specify an incremental adjustment to the current control signal $P_{\mathrm{el},k}$. To allow fine-grained control, seven output membership functions are employed and presented in Figure 4.1f over the normalized output domain. The resulting incremental signal is subsequently scaled by 300 W, which prevents rapid changes in heat pump operation. The maximum electrical power of the heat pump is limited to 2 kW. The heat pump electricity in the time step k is defined as follows:

$$P_{\mathrm{el},k+1} = P_{\mathrm{el},k} + \alpha \cdot 300\,\mathrm{W}, \text{ for } \alpha \in \{\alpha_{\mathrm{eco}}, \alpha_{\mathrm{com}}\} \tag{4.2}$$

The fuzzy rule base designs, in which α_{com} and α_{eco} represent the fuzzy outputs of the comfort- and economic-oriented controllers, respectively, are provided in Appendix C in Tables C.1 and C.2. The underlying principles of these controllers differ: the comfort-oriented controller exhibits greater sensitivity to the indoor air temperature error e_{com} and its rate of change Δe_{com}, thereby improving thermal comfort for occupants. In contrast, the economic-oriented controller operates with a more flexible interpretation of the acceptable temperature range, as previously discussed in this section. This distinction becomes evident, for example, when comparing rule 1 of the comfort-oriented controller in Table C.1 with rules 45–51 of the economic-oriented controller

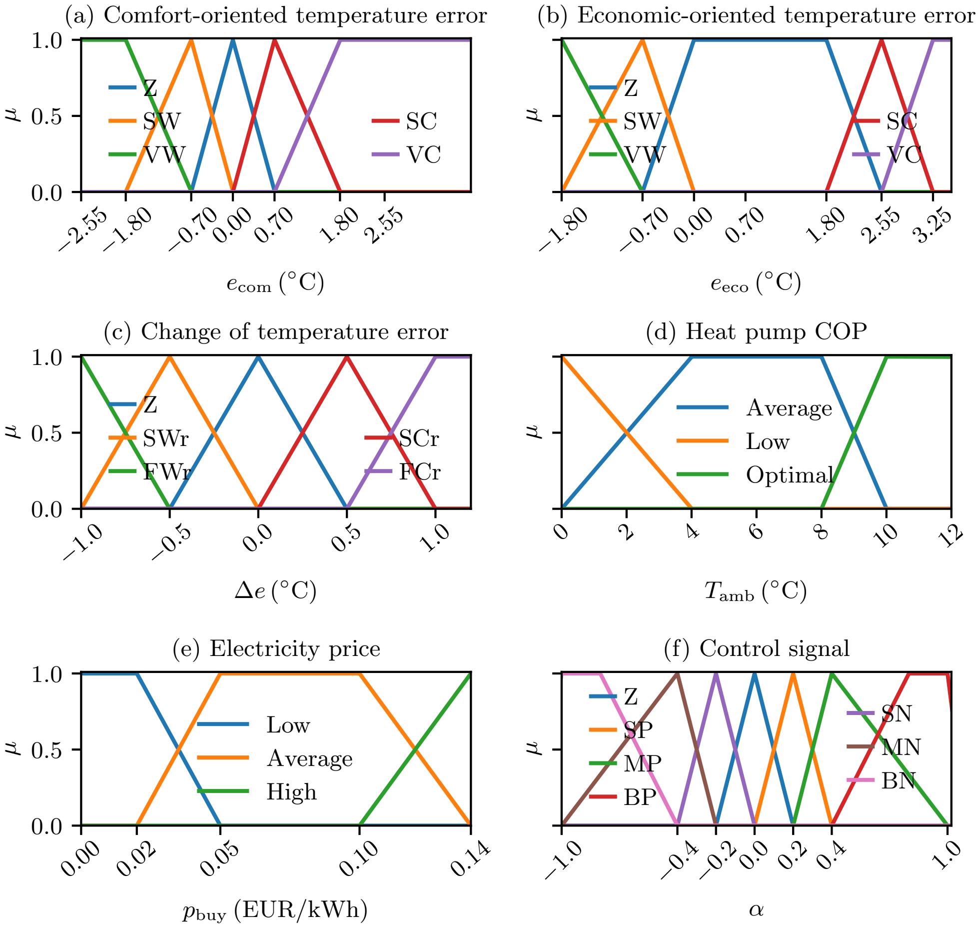

Figure 4.1: Membership functions for inputs and outputs of both comfort- and economic-oriented controllers. Abbreviations stand for: Z - "zero"; SW - "small warm"; VW - "very warm"; SC - "small cold"; VC - "very cold"; SWr - "slower warmer"; FWr - "faster warmer"; SCr - "slower colder"; FCr - "faster colder"; SP - "small positive"; MP - "medium positive"; BP - "big positive"; SN - "small negative"; MN - "medium negative"; BN - "big negative".

in the Table C.2. Both sets of rules address the operating condition in which the indoor air temperature error and its rate of change are in fuzzy set "zero", i.e., $e_k = 0$ and $\Delta e_k = 0$. In rule 1 of the comfort-oriented controller, the control action remains unchanged from the previous time step, indicated by $\alpha_{\mathrm{com},k} = \mathrm{Z}$, regardless of the external dynamic signals $p_{\mathrm{buy},k}$ and COP_k. Conversely, the economic-oriented controller determines, based on these external signals, whether the control action should remain unchanged ($\alpha_{\mathrm{eco},k} = \mathrm{Z}$) or be reduced by a small decrement ($\alpha_{\mathrm{eco},k} = \mathrm{SN}$) or a medium decrement ($\alpha_{\mathrm{eco},k} = \mathrm{MN}$).

Baseline controller

A commonly used hysteresis controller (Martinčević et al. 2016) is implemented as a benchmark model. For a quantitative comparison, the hysteresis constraints are selected to correspond to the constraints of OTS level II (see Table 4.1). Accordingly, the controller activates at an indoor air temperature $T_{\mathrm{air,min}}$ of $21.5\,^\circ\mathrm{C}$ using the maximum heating power $P_{\mathrm{el,max}}$ and deactivates once the indoor air temperature $T_{\mathrm{air,max}}$ reaches $25\,^\circ\mathrm{C}$. During unoccupied periods, i.e., outside regular working hours, the hysteresis controller remains switched off.

Information required by the controllers

Table 4.2 gives an overview of the data required by different controllers. Hysteresis, as expected needs the lowest amount of the information, only indoor air temperature $T_{\mathrm{air},k}$ and temperature constraints $T_{\mathrm{air,min},k}$ and $T_{\mathrm{air,max},k}$ for the time step k. The comfort- and economic-oriented controllers additionally require ambient temperature $T_{\mathrm{amb},k}$ to obtain the COP$_k$ values and electricity prices $p_{\mathrm{buy},k}$. All controllers are forecast-free, and none require day-ahead electricity prices.

Table 4.2: Information required by the controllers.

Controller	$T_{\mathrm{air},k}$	$T_{\mathrm{air,min/max},k}$	$T_{\mathrm{amb},k}$	$p_{\mathrm{buy},k}$	Forecasts	Day-ahead prices
Hysteresis	✓	✓	—	—	—	—
Comfort-oriented	✓	✓	✓	✓	—	—
Economic-oriented	✓	✓	✓	✓	—	—

Gray-box thermal building model

The proposed control strategies are evaluated using a single-zone gray-box thermal building model. The 2R2C model structure is used from Madsen and Holst (1995). The model comprises two states: the indoor air temperature T_{air}, which is also the system output, and the temperature of the thermal building mass T_{m}, as described by Equations (4.3)–(4.4). The gray-box thermal building model requires three input signals: the ambient temperature T_{amb}, global solar radiation $\dot{q}_{\mathrm{sol}}$, and the heat flow supplied by a heat pump $\dot{Q}_{\mathrm{h}}$.

$$C_{\mathrm{air}} \frac{\mathrm{d}T_{\mathrm{air}}}{\mathrm{d}t} = \frac{T_{\mathrm{m}} - T_{\mathrm{air}}}{R_{\mathrm{air}}} + \frac{T_{\mathrm{amb}} - T_{\mathrm{air}}}{R_{\mathrm{amb}}} + \dot{Q}_{\mathrm{h}} + g_{\mathrm{sol}} \dot{q}_{\mathrm{sol}} \tag{4.3}$$

$$C_{\mathrm{m}} \frac{\mathrm{d}T_{\mathrm{m}}}{\mathrm{d}t} = \frac{T_{\mathrm{air}} - T_{\mathrm{m}}}{R_{\mathrm{air}}} \tag{4.4}$$

The thermal resistances of heat transfer between the ambient air and the indoor air, and between the thermal building mass and the indoor air, are denoted as R_{amb} and R_{air}, respectively. The thermal capacitances of the indoor air and the thermal building mass are represented by C_{air} and C_{m}, respectively. Additional details regarding the utilized gray-box thermal building model can be found in (Madsen and Holst 1995, Frahm et al. 2022b).

4.1.2 Case study

The identification and validation of the RC thermal building model are performed using measurement data from an LLEC building at the KIT (Wiegel et al. 2022). According to Gray and Schmidt (2016), a three-week identification interval ensures a relatively low forecasting error. Consequently, a dataset with a $2\,\mathrm{min}$ resolution spanning from December 20, 2021, to January 10, 2022, is selected for parameter identification, while the validation interval covers one week from January 10, 2022, to January 16, 2022. In this period, the heating experiment was conducted, in which the LLEC building was heated in different phases to generate high-quality data for gray-box model identification. The RMSEs of the indoor air temperature predictions for the identification and validation phases amount to $0.25\,^{\circ}\mathrm{C}$ and $0.34\,^{\circ}\mathrm{C}$, respectively. Although the thermal building model is identified and validated using data from the winter period of December 2021 and January 2022, the control strategy assessment is based on data from November 22, 2023, to January 21, 2024. Given comparable weather conditions, it is assumed that the building exhibits similar thermal behavior across the two winter datasets, as argued by Broholt et al. (2022). Since no data on OB patterns are available, the reference indoor air temperature $T_{\mathrm{air,ref}}$ is specified according to the usual working hours. Thus, reference indoor air temperature $T_{\mathrm{air,ref}}$ is $23.3\,^{\circ}\mathrm{C}$ between 8:00 AM and 6:00 PM, including a two-hour preheating period, whereas a value of $18\,^{\circ}\mathrm{C}$ is assumed outside these hours, reflecting the heat pump being switched off.

4.1.3 Results and discussion

The controlled indoor air temperature, electricity demand, dynamic electricity prices, and the dynamic heat pump's COP across two representative one-week intervals for all three controllers are illustrated in Figures 4.2 and 4.3. These intervals are selected to illustrate the worst- and best-case conditions over the entire assessment period. Specifically, Figure 4.2 depicts a week characterized by relatively high electricity prices and low-to-average COP of the heat pump. On the other hand, Figure 4.3 presents a week with low electricity prices during which the heat pump operates in a highly efficient mode. The gray regions shown in the indoor air temperature subplots (4.2a and 4.3a) indicate the designated working hours during which heating is provided. In the subplots depicting dynamic electricity prices p_{buy} and COP, the red segments correspond to intervals characterized by relatively high prices and low COP values, which are specified by the FLCs' input membership functions. Accordingly, the yellow zones denote medium electricity prices and moderate COP values, whereas the green zones highlight periods of low electricity prices accompanied by high, optimal COP performance.

To assess the performance of the proposed control strategies over a two-month period, three statistical indicators are employed: (i) mean daily discomfort, based on Equation (2.15), (ii) total electricity costs, as defined in Equation (2.17) and (iii) total electricity consumption in kWh. To get the mean daily discomfort, Equation (2.15) is averaged as follows:

$$d_{\text{day}} = \frac{1}{\text{NoD}} \cdot d \tag{4.5}$$

where NoD denotes the number of days. The discomfort is evaluated only for the period when the building is occupied and using the OTS level II temperature constraints, i.e., $T_{\text{air,min}} = 21.5\,^{\circ}\mathrm{C}$ and $T_{\text{air,max}} = 25\,^{\circ}\mathrm{C}$.

Thermal discomfort

With the proposed control strategies, daily mean thermal discomfort values of $0.13\,\mathrm{Kh}$ and $5.18\,\mathrm{Kh}$ are achieved with the comfort- and economic-oriented controllers, respectively, whereas the hysteresis controller does not exhibit any daily mean discomfort. The hysteresis controller exhibits the lowest daily mean discomfort, as it is designed to activate when the indoor air temperature T_{air} reaches the lower constraint $T_{\text{air,min}}$ and to deactivate once the upper constraint $T_{\text{air,max}}$ is attained. Since these limits also define the thermal discomfort metric, minimal violations naturally occur.

In contrast, the comfort-oriented controller tracks the reference temperature T_{ref} during the heating phase. After reaching the reference temperature T_{ref}, it maintains the temperature within a narrow band until the end of the day, as illustrated in Figures 4.2a and 4.3a. The hysteresis controller, however, continues heating until $T_{\text{air,max}}$, leading to greater intra-day temperature

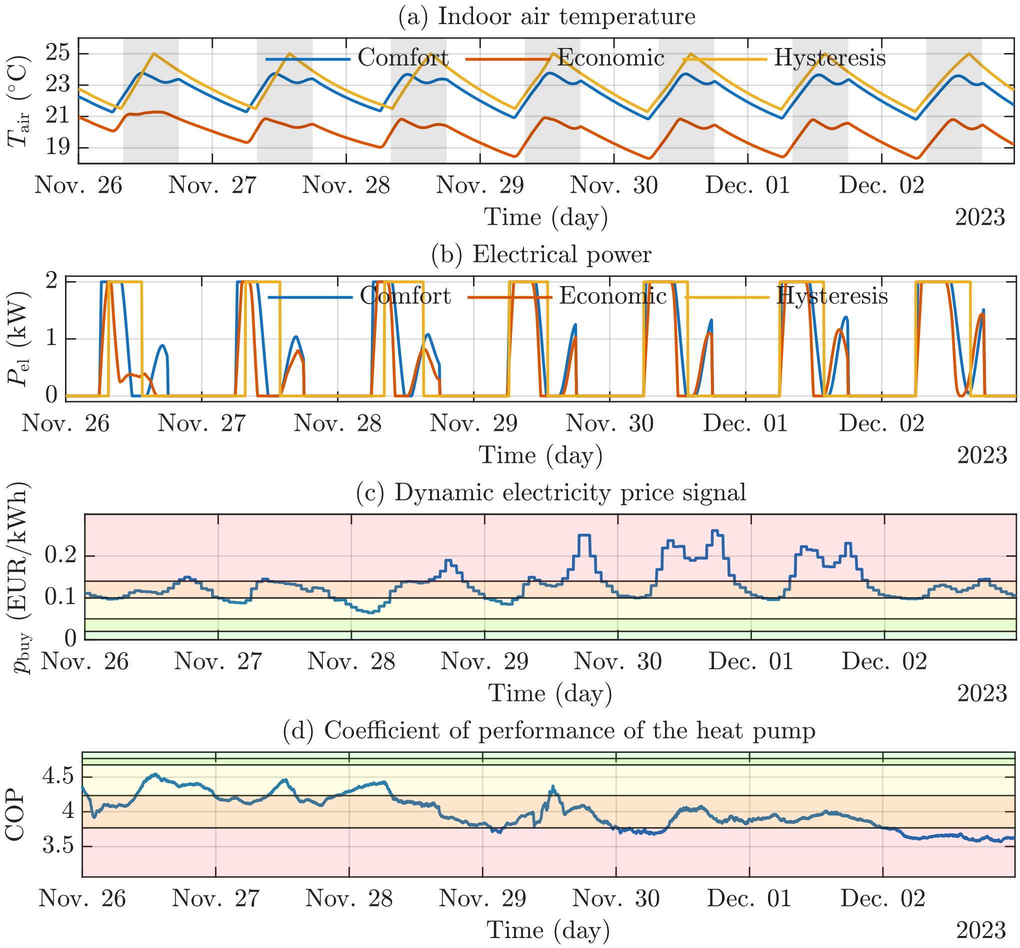

Figure 4.2: The controller comparison of indoor air temperature (T_{air}) and heat pump power (P_{el}) under high electricity prices (p_{buy}) and average-to-high heat pump COP, during the period from November to December 2023. The figure is derived from Kovačević et al. (2024b).

variation. These temperature fluctuations can also be characterized as uncomfortable for the occupants.

The economic-oriented controller incorporates a permissible deviation range around the reference indoor air temperature, as shown in Figure 4.1b. It penalizes high electricity prices and low heat pump COP, thereby allowing the indoor air temperature to drop. This mechanism results in the highest thermal discomfort. As depicted in Figure 4.2a, the indoor air temperature drops to approximately 21 °C during periods of elevated electricity prices. Conversely, when electricity

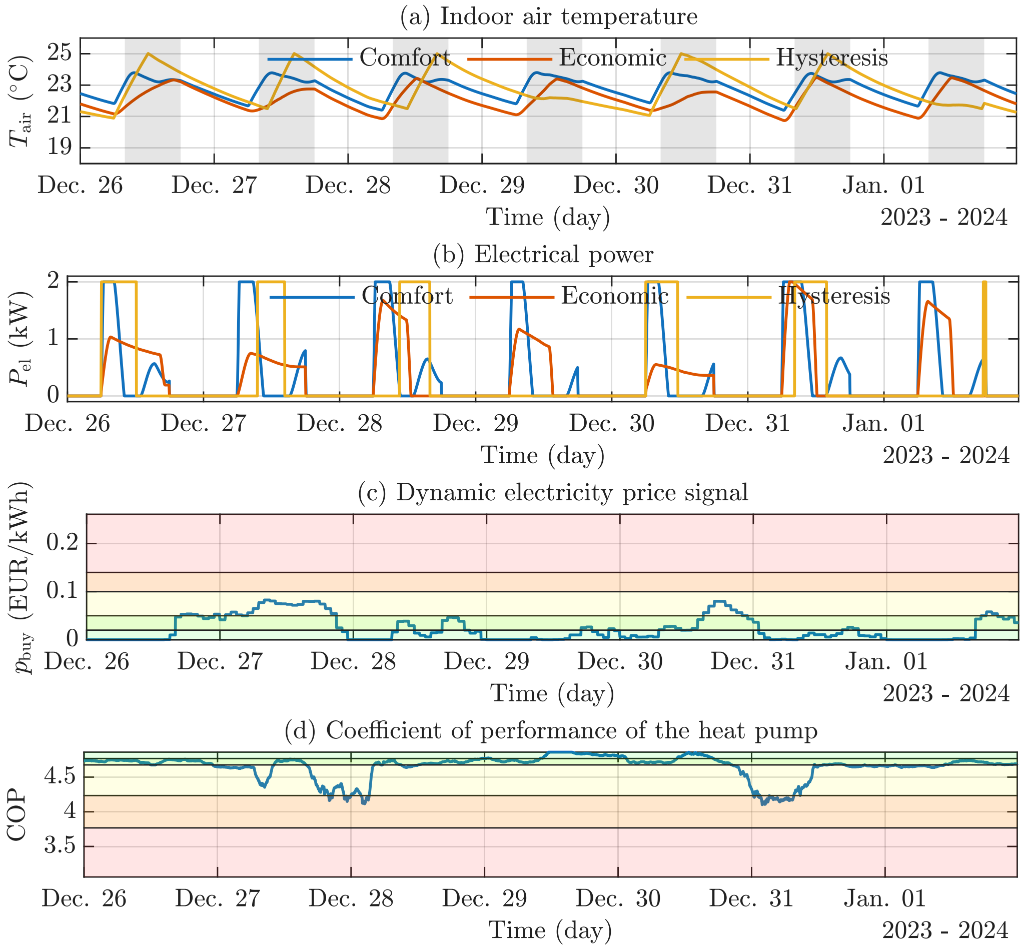

Figure 4.3: The controller comparison of indoor air temperature (T_{air}) and heat pump power (P_{el}) under low electricity prices (p_{buy}) and low-to-average heat pump COP, during the period from December 2023 to January 2024. The figure is derived from Kovačević et al. (2024b).

prices are low, and the heat pump operates efficiently, the economic-oriented controller maintains a higher indoor air temperature T_{air} level, as shown in Figure 4.3.

Electricity costs and consumption

Table 4.3 presents the total electricity costs in EUR and the electrical energy consumption in kWh for the evaluation interval from November 22, 2023, to January 21, 2024. The economic-oriented controller yields the lowest electricity costs and energy used, amounting to 58.21 EUR and 633.20 kWh, respectively. This outcome is expected, as the economic-oriented strategy is formulated to prioritize electricity price signals and heat pump efficiency over occupants' comfort, as shown in Figures 4.2 and 4.3.

In contrast, the comfort-oriented and hysteresis controllers result in similar electricity costs of 68.62 EUR and 71.34 EUR, respectively. Although the comfort-oriented controller accounts for electricity prices and the heat pump's COP, its primary objective is to maintain occupant comfort. Consequently, it results in slightly lower energy consumption of 722.51 kWh compared with the hysteresis controller energy consumption of 744.20 kWh.

The electrical power consumption over a representative worst-case and best-case week is illustrated in Figures 4.2b and 4.3b. From Figure 4.2b, it becomes evident that during periods of high electricity prices, the economic-oriented controller operates less frequently at maximum power than the comfort-oriented controller. The reduction in consumption is still not significant, as the heat pump peaks at 2 kW in on-peak hours, which can be unfavorable for the grid, while the occupants' thermal discomfort remains significant. On the contrary, in the best-case scenario (see Figure 4.3b), the economic-oriented controller has the feature of peak shedding, meaning it does not necessarily peak at the maximum heat pump power. However, this feature should be further implemented for worst-case scenarios, as these represent the unfavorable state of the grid, where buildings can contribute by reducing consumption. The comfort-oriented controller continues to operate the heat pump at its maximum electrical power in the best-case scenario, constrained by its stricter indoor air temperature requirements.

Table 4.3: Energy consumption and electricity costs of all three controllers.

Controller	Consumption (kWh)	Costs (EUR)
Hysteresis	744.20	71.34
Comfort-oriented	722.51	68.62
Economic-oriented	633.20	58.21

Summary

Regarding thermal comfort, the comfort-oriented controller demonstrates the best performance. Although its discomfort value is marginally higher than that of the hysteresis, it maintains predominantly stable indoor air temperatures throughout the day, whereas the hysteresis controller exhibits pronounced temperature fluctuations.

Although the economic-oriented controller prioritizes reducing building energy demand by jointly considering the heat pump's operational efficiency and time-varying electricity prices, this approach substantially compromises occupants' thermal comfort, which is treated as a secondary objective. Peak shedding is observable during periods with low electricity prices and average-to-optimal heat pump efficiency. In contrast, under unfavorable conditions, characterized by elevated electricity prices and low-to-average heat pump operation, the economic-oriented controller is unable to suppress power peaks, even though the indoor temperature remains considerably lower than that achieved by the comfort-oriented and hysteresis controllers.

Table 4.4 provides an overview of the controllers' performance and the information required for their operation. When considering the statistical indicators, the economic-oriented controller yields the most favorable results for energy consumption and operational costs, while the comfort-oriented controller achieves the highest level of indoor thermal comfort. None of the controllers relies on forecasting models, predefined profiles, or day-ahead electricity price information, highlighting the simplicity of the implemented strategies. However, neither of the FLC-based controllers is capable of shifting or reducing the peak load during on-peak periods under unfavorable grid conditions (see Figure 4.2). Incorporating additional information, such as predefined future electricity prices or constraints on future indoor air temperature, could enable load shifting without violating occupants' thermal comfort. The development of an improved FLC strategy is presented in the subsequent section, followed by its evaluation in a real-world experimental setting.

Table 4.4: Summary of the controllers' performance and features. A poor performance is indicated by 🔴, average performance by 🟡 and good performance by 🟢.

Controller	Consumption	Costs	Comfort	Information required
Hysteresis	🔴	🔴	🟡	🟢
Comfort-oriented	🟡	🟡	🟢	🟡
Economic-oriented	🟢	🟢	🔴	🟡

4.2 Experiment: Real-world evaluation of the fuzzy logic control for demand response in buildings

This section proposes FLC for a real-world setup to exploit the building's thermal mass for demand response. FLC is benchmarked against Baseline (BL), whose control actions are based on the heating curve. FLC considers the room-individual occupant schedules as allowable temperature constraints and uses dynamic day-ahead heating price signals to encourage thermal load shifting of the building.[8]

4.2.1 Methodology

The experimental study is conducted in two identical buildings that are part of the LLEC infrastructure at the KIT (Wiegel et al. 2022). Each building has a usable floor area of approximately $100\,\mathrm{m}^2$ and comprises five rooms, a corridor, a bathroom, and a kitchen (see Figure 3.4). The utility rooms in both buildings are excluded from the analysis, as they serve exclusively for hydraulic configuration.

The heating configuration employed in this study comprises an underfloor heating system supplied via the district heating network. Both buildings are supplied with the same temperature from the district heating network. The supply water is then mixed with underfloor heating return water to achieve the required supply setpoint temperature $T_{\mathrm{s,ref}}$. The resulting mixture is circulated by a pump, which delivers the supply water at temperature T_{s} to each room. Every room is equipped with a control valve that regulates the mass flow rate of the incoming supply water.

Two supervisory control strategies are implemented, namely an FLC and a BL controller. Both approaches operate at a higher hierarchical level and define the setpoints for (i) the indoor air temperature in each room $T_{\mathrm{air,ref},j}$, and (ii) the supply water temperature of the underfloor heating system $T_{\mathrm{s,ref}}$. These setpoint values are then forwarded to the underlying local control loops, which consist of (i) an on/off controller for regulating the indoor air temperature in each room and (ii) a Proportional–Integral (PI) controller for adjusting the supply water temperature.

The exchange of information between the supervisory control layer and the building infrastructure is depicted in Figure 4.4. The supervisory controllers differ in the level of information required for operation. They rely on external data sources, which include: (i) the ambient temperature T_{amb} obtained from the German Weather Service (Deutscher Wetterdienst - DWD), required by each supervisory controller, and (ii) the heat price signal p_{buy}, which is utilized exclusively by the FLC. The setpoints defined by the supervisory control algorithms, indoor air temperature $T_{\mathrm{air,ref}}$ and supply water temperature $T_{\mathrm{s,ref}}$, are transmitted to local Programmable Logic Controllers (PLCs) via the MQTT protocol. By actuating the respective room and mixing valves, the local controllers ensure that the setpoint temperatures are met. In the feedback loop, indoor air temperatures T_{air}

[8] This section is based on a research paper I co-authored (Langner and Kovačević et al. (2025)). Note that my contribution is the development of the FLC strategy for room-individual thermal building control. The remainder is the contribution from my colleague Felix Langner.

and the supply temperature T_s measurements are monitored by PLCs and stored in InfluxDB via MQTT.

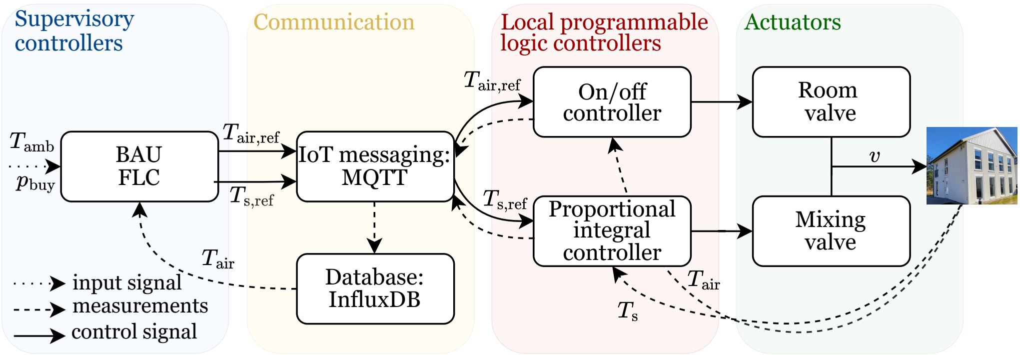

Figure 4.4: Information flow in the buildings. The figure is adapted from Langner and Kovačević et al. (2025).

Two sets are introduced in the present study: $\mathcal{J} = \{\mathrm{R}_1, \mathrm{R}_2, \mathrm{R}_3\,, \mathrm{R}_4\,, \mathrm{R}_5\,, \mathrm{C}, \mathrm{K}, \mathrm{B}\}$ enumerates all considered rooms, corridor, kitchen, and bathroom, respectively (see Figure 3.4). The rooms are labeled as follows: R_1 - dining room, R_2 - living room, R_3 and R_4 children's room, and R_5 bedroom, whereas C refers to the corridor, K to the kitchen, and B to the bathroom. Second, $\mathcal{K} = \{1, 2, \ldots, N\}$ represents the sequence of natural numbers up to N, corresponding to the number of discrete time steps. For this case study, the sampling time of $t_\mathrm{s} = 15\,\mathrm{min}$ is chosen, and a horizon for predefined future heat price signals is $24\,\mathrm{h}$.

Baseline

BL is employed to reduce energy demand and determine the supply temperature via a heating curve that depends solely on the ambient temperature T_amb:

$$T_{\mathrm{s,ref,HC},k} = \begin{cases} 45\,^\circ\mathrm{C}, & \text{for } T_{\mathrm{amb},k} \leq -10\,^\circ\mathrm{C}, \\ 20\,^\circ\mathrm{C}, & \text{for } T_{\mathrm{amb},k} \geq 20\,^\circ\mathrm{C}, \\ \left(20 + \dfrac{20 \cdot 25}{30}\right) - \dfrac{25}{30}\,T_{\mathrm{amb},k}, & \text{otherwise.} \end{cases} \tag{4.6}$$

The controller maintains the indoor air temperature of each room j at the lower temperature constraint $T_{\mathrm{air,min},j,k}$ so that energy use is minimized.

Fuzzy logic control

The FLC determines the control action for each room j by evaluating four distinct input variables:

(i) The error term e_j, defined as the difference between the lower temperature constraint and the indoor air temperature of room j:

$$e_{j,k} = T_{\mathrm{air,min},j,k} - T_{\mathrm{air},j,k} \tag{4.7}$$

(ii) The temporal temperature variation $\Delta T_{\mathrm{air},j}$ observed within a two subsequent time steps, which reflects potential disturbances, e.g., a sudden decrease in indoor air temperature may indicate that windows have been opened:

$$\Delta T_{\mathrm{air},j,k} = T_{\mathrm{air},j,k} - T_{\mathrm{air},j,k-1} \tag{4.8}$$

(iii) The change in the lower temperature constraint for the subsequent six hours is denoted as Δo_j:

$$\Delta o_{j,k} = T_{\mathrm{min},j,k} - T_{N/4,j,k} \tag{4.9}$$

$$T_{N/4,j,k} = \begin{cases} T_{\mathrm{air,min},j,k+w}, & \text{if } \exists w : T_{\mathrm{air,min},j,k+w-1} \neq T_{\mathrm{air,min},j,k+w} \\ & \text{for } w \in \{1, 2 ... N/4\}, \\ T_{\mathrm{air,min},j,k+N/4}, & \text{otherwise.} \end{cases} \tag{4.10}$$

Incorporating predefined occupant schedules enables the controller to initiate preheating when future occupancy is expected and, conversely, to reduce heating demand when the room is expected to remain unoccupied. The six-hour window, equivalent to 24 sampling steps (i.e., $N/4$) at a 15 min interval, is motivated by the high thermal inertia of underfloor heating systems. This time span gives the controller enough time to preheat the room.

(iv) The ECDF of the day-ahead heat price, $\hat{F}(p_{\mathrm{buy}})$, indicating whether the current price level is low or high relative to future prices (see Section 2.3.3).

FLC specifies the room indoor air temperature setpoints $T_{\mathrm{air,ref},j}$ and the supply water temperature setpoint of the underfloor heating system $T_{\mathrm{s,ref}}$. Whereas the room indoor air temperature setpoints are directly inferred, the supply temperature setpoint, Equation (4.11), is obtained by determining a temperature deviation α_{s} relative to the heating curve (see Equation (4.6)).

$$T_{\mathrm{s,ref},k+1} = T_{\mathrm{s,HC},k} + \beta \cdot \max_j \left(\alpha_{\mathrm{s},j,k+1}\right), \ \beta = 10 \tag{4.11}$$

Using the input data, the supervisory controller computes, for each room individually, both the subsequent indoor air temperature setpoint and the normalized supply water temperature increment $\alpha_{\mathrm{s},j,k+1}$. To guarantee that every room is provided with an adequate thermal supply, the maximal defined increment is chosen, scaled by the factor β, and subsequently added to the reference supply temperature $T_{\mathrm{s,HC},k}$.

Figure 4.5(a-d) display the membership functions of input variables, whereas the membership functions of control signals are shown in Figure 4.5(e-f). The variation in the lower temperature constraint, depicted in Figure 4.5c, is represented by three triangular membership functions, since the permissible values of the lower constraint $T_{\mathrm{air,min}}$ can be either 18 °C or 21 °C, i.e., a deviation of ± 3 K (see Figure 4.9).

In the subplot in Figure 4.5e, the function T_{off} is omitted from the plot; however, it is applied whenever the room is unoccupied, corresponding to $T_{\mathrm{air,min}} = 18\,^{\circ}\mathrm{C}$. This membership function is defined as a triangular shape ranging from 17.5 °C to 18.5 °C with its peak at 18 °C, and it does not intersect with any other membership functions. The membership functions associated with the supply temperature control signal $\alpha_{\mathrm{s},j}$, presented in the Figure 4.5f, are restricted to positive output values. This is because the BL supply water temperature is increased exclusively when required to ensure the achievement of the higher indoor air temperature setpoints $T_{\mathrm{air,ref},j}$.

Since the lower temperature constraint $T_{\mathrm{air,min}}$ varies between 18 °C and 21 °C (see Figure 4.9), two distinct rule sets are established accordingly. An overview of the corresponding rules for both configurations is given in Appendix C.2 in Tables C.3 and C.4. For example, when a substantial heating demand coincides with a low heat price, the FLC intensifies the heating action. This situation emerges when the temperature error $e_{j,k}$ of room j at time step k is classified as "zero", the indoor air temperature change $\Delta T_{\mathrm{air},j,k}$ indicates a "colder", and no change of the lower temperature constraint is expected within the subsequent six hours (i.e., $\Delta o_{j,k}$ is "zero"). If, in addition, the ECDF of the heat price $\hat{F}\left(p_{\mathrm{buy}}\right)_k$ falls into the "low" category, the controller assigns the next-step temperature setpoint $T_{\mathrm{air,ref},j,k+1}$ to T_{BP}, thereby triggering a significant heating response. Simultaneously, the supply temperature increment $\alpha_{\mathrm{s},j,k+1}$ is a "big positive" (see rule 4 in Table C.3). In contrast, when the ECDF of price signal $\hat{F}\left(p_{\mathrm{buy}}\right)_k$ indicates "high" while the remaining inputs are unchanged, the controller suppresses strong heating. In this case, the room setpoint temperature $T_{\mathrm{air,ref},j,k+1}$ is reduced to the lower temperature constraint, and only a minor increase in the supply temperature $\alpha_{\mathrm{s},j,k+1}$ ("small positive") is applied to prevent the temperature from dropping (see rule 6 in Table C.3).

Figure 4.6 illustrates the control signals $T_{\mathrm{air,ref},j,k+1}$ and $\alpha_{\mathrm{s},j,k+1}$ for the scenario in which $T_{\mathrm{min},j} = 21\,^{\circ}\mathrm{C}$, $e_{j,k}$ and $\Delta o_{j,k}$ are "zero", while all remaining inputs are varying. Along the axis associated with variations in $\Delta T_{\mathrm{air},j,k}$, a pronounced gradient becomes evident, indicating that both control actions rise sharply once a negative disturbance (such as a window opening) is

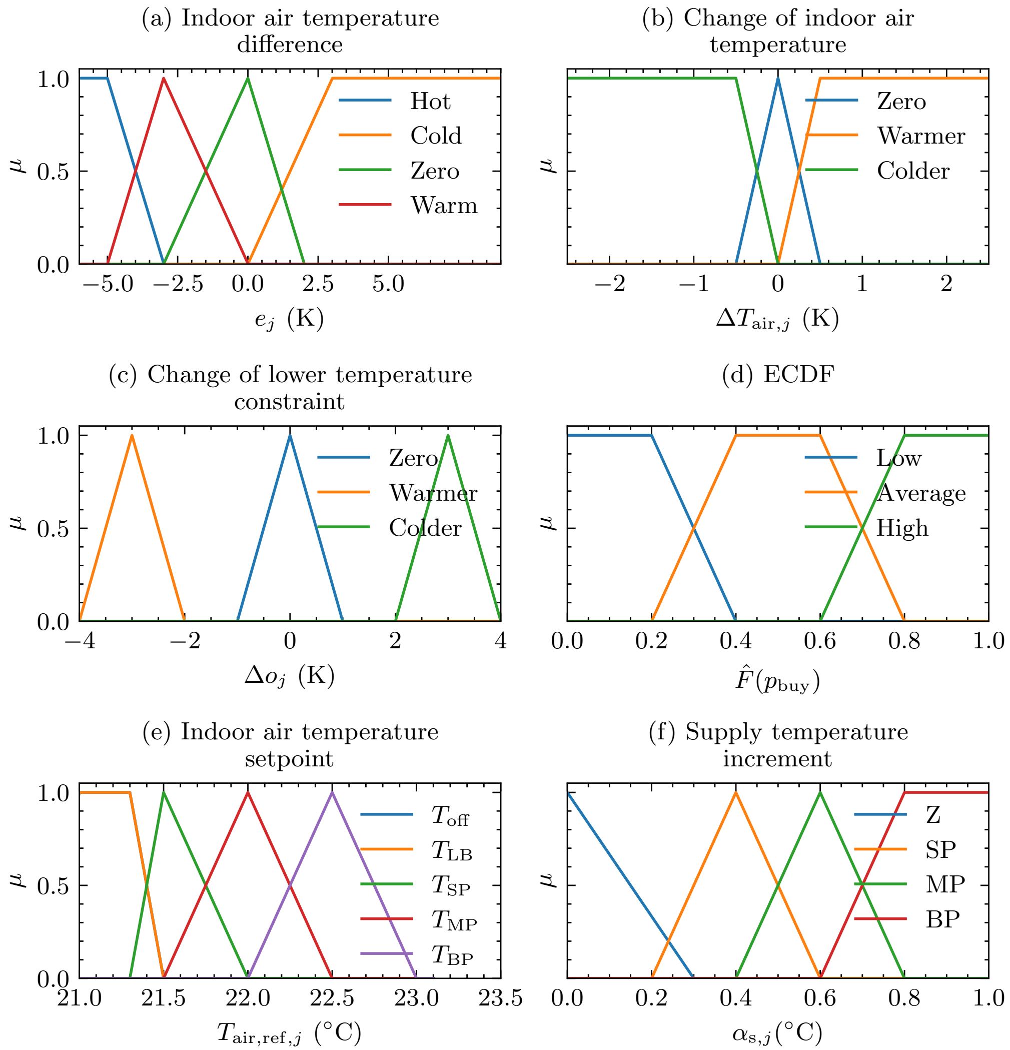

Figure 4.5: Defined membership functions for all inputs and outputs of FLC. The figure is adopted from Langner and Kovačević et al. (2025).

detected. Moreover, when $\hat{F}(p_{\mathrm{buy}})_k$ attains large values, the two control signals are maintained at low levels in order to reduce operational costs.

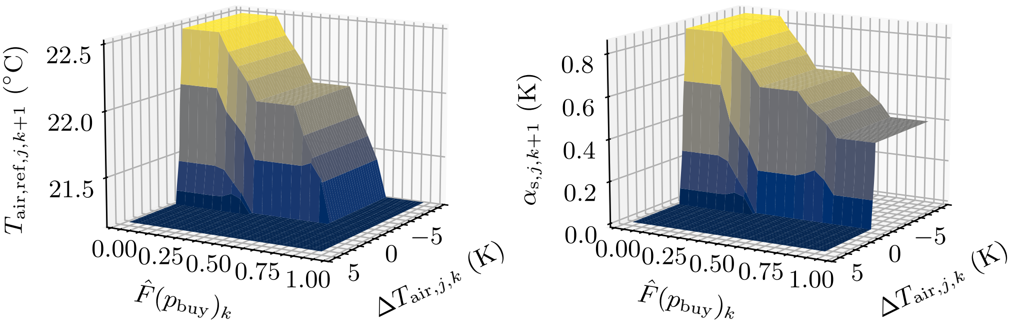

Figure 4.6: The FLC input-output mapping when the ECDF of the heat price $\hat{F}\left(p_{\mathrm{buy}}\right)_k$ and the change of the room temperature $\Delta T_{\mathrm{air},j,k}$ vary. The case of $T_{\mathrm{min},j,k} = 21\,^{\circ}\mathrm{C}$ is depicted. The remaining two input signals are kept constant $e_{j,k} = 0$ K and $\Delta o_{\mathrm{j,k}} = 0$ K. The figure is derived from Langner and Kovačević et al. (2025).

4.2.2 Case study

Four experiments with different setups for cost minimization are carried out between December 2024 and February 2025, as illustrated in Figure 4.7. The experiments differ in the dynamic price signals, temperature constraints, and disturbances. Experiment 1, performed from December 22 to 28, employs variable price signals while maintaining fixed temperature constraints. In Experiment 2, conducted between December 30 and January 5, the constant temperature constraints are replaced by variable constraints. Experiment 3, performed from February 14 to 16, combines variable and constant heating price signals with variable temperature constraints. The final experiment 4, undertaken from January 10 to 12, incorporates disturbances in addition to the setup from experiment 3.

With the exception of experiment 4, all remaining experiments were conducted with the interior doors fully closed. The west-facing roller shutters of the west building and the east-facing roller shutters of the east building were kept closed throughout the experiments to reduce the influence of solar radiation. Moreover, all electrical devices were turned off throughout the entire experimental period.

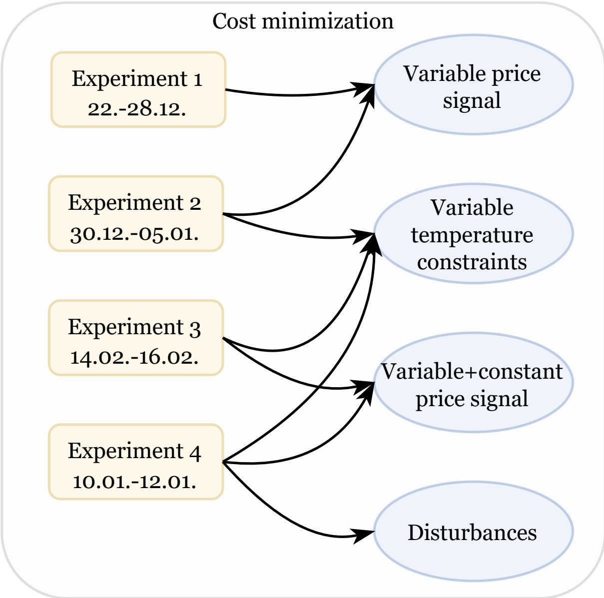

Figure 4.7: Experimental schedule for operational cost minimization with four different setups.

Heating price signals

As the basis for deriving heating price signals, day-ahead electricity prices are employed. Two distinct pricing schemes are examined: (i) the "variable" price, which is solely determined by the spot market price and therefore exhibits pronounced intra-day fluctuations, and (ii) the "variable + constant" price, which incorporates, in addition to the time-dependent spot market prices, a fixed component representing charges and taxes (Smart Energy Tariff | tado°). Figure 4.8 shows the seven-day heating price signal used throughout the experiments.

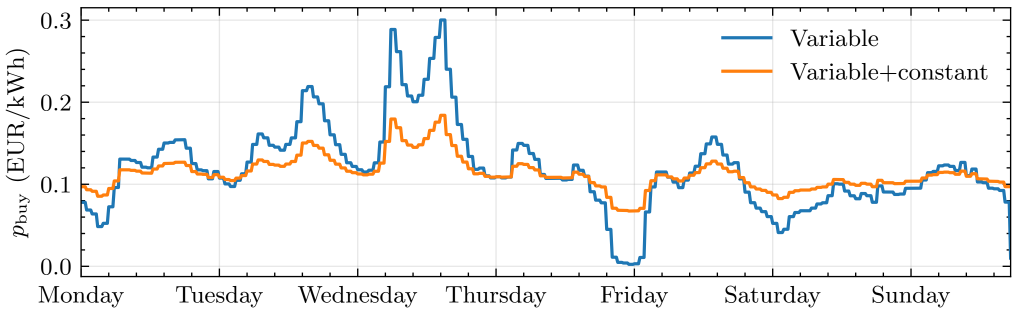

Figure 4.8: Dynamic heat price signals. The figure is derived from Langner and Kovačević et al. (2025).

Table 4.5 links each experimental setup to the corresponding daily heat price signals illustrated in Figure 4.8. For example, experiment 4, which spans three days, incorporates heating price signals from Thursday through Saturday to represent both weekday and weekend conditions.

Table 4.5: Mapping of the heating price signals to experiments.

Heat price signal	Experiment 1	Experiment 2	Experiment 3	Experiment 4
Variable	Mon.-Sun.	Mon.-Sun.	—	—
Variable + constant	—	—	Thu.-Sat.	Thu.-Sat.

Temperature constraints and disturbances

Two types of temperature constraints are applied across the experimental setups. The constant temperature constraints, defined as $T_{\mathrm{air,min}} = 21\,°\mathrm{C}$ and $T_{\mathrm{air,max}} = 24\,°\mathrm{C}$, are implemented only in experiment 1. All subsequent experiments employ variable temperature constraints. This configuration is adjusted individually for each room and depends on the respective occupancy schedules provided in Ueno and Meier (2020). An overview of the variable temperature constraints for all rooms is presented in Figure 4.9.

Experiment 4 incorporates disturbances into the setup. Identical disturbance profiles are applied to both buildings, as they are fully automated. These disturbances arise from the opening of interior doors and windows, as well as from the actuation of the roller shutters. The disturbance schedule for all rooms is illustrated in Figure 4.10. For example, in room R_1, representing the dining room, the interior door D and the roller shutters R remain open for the entire day, whereas the window W is opened twice, once in the morning and once in the evening, for a duration of $10\,\mathrm{min}$ on each occasion.

Evaluation metrics

Three statistical indicators are used for the evaluation of the control strategies: (i) daily averaged thermal discomfort d_{day} (ii) energy costs σ_{buy} and (iii) daily flexibility factor ϕ_{day}.

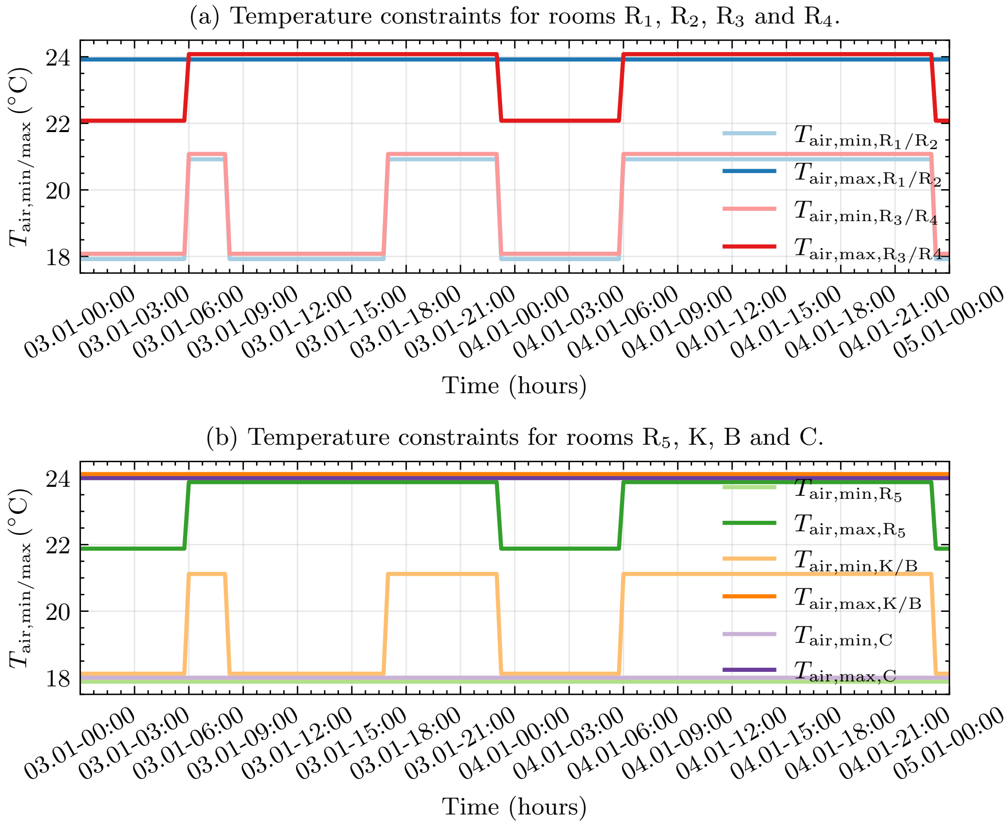

Figure 4.9: The room-specific variable temperature constraints.

The thermal discomfort is evaluated as a room-specific, daily averaged indicator and thus Equation (2.15) is adjusted to the following form:

$$d_{\mathrm{day}} = \frac{1}{J \cdot \mathrm{NoD}} \cdot t_{\mathrm{s}} \cdot \sum_{j} \sum_{k} d_{j,k} \tag{4.12}$$

where NoD represents the number of simulation days and J is the total number of rooms. The $d_{j,k}$ is calculated as described by Equation (2.16) for each room j.

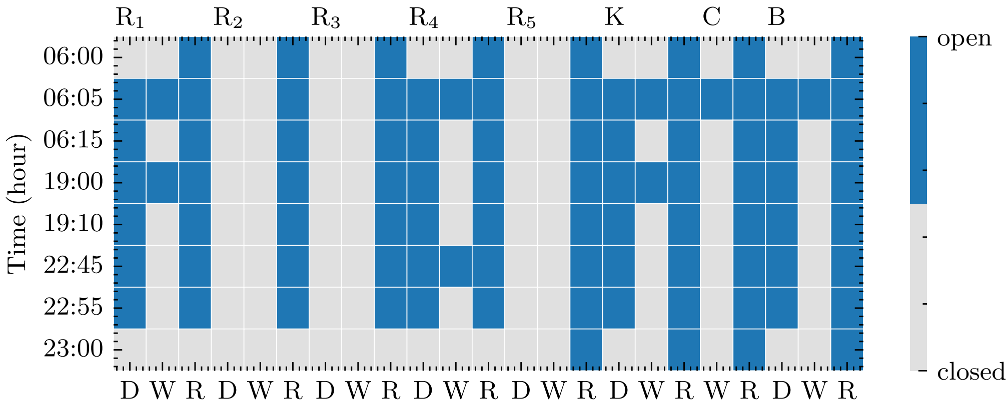

Figure 4.10: Disturbances schedule. Abbreviations: D - door; W - window; R - roller shutters.

In accordance with Equation (2.17), the formulation is adapted to express the total cost as the sum of room-specific costs, each based on the heating power and price signals:

$$\sigma_{\text{buy}} = t_s \cdot \sum_k \sum_j p_{\text{buy},k} \cdot \dot{Q}_{\text{h},j,k} \tag{4.13}$$

The flexibility factor ϕ_{day} (Le Dréau and Heiselberg 2016) is calculated as follows:

$$\phi_{\text{day}} = \frac{\sum_{k \in \underline{\mathcal{K}}} \dot{Q}_{\text{h},k} - \sum_{k \in \overline{\mathcal{K}}} \dot{Q}_{\text{h},k}}{\sum_{k \in \underline{\mathcal{K}}} \dot{Q}_{\text{h},k} + \sum_{k \in \overline{\mathcal{K}}} \dot{Q}_{\text{h},k}} \tag{4.14}$$

where $\dot{Q}_{\text{h},k}$ represents the heat flow of the entire building and $\underline{\mathcal{K}}$ and $\overline{\mathcal{K}}$ correspond to the time step subsets where the heating prices are in lower and upper quartiles of the corresponding day, respectively. The flexibility factor ϕ_{day} ranges from -1 to 1. A value approaching 1 indicates that the heating system predominantly operates during low-price periods, reflecting high flexibility. A value near zero signifies balanced operation across both high- and low-price intervals, indicating low flexibility. A flexibility factor approaching -1 indicates increased heating use when prices are high.

4.2.3 Results and discussion

The energy consumption comparison of the two identical buildings used in the present experiment is reported in Langner and Kovačević et al. (2025), and it indicates that the discrepancy in total building demand remains below 1% during periods of minimal wind.[9]

Figure 4.11 illustrates the indoor air temperature for each room, the aggregate heat demand, and the corresponding heating price signal for both buildings during experiment 1. BL controller maintains the indoor air temperature of each room at the lower limit $T_{\mathrm{air,min}}$ to ensure minimal energy usage. Conversely, the FLC modulates thermal demand by preheating indoor air in response to the heating price signal, thereby shifting consumption to periods with lower heating costs (e.g., between 00:00 and 06:00). Moreover, the FLC strategy typically preheats the rooms only up to 22 °C, despite the upper temperature limit $T_{\mathrm{air,max}}$ being set to 24 °C. Rapid, large changes in temperature can be unfavorable for occupants. Therefore, load shifts are constrained to smaller changes in indoor air temperature, thereby reducing load flexibility.

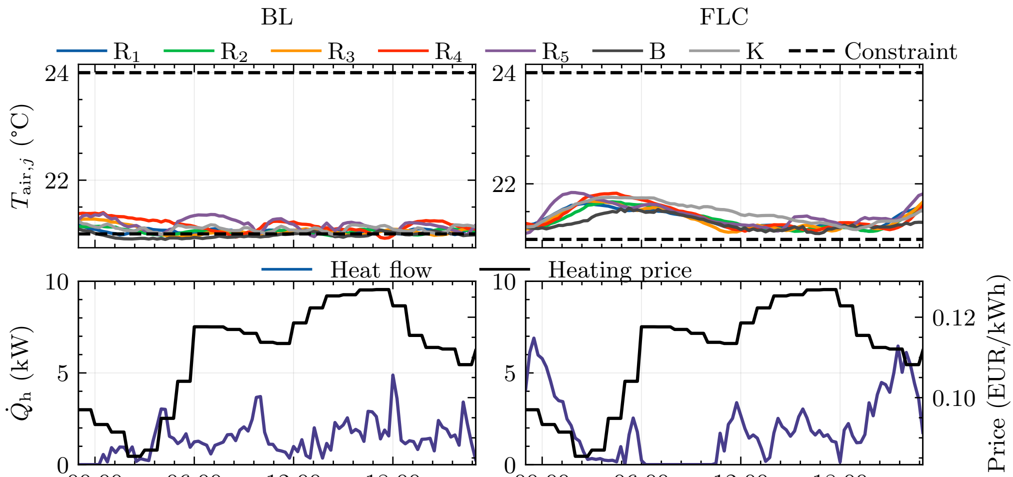

Figure 4.11: One day evaluation during experiment 1 depicting indoor air temperature in rooms, total building heat flow, and heating price signal. Figure is adapted from Langner and Kovačević et al. (2025).

Figures 4.12 and 4.13 illustrate the indoor air temperature, heat flow, and heating prices for rooms 2 and 4, respectively, under different temperature constraint conditions. The FLC receives information about the future 6 h occupancy schedule (e.g., temperature constraints) and thus preheats the rooms only 6 h in advance. It also does not usually preheat more than 22 °C to avoid

9 The measurements from buildings collected during these experiments are published in Tajalli-Ardekani et al. (2025).

rapid changes in temperature, as mentioned earlier, and to avoid violating the upper temperature constraint $T_{\mathrm{air,max}}$ (see Figure 4.13). However, this also limits the potential for cost reduction of FLC. On January 1, two high peaks in heating costs occur, during which FLC avoids heating by shifting the load and preheating the rooms. Moreover, on January 2, FLC keeps room temperatures mostly constant at the lower temperature constraint. This happens as heating price discrepancies throughout the day are minimal, and in combination with corresponding temperature constraints, preheating would lead to economically unprofitable load shifting.

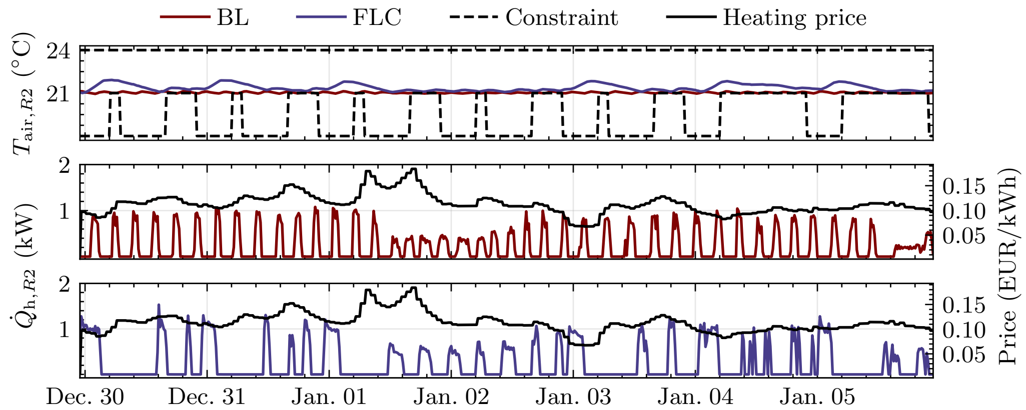

Figure 4.12: Indoor air temperature and heat flow for room R_2 with heating price signals during experiment 2. Figure is adapted from Langner and Kovačević et al. (2025).

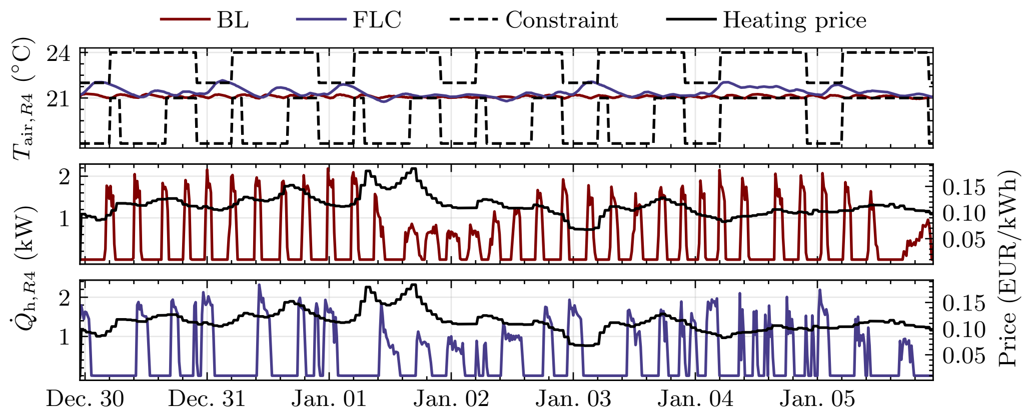

Figure 4.13: Indoor air temperature and heat flow for room R_4 with heating price signals during experiment 2. Figure is adapted from Langner and Kovačević et al. (2025).

Experiment 4 illustrates disturbances in the building by actuating the roller shutters, windows, and interior doors. Figure 4.14 illustrates the influence of window opening in room R_1 and kitchen K. Both controllers increase the heating flux to restore a comfortable indoor air temperature in the rooms. Additionally, FLC also increases the supply water temperature to reduce the impact of the disturbances faster. Bathroom B does not have an open window; its temperature is indirectly affected by the opening of windows in other rooms. Rooms 2 and 5 are shown as the rooms where the disturbance does not occur. In addition, room 5 is plotted separately as it has different temperature constraints.

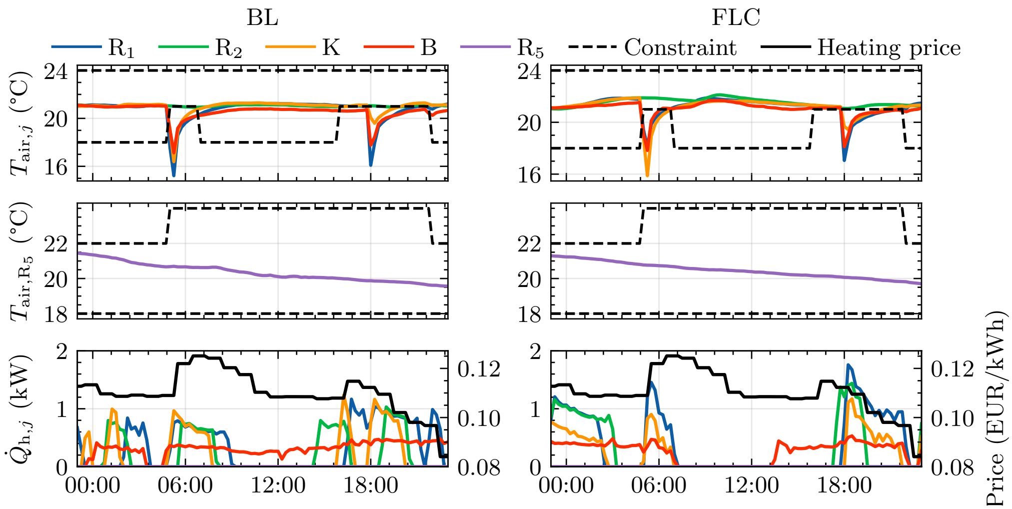

Figure 4.14: Indoor air temperature of the rooms, corresponding heat flows, and heating price on January 10. 2025, during experiment 4. Figure is adapted from Langner and Kovačević et al. (2025).

Operational costs

The heating costs for four experiments are shown in Figure 4.15. Experiments 1–2 and 3–4 are displayed separately, as their durations differ and they rely on distinct heating price signals (see Figure 4.7). The BL results in the following operational costs: 37.17 EUR for experiment 1, 36.95 EUR for experiment 2, 13.65 EUR for experiment 3 and 16.38 EUR for experiment 4. In comparison, the FLC yields following cost reduction: 7.4% in experiment 1, 8.6% in experiment 2, 5.2% in experiment 3 and 4.4% in experiment 4. The slightly higher reduction in experiment 2 arises from the varying temperature constraints, which allow lower indoor air temperatures ($T_{\mathrm{air,min}} = 18\,^{\circ}\mathrm{C}$) during the "sleeping" and "away" periods (see Figures 4.12 and 4.13).

The heating price signal used in experiments 3 and 4 exhibits lower discrepancies compared to the signal applied in experiments 1 and 2 (see Figure 4.8 and Table 4.5), thereby reducing the cost reduction potential. Moreover, in experiment 4, compared with experiment 3, the costs and heat demand increase for both controllers due to disturbances. Achieving more substantial cost reduction would require FLC to shift larger thermal loads, thereby necessitating preheating to higher indoor temperatures. Furthermore, the variability in the lower temperature constraint (e.g., $T_{\mathrm{air,min}} = 18\,°\mathrm{C}$) could be exploited more extensively, allowing the indoor temperature during unoccupied periods to be reduced further. However, rapid temperature fluctuations during occupied periods should be avoided, as they may compromise occupant comfort according to standard ISO 7730 (2025).

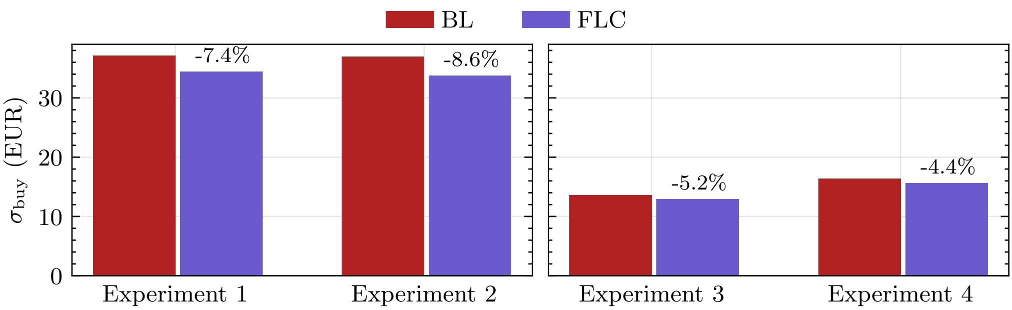

Figure 4.15: Heating costs and reduction for each experiment. Experiments employing identical price signals are configured within subplots. Figure is adapted from Langner and Kovačević et al. (2025).

Building flexibility

The daily flexibility factor ϕ_{day} is presented in Figure 4.16. In all four experiments, the median flexibility factor of the BL is near zero. This indicates that the BL heats the building almost equally during high- and low-heating-price periods. This happens because the BL does not utilize information about the heating price signal. FLC shifts the median of the flexibility factor upper, indicating more heating during the low heating price periods than during the high heating price periods. Among different experiments, the following flexibility factors are achieved: 0.2 for FLC and -0.02 for BL in experiment 1, 0.27 for FLC and -0.04 for BL in experiment 2, 0.09 for FLC and 0 for BL in experiment 3 and -0.02 for FLC and -0.1 for BL in experiment 4.

The slightly higher flexibility factor in experiment 2 compared to experiment 1 is followed by a looser lower temperature constraint $T_{\mathrm{air,min}}$, as already discussed earlier. The flexibility factor during the third day of experiment 3 exhibits the worst performance as the heating price signal is almost constant with maximal variation of $3\,\mathrm{ct}$ (see Figures 4.8 and C.1). In experiment 4, disturbances, such as window openings, force the controller to heat during peak hours, thereby reducing the flexibility factor.

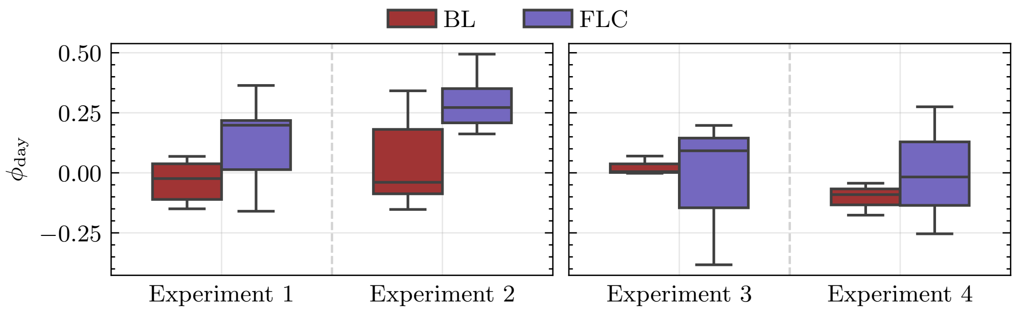

Figure 4.16: Daily flexibility factor ϕ_{day} box-plots for each experiment. Experiments employing identical price signals are configured within subplots. Figure is adapted from Langner and Kovačević et al. (2025).

Thermal discomfort

Thermal discomfort is presented for all experiments in Figure 4.17 and calculated as the daily room-average temperature constraint violation. From the first three experiments, it can be concluded that FLC does not experience thermal discomfort. In experiment 4, FLC manages faster to mitigate the impact of the disturbances than BL. Here, the thermal discomfort of the FLC is 31.4% lower than that of BL.

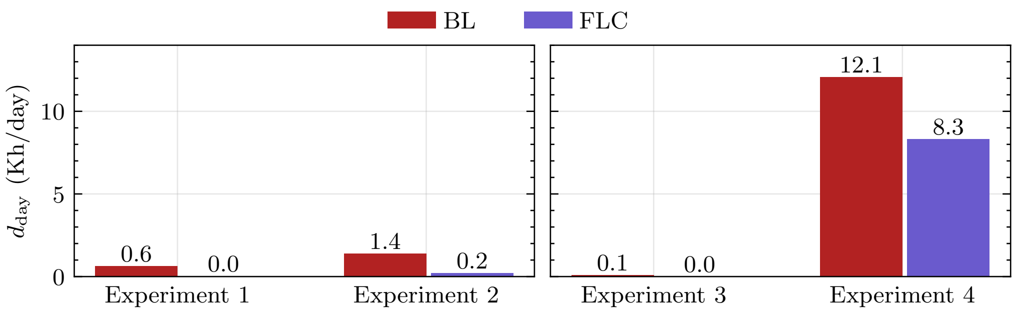

Figure 4.17: Daily room-average thermal discomfort d_{day} for all experiments. Experiments employing identical price signals are configured within subplots. Figure is adapted from Langner and Kovačević et al. (2025).

The histograms of the supply water temperature T_{s} of both controllers are presented in Figure 4.18. The BL determines the supply temperature according to the heating curve (see Equation (4.6)).

In contrast, the FLC shifts the histogram toward higher temperatures, as it relies on the same heating curve but modifies it through the correction factor α_s. This adjustment also facilitates load shifting during off-peak grid periods.

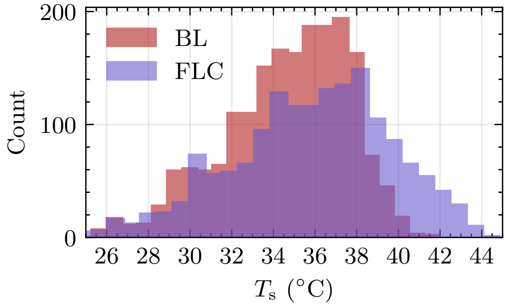

Figure 4.18: Supply water temperature histograms throughout all experiments. The figure is adapted from Langner and Kovačević et al. (2025).

4.3 Contributions

This section addresses **RQ3** and thereby closes the corresponding **research gap 3**, by evaluating the FLC strategy for demand response programs. The first part of this chapter (Section 4.1) examines and contrasts two forecast- and model-free FLC approaches for thermal building control. Both the comfort- and the economic-oriented driven FLCs retain simplicity. However, neither strategy can achieve substantial load shifting or shedding under unfavorable grid conditions. Consequently, additional information must be incorporated into the control strategy. Integrating day-ahead price signals together with occupants' schedules, expressed through time-dependent temperature constraints, can enable the controller to shift demand by preheating the building when the price signal is inexpensive.

In the real-world experiment evaluated in Section 4.2, the FLC is further developed by integrating the aforementioned information, which enhances the exploitation of load-shifting potential during operation. The FLC is designed such that the upper temperature constraint of 24 °C is not reached. Nevertheless, greater flexibility can be achieved when more energy demand is shifted to off-peak periods. Such behavior, however, may influence occupants, as larger temperature variations can reduce thermal comfort. Potential for extension can be investigating the optimal indoor air temperature ranges within the FLC strategy that allow the controller to fully utilize its flexibility without compromising comfort.

5 Fuzzy logic energy management system

Publications supporting the chapter content

- Jovana Kovačević, et al. ComEMS4Build: Comfort-Oriented Energy Management System for Residential Buildings using Hydrogen for Seasonal Storage. Preprint, 2025b. doi: 10.48550/arXiv.2511.04293.

The widespread integration of intermittent RES, such as PV and residential wind turbines, into building energy systems necessitates storage solutions to ensure flexibility across multiple time scales. BESS fulfills this role by storing renewable energy and providing short- to medium-term flexibility. Despite conventional BESS advantages in supporting RES integration, there are notable environmental challenges associated with manufacturing, raw material extraction, and end-of-life disposal (Simpa et al. 2024). Electric vehicles can also be categorized as a flexible resource, providing energy to buildings when needed and charging when building energy conditions are favorable (Berkes and Keshav 2024). Furthermore, hydrogen-powered vehicles offer flexibility but remain in a research area that requires significant technological advancements (Agert et al. 2023). On the other hand, stationary hydrogen storage enables seasonal energy shifting by storing surplus summer electricity in a high-energy-density, low-leakage form that can be utilized during periods of high demand and low renewable generation. Hydrogen storage and BESS complement each other, providing energy flexibility throughout the year.

To manage these complex, versatile energy technologies, an advanced EMS is necessary to enhance the efficiency and performance of distributed energy resources in residential applications (Mariano-Hernández et al. 2021). This chapter contributes to fulfilling the **research gap 4** and answers **RQ4** and **RQ5** by developing the EMS for residential building setup with distributed resources[10] where heat pump and fuel cell operate collaboratively. As the EMS has a crucial impact on the performance of distributed energy resources, three strategies with different information

[10] Note that under distributed energy resources following energy resources are considered throughout the present chapter: PV, BESS, hydrogen storage, DHW storage, heat pump, fuel cell and building thermal mass.

requirements have been developed and compared. A model- and forecast-free strategy, Comfort-Oriented Energy Management System for Residential Buildings (ComEMS4Build), is introduced and benchmarked against MPC and RBC, as described in detail in the following section.

5.1 Method: Comfort-oriented energy management using hydrogen seasonal storage

The fuel cell and the heat pump were initially viewed as rival technologies (Dodds et al. 2015, Knosala et al. 2022). In recent years, however, they have been recognized as complementary. Andrade et al. (2025) show that coupling a fuel cell with a heat pump under European climate conditions can reduce the required fuel cell capacity by at least 40%, thereby lowering the investment costs, while the heat pump can provide up to 20% energy savings. To the best of the author's knowledge, a detailed assessment of operational flexibility, in which grid dependence is reduced by hydrogen utilization, and the building's thermal mass is used as an additional storage medium, has not yet been reported. Thus, the scientific contribution, a novel EMS for coupled fuel cell and heat pump operation, is presented within a residential building case study to demonstrate its feasibility. The building is further enhanced with the PV, BESS, DHW storage and hydrogen storage. The EMS is developed as a forecast- and model-free controller that accounts for occupants' thermal comfort while simultaneously utilizing thermal building mass as an additional flexibility term. The proposed EMS - ComEMS4Build is benchmarked against a cost-optimal MPC, which requires forecasting models and profiles, and an RBC, which is designed with minimal input requirements.

5.1.1 Methodology

Figure 5.1 shows the residential building configuration[11], in which all components and the corresponding electricity, heating, and hydrogen flows are depicted. The HESS is composed of short-term BESS storage and long-term hydrogen storage. Dynamic electricity prices are used to characterize the state of the electricity grid, while a PV system is integrated as an additional energy source. Alongside the DHW storage, the thermal building mass is employed as supplementary thermal energy storage, both highlighted in Figure 5.1 with a red background. Three control strategies are examined:

(i) ComEMS4Build is developed as forecast- and model-free FLC strategy,

[11] A typical four-person household is considered in the present case study.

(ii) RBC is derived from the ComEMS4Build rule set and constructed as the minimalistic baseline, requiring only essential inputs for operating the building's distributed energy resources,

(iii) MPC is employed as an optimal reference controller that operates under ideal forecasts and requires the most inputs.

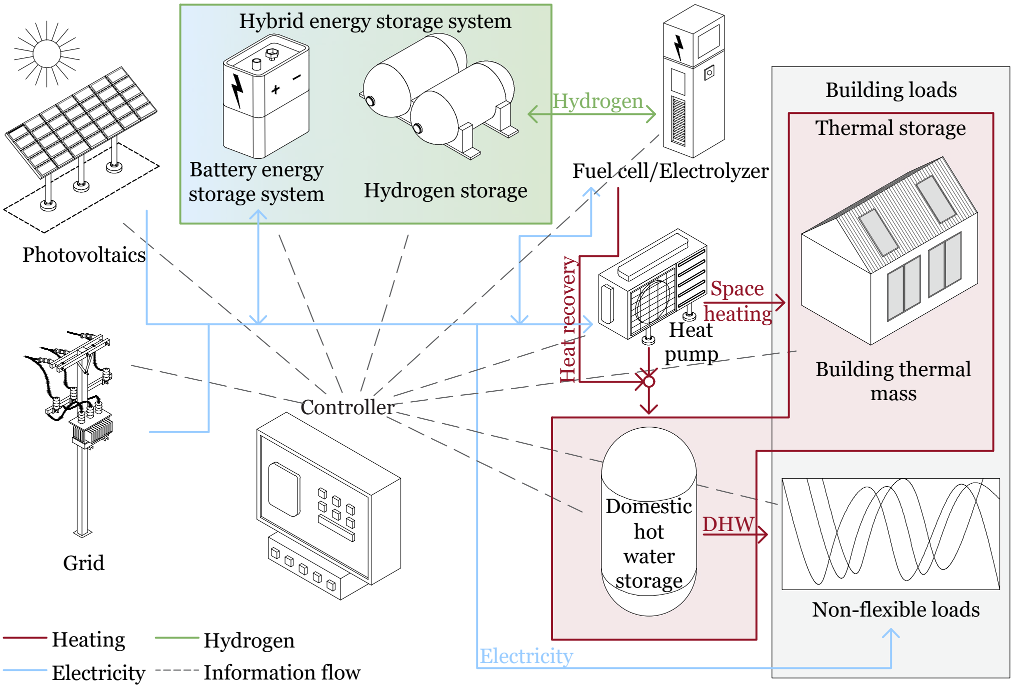

Figure 5.1: The residential building with PV, HESS, DHW storage, fuel cell, heat pump, and thermal building mass as an additional thermal energy storage. Figure is adapted from Kovačević et al. (2025b).

Models

In this subsection, the models used for the present study are described. First, the PV power generation and BESS models are presented. Thereafter, the hydrogen system, which includes the fuel cell and hydrogen storage, is defined. This is followed by a description of the heat pump and the DHW storage system. Finally, a gray-box thermal building model, used as the control model in MPC and as a physical representation, is presented.

Photovoltaics (PV): PV generation defined in the literature (Al Essa 2019) is expressed by Equation (5.1). It is determined by the number of modules n_{module}, the module area a_{module} in m^2, and the incident solar radiation G_k in the time step k, given in W/m^2. The value G_k is obtained from the global radiation $\dot{q}_{\text{sol}}$, the diffuse radiation, and the module's tilted angle (Hazyuk et al. 2012).

The nominal operating cell temperature NOCT, the ambient air temperature T_{amb}, and the standard test condition temperature T_{STC} are all expressed in $^\circ\text{C}$. The term $(\text{NOCT} - 20^\circ\text{C})/800\text{W}/\text{m}^2$ is used to represent the overall heat-loss coefficient in $^\circ\text{Cm}^2/\text{W}$ (Rouhani et al. 2013):

$$\begin{aligned} P_{\text{PV},k} =& n_{\text{module}} \cdot a_{\text{module}} \cdot G_k \cdot \eta_{\text{STC}} \cdot \eta_{\text{L\&T}} \\ & \cdot \Big[1 - \big(\eta_T \cdot (T_{\text{amb},k} + \frac{\text{NOCT} - 20^\circ\text{C}}{800\text{W}/\text{m}^2} \cdot G_k - T_{\text{STC}})\big)\Big] \end{aligned} \tag{5.1}$$

where η_{STC} is the electrical efficiency at standard test conditions, $\eta_{\text{L\&T}}$ represents the combined inverter and maximum power point tracking efficiency losses, and η_T is the temperature coefficient in $1/^\circ\text{C}$.

Battery Energy Storage System (BESS): The SOC_k at time step k, as formulated in the literature (Javadi et al. 2020), is computed from the former state SOC_{k-1}, the charging and discharging powers $P_{\text{ch},k}$ and $P_{\text{d},k}$, the corresponding efficiencies η_{ch} and η_{d}, and the battery's maximum capacity $E_{\text{BESS,max}}$:

$$\text{SOC}_k = \text{SOC}_{k-1} + (\eta_{\text{ch}} \cdot P_{\text{ch},k} \cdot t_{\text{s}} - \frac{P_{\text{d},k}}{\eta_{\text{d}}} \cdot t_{\text{s}})/E_{\text{BESS,max}} \tag{5.2}$$

where the sample time t_{s} is expressed in hours. The effect of BESS self-discharge has not been taken into account. The BESS is subject to Equations (5.3) and (5.6). The binary variables $s_{\text{ch},k}$ and $s_{\text{d},k}$, defined in Equations (5.5) and (5.6), are introduced to ensure that simultaneous charging and discharging do not occur, meaning the condition $s_{\text{ch},k} = 1$ and $s_{\text{d},k} = 1$ is prohibited:

$$\text{SOC}_{\min} \leq \text{SOC}_k \leq \ \text{SOC}_{\max} \tag{5.3}$$

$$s_{c,k} \cdot P_{c,\min} \leq P_{c,k} \leq \ s_{c,k} \cdot P_{c,\max} \tag{5.4}$$

$$s_{c,k} \in \{0,1\}; \ \forall c \in \{\text{ch}, \text{d}\} \tag{5.5}$$

$$s_{\text{ch},k} + s_{\text{d},k} \in \{0,1\} \tag{5.6}$$

Hydrogen system: It is assumed that the green hydrogen is produced during summer using the electrolyzer when surplus RES generation is available and is subsequently stored in the hydrogen storage. When needed, the stored hydrogen is reconverted into electricity by the fuel cell. Heat is also released as a byproduct of the fuel cell. It is recovered and utilized to meet the DHW demand, enabling cogeneration.

For the modeling of hydrogen system approaches commonly adopted in the literature are followed (Firtina-Ertis et al. 2020, Cau et al. 2014, Lacko et al. 2014). The molar hydrogen flow consumed by the fuel cell $\dot{n}_{\text{FC}}$ (measured in mol/s) is expressed as a function of the fuel cell's electrical output $P_{\text{el,FC}}$ [12], as presented in Equation (5.7). Faraday's law derives the electrical efficiency $\eta_{\text{el,FC},k}$ from the hydrogen Lower Heating Value (LHV) and molar flow $\dot{n}_{\text{FC},k}$ for time step k, as defined in Equation (5.8):

$$\dot{n}_{\text{FC}} = f(P_{\text{el,FC}}) \tag{5.7}$$

$$\eta_{\text{el,FC},k} = \frac{P_{\text{el,FC},k}}{\dot{n}_{\text{FC},k} \cdot \text{LHV}} \tag{5.8}$$

Similar to the BESS, the Level of Hydrogen (LOH) is formulated as the percentage of hydrogen energy content in storage, as shown in Equation (5.9). LOH_k is presented as the difference between the previous state LOH_{k-1} and hydrogen used in the current time step k:

$$\text{LOH}_k = \text{LOH}_{k-1} - \dot{n}_{\text{FC},k} \cdot \text{LHV} \cdot \frac{t_{\text{s}}}{E_{\text{H}_2,\text{max}}} \tag{5.9}$$

where the ideal gas law is applied as the hydrogen can be stored at lower pressures, e.g., 13–30 bar (Cau et al. 2014, Acar et al. 2023). Moreover, according to Acar et al. (2023), these pressure levels have an additional advantage. No additional energy is required for compression to higher pressures, since the electrolyzer produces hydrogen at the aforementioned low pressure levels. The hydrogen storage is constrained by the LOH_{min} and LOH_{max}, while the fuel cell is constrained by minimal and maximal power $P_{\text{el,FC,min}}$ and $P_{\text{el,FC,max}}$:

$$\text{LOH}_{\text{min}} \leq \text{LOH}_k \leq \text{LOH}_{\text{max}} \tag{5.10}$$

$$P_{\text{el,FC,min}} \cdot s_{\text{FC},k} \leq P_{\text{el,FC},k} \leq \zeta \cdot P_{\text{el,FC,max}} \cdot s_{\text{FC},k} \tag{5.11}$$

where the factor ζ is a restriction factor related to fuel cell degradation.

[12] The relation molar flow - fuel cell electrical output is usually provided by manufacturer.

The heat generated by the fuel cell, as presented in Ou et al. (2021), is calculated based on hydrogen molar flow $\dot{n}_{\mathrm{FC},k}$, thermal efficiency of the fuel cell $\eta_{\mathrm{th,FC}}$, and LHV:

$$\dot{Q}_{\mathrm{hr,FC},k} = \dot{n}_{\mathrm{FC},k} \cdot \eta_{\mathrm{th,FC},k} \cdot \mathrm{LHV} \tag{5.12}$$

$$\eta_{\mathrm{th,FC},k} = \eta_{\mathrm{sys,FC}} - \eta_{\mathrm{el,FC},k} \tag{5.13}$$

where the thermal efficiency of the fuel cell $\eta_{\mathrm{th,FC}}$ is estimated based on the total and electrical fuel cell efficiencies, $\eta_{\mathrm{sys,FC}}$ and $\eta_{\mathrm{el,FC},k}$, respectively.

Heat pump: The heat pump, represented with Equations (5.14) and (5.15), transforms the electricity $P_{\mathrm{el,HP}}$ into the heat flux $\dot{Q}_{\mathrm{h}}$. The COP is subject to ambient air temperature T_{amb} and supply water temperature T_{s}. The supply water temperature is $55\,^{\circ}\mathrm{C}$ when it comes to space heating and $45\,^{\circ}\mathrm{C}$ when heating DHW:

$$\dot{Q}_{\mathrm{h},k} = \mathrm{COP}_k \cdot P_{\mathrm{el,HP},k}, \quad \mathrm{COP}_k = \mathrm{COP}(T_{\mathrm{amb},k}, T_{\mathrm{s},k}) \tag{5.14}$$

$$P_{\mathrm{el,HP},k} = \eta_{\mathrm{HP},k} \cdot P_{\mathrm{el,HP,max},k}, \quad \eta_{\mathrm{HP}} \in \{0, [0.2, 1]\} \tag{5.15}$$

where η_{HP} represents the modulation factor of heat pump electrical power usage, and it is controlled by the EMS. Moreover, the modulation factor η_{HP} can be either 0 (e.g., the heat pump is turned off) or between 0.2 and 1. The EMS decides whether the heat pump works in space heating $\dot{Q}_{\mathrm{h,SH},k}$ or DHW $\dot{Q}_{\mathrm{h,DHW},k}$ mode. The binary variables s_{SH} and s_{DHW} are constrained so that the heat pump can be used in only one mode at a time:

$$s_{\mathrm{SH},k}\,,\, s_{\mathrm{DHW},k} \in \{0, 1\} \tag{5.16}$$

$$s_{\mathrm{SH},k} + s_{\mathrm{DHW},k} \in \{0, 1\} \tag{5.17}$$

$$\dot{Q}_{\mathrm{h,SH},k} = s_{\mathrm{SH},k} \cdot \dot{Q}_{\mathrm{h},k} \tag{5.18}$$

$$\dot{Q}_{\mathrm{h,DHW},k} = s_{\mathrm{DHW},k} \cdot \dot{Q}_{\mathrm{h},k} \tag{5.19}$$

Domestic Hot Water (DHW) storage: DHW storage is modeled to keep the constant temperature ($T_{\mathrm{DHW}} = 45\,^{\circ}\mathrm{C}$), while the usable volume of the hot water in storage, V_{DHW} (m^3), varies (Dengiz et al. 2019). The ΔT_{DHW} represents the difference between the reference temperature of the water T_{DHW} and tap water. The heat fluxes that affect the storage are $\dot{Q}_{\mathrm{DHW}}$, which represents the sum of heat fluxes of the heat pump $\dot{Q}_{\mathrm{h,DHW},k}$ and fuel cell $\dot{Q}_{\mathrm{hr,FC},k}$, DHW demand $\dot{Q}_{\mathrm{dm,DHW}}$ and standing losses $\dot{Q}_{\mathrm{l,DHW}}$, calculated in W:

$$V_{\mathrm{DHW},k} = V_{\mathrm{DHW},k-1} + \frac{\dot{Q}_{\mathrm{DHW},k} - \dot{Q}_{\mathrm{dm,DHW},k} - \dot{Q}_{\mathrm{l,DHW}}}{\Delta T_{\mathrm{DHW}} \cdot \rho_{\mathrm{H_2O}} \cdot c_{\mathrm{H_2O}}} \cdot t_{\mathrm{s}} \tag{5.20}$$

$$\dot{Q}_{\mathrm{DHW},k} = \dot{Q}_{\mathrm{h,DHW},k} + \dot{Q}_{\mathrm{hr,FC},k} \tag{5.21}$$

where the density and specific heat capacity of the water are denoted as $\rho_{\mathrm{H_2O}}$ and $c_{\mathrm{H_2O}}$, respectively. DHW storage is constrained by minimal and maximal volumes:

$$V_{\mathrm{DHW,min}} \leq V_{\mathrm{DHW},k} \leq V_{\mathrm{DHW,max}} \tag{5.22}$$

Thermal building model: The 4R3C gray-box thermal building model from Langner et al. (2024) is used for the evaluation of the methodology and in MPC as a control model. The model comprises three states: (i) indoor air temperature T_{air} represented by Equation (5.23), (ii) internal wall temperature $T_{\mathrm{w,in}}$ described by Equation (5.24), and (iii) external wall temperature $T_{\mathrm{w,out}}$ presented by Equation (5.25). The heat flux emitted by the heat pump is represented with $\dot{Q}_{\mathrm{h,SH}}$, while weather-related inputs are ambient air temperature T_{amb} and solar radiation $\dot{q}_{\mathrm{sol}}$:

$$C_{\mathrm{air}} \frac{\mathrm{d}T_{\mathrm{air}}}{\mathrm{d}t} = \frac{T_{\mathrm{w,in}} - T_{\mathrm{air}}}{R_{\mathrm{w,air}}} + \frac{T_{\mathrm{amb}} - T_{\mathrm{air}}}{R_{\mathrm{air,amb}}} + g_{\mathrm{sol}}\dot{q}_{\mathrm{sol}} + f_{\mathrm{conv}}\dot{Q}_{\mathrm{h,SH}} \tag{5.23}$$

$$C_{\mathrm{w}} \frac{\mathrm{d}T_{\mathrm{w,in}}}{\mathrm{d}t} = \frac{T_{\mathrm{air}} - T_{\mathrm{w,in}}}{R_{\mathrm{w,air}}} + \frac{T_{\mathrm{w,out}} - T_{\mathrm{w,in}}}{R_{\mathrm{w}}} + (1 - f_{\mathrm{conv}})\dot{Q}_{\mathrm{h,SH}} \tag{5.24}$$

$$C_{\mathrm{w}} \frac{\mathrm{d}T_{\mathrm{w,out}}}{\mathrm{d}t} = \frac{T_{\mathrm{w,in}} - T_{\mathrm{w,out}}}{R_{\mathrm{w}}} + \frac{T_{\mathrm{amb,eq}} - T_{\mathrm{w,out}}}{R_{\mathrm{w,amb}}} \tag{5.25}$$

where g_{sol} is the solar heat gain factor, f_{conv} is the convective share of heat flux, and $T_{\mathrm{amb,eq}}$ is the equivalent outdoor temperature at the exterior surfaces, with the effect of solar radiation taken into account.

Equations (5.23)-(5.25) represent the set of ordinary differential equations which define the thermal dynamics of the building. The set of ordinary differential equations is reformulated as a state-space system (see Equations (2.2)-(2.3)) and discretized using a zero-order hold method. The comfortable temperature constraints are introduced to exploit thermal building mass as an additional storage medium:

$$T_{\mathrm{air,min},k} \leq T_{\mathrm{air},k} \leq T_{\mathrm{air,max},k} \tag{5.26}$$

Power balance: The power balance is described as the equilibrium between generated and demanded power at time step k:

$$P_{\mathrm{PV},k} + P_{\mathrm{buy},k} + P_{\mathrm{el,FC},k} + P_{\mathrm{d},k} = P_{\mathrm{sell},k} + P_{\mathrm{el,load},k} + P_{\mathrm{el,HP},k} + P_{\mathrm{ch},k} \tag{5.27}$$

where $P_{\mathrm{buy},k}$ and $P_{\mathrm{sell},k}$ represent the purchased and sold power, respectively. The electrical load from appliances is denoted by $P_{\mathrm{el,load},k}$. This load is introduced to evaluate the EMS performance under a comprehensive building load: flexible $P_{\mathrm{el,HP}}$ and non-flexible $P_{\mathrm{el,load}}$.

Control algorithms

This subsection describes the developed control algorithm, namely the ComEMS4Build. Thereafter, the benchmark control strategies, RBC, which requires minimal information, and MPC, which is optimization- and model-based, are presented.

ComEMS4Build: Comfort-Oriented Energy Management System for Residential Buildings: This control strategy is developed to hierarchically split thermal load management, coordinated by FLC$_{\mathrm{flex}}$ and operation of the HESS, coordinated by FLC$_{\mathrm{FC}}$ and FLC$_{\mathrm{BESS}}$, as illustrated in Figure 5.2a. The FLC$_{\mathrm{flex}}$ operates the thermal load based on following input signals:

(i) Solar radiation $\dot{q}_{\mathrm{sol}}$, as external signal.

(ii) ECDF of the day-ahead electricity price signal $\hat{F}(p_{\mathrm{buy})}$ (see Equation (2.18)), also denoted as an external signal.

(iii) SOC (see Equation (5.2)) and LOH (see Equation (5.9)) as the indicator of the HESS state.

(iv) Binary variables s_{SH} and s_{DHW}, defining whether the heat pump is used for space or DHW heating:

$$s_{\mathrm{SH},k} = \begin{cases} 1, & \text{if } \chi_{\mathrm{SH},k} < \chi_{\mathrm{DHW},k}, \\ 0, & \text{otherwise,} \end{cases} \qquad s_{\mathrm{DHW},k} = \begin{cases} 1, & \text{if } \chi_{\mathrm{DHW},k} \leq \chi_{\mathrm{SH},k}, \\ 0, & \text{otherwise.} \end{cases} \tag{5.28}$$

Indoor air temperature thermal state $\chi_{\mathrm{SH},k}$ is defined as following:

$$\chi_{\mathrm{SH},k} = \sqrt{\frac{T_{\mathrm{air},k-1} - \max(T_{\mathrm{air,min},k}, T_{\mathrm{air,min},k+5})}{T_{\mathrm{air,max},k} - \max(T_{\mathrm{air,min},k}, T_{\mathrm{air,min},k+5})}} \tag{5.29}$$

where parameter $T_{\text{air,min},k+5}$ represents the minimal temperature constraint in the next five hours, used as an indicator for preheating. This thermal state is under the square root to control the temperature closer to the lower temperature constraint defined by the term $\max(T_{\text{air,min},k}, T_{\text{air,min},k+5})$. The DHW storage thermal state $\chi_{\text{DHW},k}$ is defined as following:

$$\chi_{\text{DHW},k} = \left(\frac{V_{\text{DHW},k-1} - V_{\text{DHW,min}}}{V_{\text{DHW,max}} - V_{\text{DHW,min}}} \right)^2 \tag{5.30}$$

This thermal state is squared to control the usable volume of the DHW closer to its upper volume constraint $V_{\text{DHW,max}}$, since future demand is unknown.

The FLC_{flex} suggests the modulation factor of the heat pump $\eta_{\text{el,HP},k} = \alpha_{\text{HP},k} + \eta_{\text{el,HP},k-1}$, where $\alpha_{\text{HP},k}$ is control signal which represents the increment or decrement of the modulation factor. Thereafter, the flexible load $P_{\text{el,HP}}$ is added to the non-flexible load $P_{\text{el,load}}$. After using the power generated by PV the residual load is defined $\Delta P_k = P_{\text{PV},k} - P_{\text{el,HP},k} - P_{\text{el,load},k}$. If the PV generation exceeds the demand, the fuel cell does not operate. If a residual load exists, the FLC_{FC} determines the amount that can be covered by the fuel cell, based on the following information:

(i) Residual power ΔP.

(ii) ECDF of the day-ahead electricity price signal $\hat{F}(p_{\text{buy}})$.

(iii) Toggling state of the fuel cell $s_{\text{on/off}}$.

(iv) HESS state as SOC and a percentage of allowable daily hydrogen consumption ΔLOH.

The allowable daily hydrogen consumption $\Delta E_{\text{H}_2,k}$ is relative to the absolute hydrogen energy left in the storage $E_{\text{H}_2,\text{k}}$ at the time step k. The variable $\Delta E_{\text{H}_2,\text{init}}$ is introduced as the initial allowable daily hydrogen consumption in kWh/day, which is updated each new day. The ΔLOH represents the percentage of allowable daily hydrogen consumption given as the input signal to FLC_{FC}:

$$\Delta \text{E}_{\text{H}_2,k} = \begin{cases} \frac{24\text{h} \cdot (E_{\text{H}_2,k} - E_{\text{H}_2,\text{min}})}{N-k} = \Delta E_{\text{H}_2,\text{init}}, & \text{if } k \bmod H = 0, \\ \Delta E_{\text{H}_2,k-1} + (E_{\text{H}_2,k} - E_{\text{H}_2,k-1}), & \text{otherwise.} \end{cases} \tag{5.31}$$

$$\Delta \text{LOH}_k = \frac{\Delta \text{E}_{\text{H}_2,k}}{\Delta \text{E}_{\text{H}_2,\text{init}}} \tag{5.32}$$

where N represents the time steps of the simulation, H one day horizon and k time step. The FLC_{FC} defines the power that the fuel cell should produce $P_{\text{el,FC},k} = \alpha_{\text{FC},k} \cdot \zeta \cdot P_{\text{el,FC,max}}$, where $\alpha_{\text{FC},k}$ represents control signal.

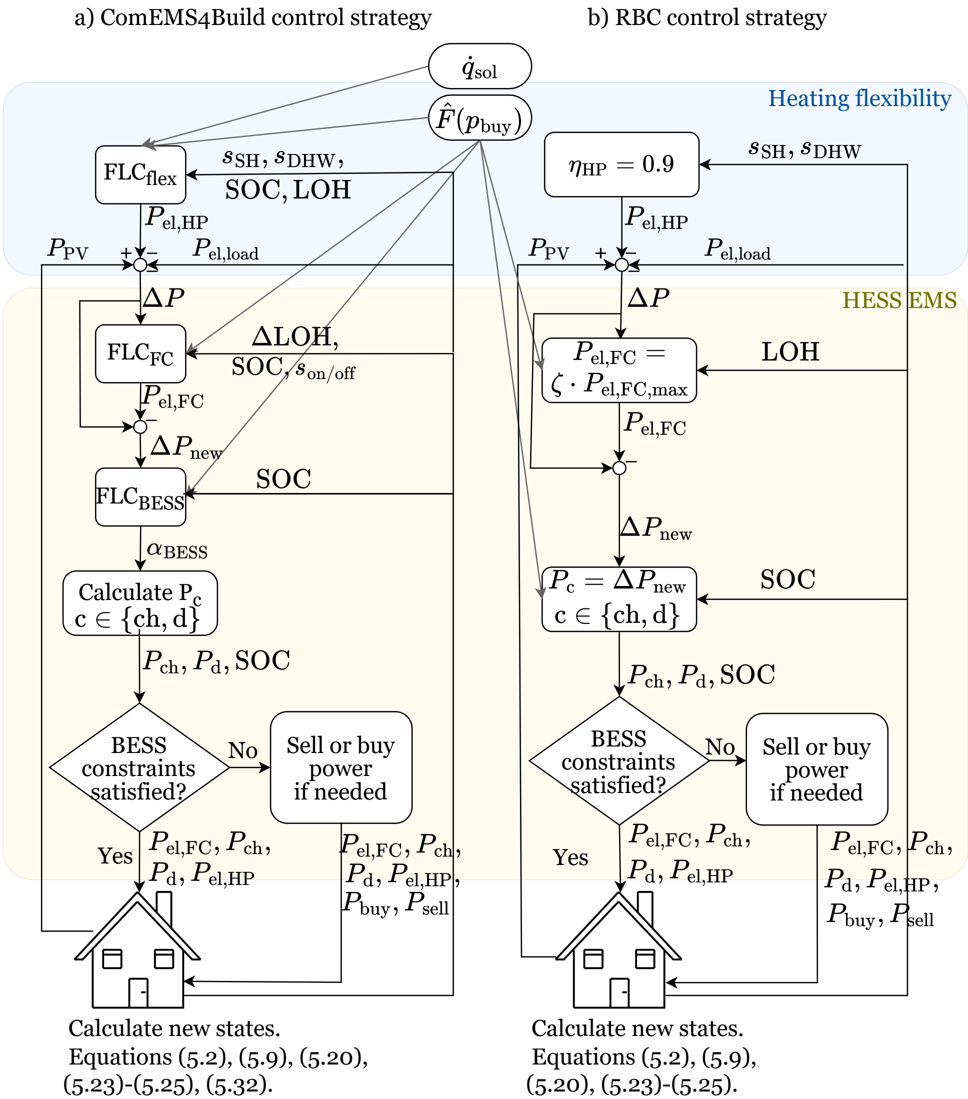

Figure 5.2: The flowcharts depicting the information flow of control strategies. Figure is adapted from Kovačević et al. (2025b).

The FLC$_{\mathrm{BESS}}$ manages operation of the BESS. It considers the following information:

(i) The residual power ΔP_{new} to fully satisfy the demand, defined as follows:

$$\Delta P_{\mathrm{new},k} = \Delta P_k - P_{\mathrm{el,FC},k} \tag{5.33}$$

(ii) ECDF of the day-ahead electricity price signal $\hat{F}(p_{\mathrm{buy}})$.

(iii) State of charge of BESS, i.e. SOC.

If the BESS cannot meet the rest of the residual power, whether due to power constraints or its state of charge being at the minimum or maximum level, the remaining power requirement is compensated by purchasing from or selling to the grid. The FLC$_{\mathrm{BESS}}$ defines following control signal:

$$\alpha_{\mathrm{BESS}} \in [-1, 1] \tag{5.34}$$

where the sign dictates whether the BESS is charged (positive) or discharged (negative). If the load ΔP_{new} is negative, meaning that demand exists, and α_{BESS} is positive, the entire deficit is purchased from the grid. In addition, if electricity prices are favorable, the BESS may also be charged. The purchased power from the grid is then defined as follows:

$$P_{\mathrm{ch},k} = \alpha_{\mathrm{BESS},k} \cdot P_{\mathrm{ch,max}} \tag{5.35}$$

$$P_{\mathrm{buy},k} = P_{\mathrm{ch},k} + |\Delta P_{\mathrm{new},k}| \tag{5.36}$$

On the other hand, if the control signal α_{BESS} is negative, the BESS will be discharged, and the rest will be purchased from the grid:

$$P_{\mathrm{d},k} = |\alpha_{\mathrm{BESS},k}| \cdot |\Delta P_{\mathrm{new},k}| \tag{5.37}$$

$$P_{\mathrm{buy},k} = (1 - |\alpha_{\mathrm{BESS},k}|) \cdot |\Delta P_{\mathrm{new},k}| \tag{5.38}$$

At the end, if the rest of the residual power is positive, indicating generation, and the control signal is positive, the control signal α_{BESS} dictates the ratio of charging the BESS and selling the power to the grid:

$$P_{\mathrm{ch},k} = \alpha_{\mathrm{BESS},k} \cdot \Delta P_{\mathrm{new},k} \tag{5.39}$$

$$P_{\mathrm{sell},k} = (1 - \alpha_{\mathrm{BESS},k}) \cdot \Delta P_{\mathrm{new},k} \tag{5.40}$$

Figures 5.3 and 5.4 illustrate the membership functions used in FLC$_{\mathrm{flex}}$, FLC$_{\mathrm{FC}}$ and FLC$_{\mathrm{BESS}}$ for inputs and control signals. Figures 5.3(a-c) illustrate the input signals describing the state of HESS as SOC, LOH and ΔLOH, building thermal state that is less favorable defined as $\min(\chi_{\mathrm{SH}}, \chi_{\mathrm{DHW}})$, fuel cell toggling state $s_{\mathrm{on,off}}$, and external signals, ECDF of electricity price signals $\hat{F}(p_{\mathrm{buy}})$ and current solar radiation $\dot{q}_{\mathrm{sol}}$. Figure 5.3d and Figure 5.4a illustrate membership functions of the residual power input signals that need to be covered by the fuel cell and BESS, respectively. Both sets are normalized on the scale of $10\,\mathrm{kW}$. Specific system values are used for defining the membership functions. For example, the "medium negative" membership function of residual power ΔP is chosen so that it peaks for the residual load that can be covered by the fuel cell's nominal power (see Table 5.2). On the other hand, the "big negative" membership function is designed so the load can be covered by operating both the fuel cell and BESS.

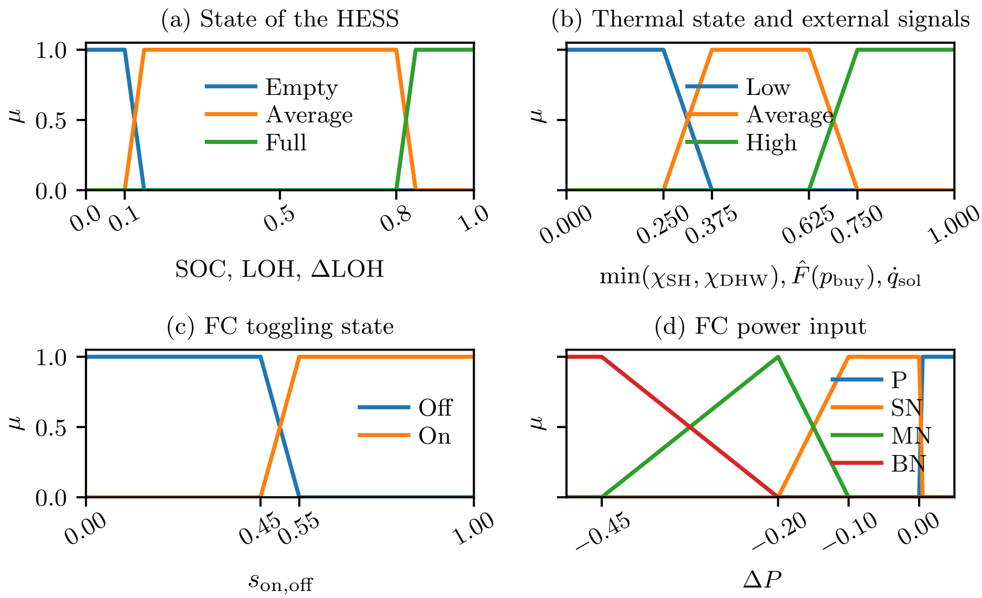

Figure 5.3: Membership functions used for input signals for $\mathrm{FLC_{flex}}$, $\mathrm{FLC_{FC}}$ and $\mathrm{FLC_{BESS}}$. The abbreviations are defined as follows: P – positive, SN – small negative, MN – medium negative, and BN – big negative. Figure is adapted from (Kovačević et al. 2025b).

A comparable approach is used to define the membership functions of the residual load ΔP_{new} in Figure 5.4a. The peaks of the "medium positive" and "medium negative" functions are selected such that, when ΔP_{new} indicates surplus generation, the BESS can be charged at its maximum power, and when ΔP_{new} denotes a demand, this demand can likewise be met by discharging the BESS at its maximum power (see Table 5.2). Subplots in Figure 5.4(b-d) depict the control signal membership functions of $\mathrm{FLC_{flex}}$, $\mathrm{FLC_{FC}}$ and $\mathrm{FLC_{BESS}}$, respectively.

Figure 5.5 depicts the input–output mapping for all three controllers. The $\mathrm{FLC_{flex}}$ is illustrated in Figure 5.5a, for the case when SOC$=10\%$ and LOH$=10\%$ and $\min(\chi_{\mathrm{SH}}, \chi_{\mathrm{DHW}}) = 0$, the other two inputs, ECDF of electricity price signal $\hat{F}(p_{\mathrm{buy}})$ and solar radiation $\dot{q}_{\mathrm{sol}}$, are varying. The figure shows that when the ECDF electricity price signal is relatively low or solar radiation

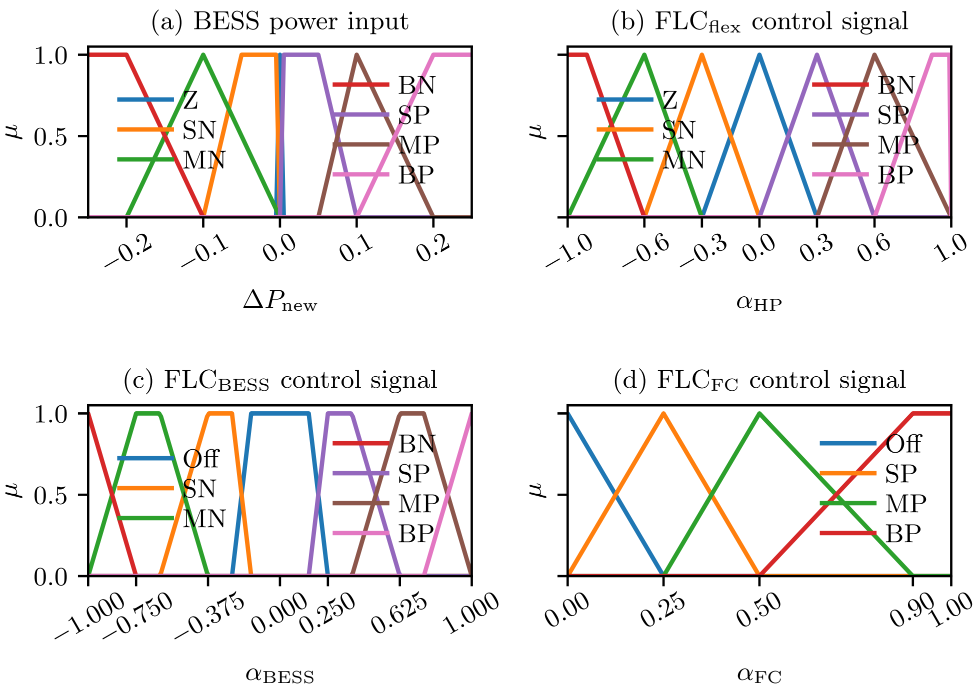

Figure 5.4: Membership functions for BESS power input signal and $\mathrm{FLC_{flex}}$, $\mathrm{FLC_{FC}}$ and $\mathrm{FLC_{BESS}}$ control signals. The abbreviations are defined as follows: Z – zero, SP – small positive, MP – medium positive, BP – big positive, SN – small negative, MN – medium negative, and BN – big negative. Figure is adapted from (Kovačević et al. 2025b).

is high, the controller uses these favorable conditions for heating by increasing the control signal α_{HP}.

Figure 5.5b depicts the input–output mapping for $\mathrm{FLC_{FC}}$ under following system conditions: (i) SOC$=10\%$, (ii) $\Delta\mathrm{LOH} = 80\%$ and (iii) $s_{\mathrm{on/off}} = 1$. The other two inputs, residual load ΔP and ECDF electricity price signal $\hat{F}(p_{\mathrm{buy}})$, vary. As both the absolute value of residual load and the ECDF price signal increase, the controller raises the value of α_{FC}, thereby increasing the output power of the fuel cell. Furthermore, when the load remains relatively low (below $1500\,\mathrm{kW}$, defined with a negative sign in the figure), and under the above-mentioned system conditions, $\mathrm{FLC_{FC}}$ tends to supply the entire load using only the fuel cell as the fuel cell is already turned on.

Figure 5.5c illustrates the $\mathrm{FLC_{BESS}}$ input–output mapping when SOC$=50\%$. When the ECDF electricity price signal approaches lower values and the residual load ΔP_{new} approaches zero, the control signal α_{BESS} increases. The positive values of the control signal α_{BESS} indicate the charging and that the load (if it exists) will be covered by purchasing from the grid (see

Equations (5.35) and (5.36)). On the other hand, when the residual load increases (depicted with a negative sign in the figure) and ECDF electricity price signal approaches higher value, the control signal becomes negative, indicating the battery discharging and purchasing from the grid (see Equations (5.37) and (5.38)). The overview and description of the rule base tables of all three controllers is given in Appendix D.1.

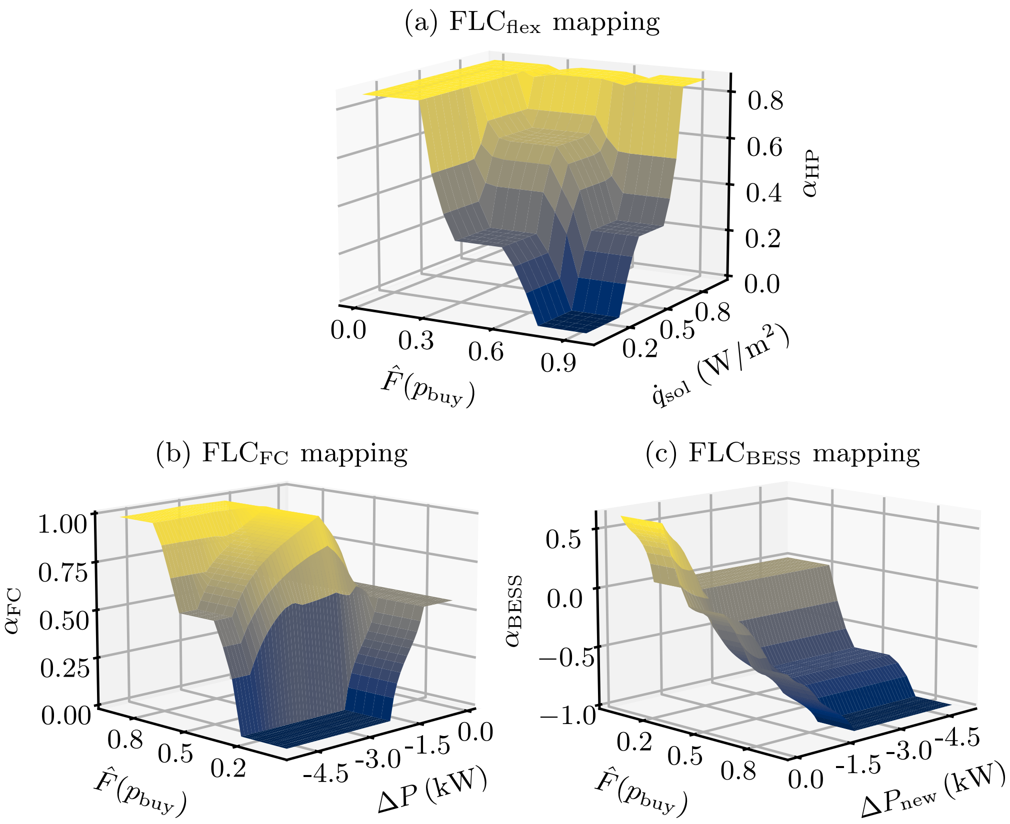

Figure 5.5: The ComEMS4Build input-output mapping for all three controllers.

Rule Based Control (RBC): The RBC presents the simpler version of the ComEMS4Build controller, developed with minimal input requirements. Figure 5.2b depicts the information flow of the RBC. Similarly to the ComEMS4Build controller, the thermal states χ_{SH} and χ_{DHW} are defined based on minimal and maximal temperatures ($T_{\mathrm{air,min}}$ and $T_{\mathrm{air,max}}$) and usable volume constraints ($V_{\mathrm{DHW,min}}$ and $V_{\mathrm{DHW,max}}$):

$$\chi_{\mathrm{SH},k} = \frac{T_{\mathrm{air},k-1} - T_{\mathrm{air,min}}}{T_{\mathrm{air,max}} - T_{\mathrm{air,min}}} \tag{5.41}$$

$$\chi_{\mathrm{DHW},k} = \frac{V_{\mathrm{DHW},k-1} - V_{\mathrm{DHW,min}}}{V_{\mathrm{DHW,max}} - V_{\mathrm{DHW,min}}} \tag{5.42}$$

while the binary variables s_{SH} and s_{DHW} follow the same logic as ComEMS4Build (see Equation (5.28)). The DHW and space heating are treated equally, and future temperature constraints are not accounted for. To avoid greater discomfort for occupants, and since future temperature constraints are unknown, the RBC uses constant temperature constraints (described in Section 5.1.2). If necessary, the heat pump is switched on with a constant modulation factor $\eta_{\mathrm{HP}} = 0.9$. Based on the sign of residual power ΔP, ECDF of the electricity price signals, and LOH, RBC considers whether the fuel cell should operate. In particular, if the load exists ($\Delta P < 0$) and the ECDF electricity price signal is in the upper quartile, the fuel cell will be turned on with maximal permissible power $P_{\mathrm{el,FC},k} = P_{\mathrm{el,FC,max}} \cdot \zeta$. Otherwise, it stays turned off. Thereafter, based on the sign of the residual load ΔP_{new}, SOC, and the ECDF electricity price signal, it is decided whether the BESS is charged or discharged. Here, if the ECDF electricity price signal is in the lower quartile, the BESS will be charged, and, if load exists, it will be purchased from the grid.

Model Predictive Control (MPC): MPC is developed as the optimization-based benchmark control algorithm. Using the models and forecasts, MPC solves the optimization problem and determines the control trajectory that minimizes the overall system operational cost. The cost function comprises three parts: (i) costs of power exchanged with the grid, (ii) fuel cell degradation costs, and (iii) initial investment and lifespan costs of the HESS:

$$\begin{aligned}\min \sum_{k=1}^{H} & \underbrace{t_{\mathrm{s}} \cdot (p_{\mathrm{buy},k} \cdot P_{\mathrm{buy},k} - p_{\mathrm{sell}} \cdot P_{\mathrm{sell},k})}_{\text{Costs of power exchange with grid}} + \underbrace{\sigma_{\mathrm{FC,on}} \cdot s_{\mathrm{FC,on},k} + \sigma_{\mathrm{FC,off}} \cdot s_{\mathrm{FC,off},k}}_{\text{Fuel cell degradation costs}} \\ & + \underbrace{t_{\mathrm{s}} \cdot (\sigma_{\mathrm{BESS,ch}} \cdot P_{\mathrm{ch},k} + \sigma_{\mathrm{BESS,d}} \cdot P_{\mathrm{d},k} + \sigma_{\mathrm{FC}} \cdot s_{\mathrm{FC},k})}_{\text{Investment and lifespan costs}}\end{aligned} \tag{5.43}$$

subject to Equations (5.1)-(5.27).

The H represents the one-day prediction horizon, and p_{sell} and p_{buy} define the remuneration price and the dynamic electricity price signal in EUR/kWh, respectively. The utilization costs of battery charging $\sigma_{\mathrm{BESS,ch}}$ (in EUR/kWh) and discharging $\sigma_{\mathrm{BESS,d}}$ (in EUR/kWh) and fuel cell operation σ_{FC} (EUR/h) comprise initial component investment costs σ_{in} (in EUR) and operation and maintenance costs σ_{om} (in EUR/h), defined as:

$$\sigma_i = \sum_i \frac{1}{\eta_i} \left(\frac{\sigma_{\text{in},i}}{L_i} + \sigma_{\text{om},i} \right), \quad i \in \{\text{“BESS,ch”}, \text{“BESS,d”}, \text{“FC”}\} \tag{5.44}$$

where L_i represents the lifespan of the corresponding component, measured in h. The lifespan of the fuel cell can be found in the datasheet, while the BESS's lifespan is estimated based on Depth of Discharge (DoD) cycles and maximal BESS capacity $E_{\text{BESS,max}}$ as described in Cau et al. (2014):

$$L_{\text{BESS},i} = \frac{E_{\text{BESS,max}}}{P_i} \cdot \text{DoD} \quad i \in \{\text{“ch”}, \text{“d”}\} \tag{5.45}$$

The costs of the fuel cell toggling in the objective function, Equation (5.43), are represented with $\sigma_{\text{FC,on}}$ and $\sigma_{\text{FC,off}}$ and are measured in EUR. The $s_{\text{FC,on}}$ and $s_{\text{FC,off}}$ indicate whether the fuel cell is starting or stopping, defined by the following logic:

$$s_{\text{FC,on},k} = s_{\text{FC},k} \wedge (\neg s_{\text{FC},k-1}) \tag{5.46}$$

$$s_{\text{FC,off},k} = s_{\text{FC},k-1} \wedge (\neg s_{\text{FC},k}) \tag{5.47}$$

The nonlinear behavior in Equations (5.7) and (5.8) arises from the dependency of the fuel cell's molar flow on its power output, estimated from the datasheet. To ensure robust convergence, the efficiency $\eta_{\text{el,FC}}$ is substituted by a constant value derived from the manufacturer's datasheet, a simplification commonly adopted in the literature (Wang et al. 2024). Given the 24 h prediction horizon of the MPC, the controller determines the permissible daily hydrogen usage by adjusting the minimum allowed level of hydrogen, $\text{LOH}_{\text{min},k}$, for each new day:

$$\Delta\text{LOH} = \frac{\text{LOH}_{\text{max}}}{\text{NoD}} \tag{5.48}$$

$$\text{LOH}_{\text{min},k} = \begin{cases} \min\left(\text{LOH}_{\text{min}},\ \text{LOH}_{\text{max}} - \Delta\text{LOH} \cdot \left(1 + \frac{k}{H}\right)\right) & \text{if } k \bmod H = 0, \\ \min(\ \text{LOH}_{\text{min}},\ \text{LOH}_{\text{min},k-1}) & \text{otherwise,} \end{cases} \tag{5.49}$$

where NoD represents the total number of days, H is a one-day horizon period, term $1 + k/H$ represent the corresponding day of the simulation and LOH_{min} is absolute minimal level of the hydrogen in storage. This additional constraint requires the MPC to respect a daily minimum level of hydrogen in storage.

Inputs required by each EMS: Table 5.1 outlines the required inputs for each EMS. The RBC requires the minimum number of inputs compared to other two controllers, i.e., besides the current thermal states T_{air} and V_{DHW} and HESS states, SOC and LOH, it also requires the day-ahead electricity price signal $\hat{F}(p_{\mathrm{buy}})$. The ComEMS4Build requires, in addition, the current allowable daily hydrogen consumption ΔLOH, the toggling state of the fuel cell $s_{\mathrm{on/off}}$, solar radiation, and future temperature constraints. The MPC is the most information-intensive controller, as it requires, in addition to the above-mentioned inputs, also the forecasting models[13] and profiles[14].

Table 5.1: The inputs required by each EMS.

Required inputs	T_{air}	V_{DHW}	SOC	LOH	ΔLOH	$s_{\mathrm{on/off}}$
RBC	✓	✓	✓	✓	—	—
ComEMS4Build	✓	✓	✓	✓	✓	✓
MPC	✓	✓	✓	✓	✓	✓
Required inputs	**Forecasting models**	**Forecasting profiles**	**Future temp. constraints**	$\hat{F}(p_{\mathrm{buy}})$	T_{amb}	$\dot{q}_{\mathrm{sol}}$
RBC	—	—	—	✓	—	—
ComEMS4Build	—	—	✓	✓	—	✓
MPC	✓	✓	✓	✓	✓	✓

5.1.2 Case study

The controllers' performance is evaluated for twelve German winter weeks. The weather-related data and electricity price signals span the period from December 2022 to February 2023. The models and control algorithms are implemented in Python, with the Gurobi optimizer (Gurobi Optimization LLC) used to solve the optimization problem. The simulation is performed with a time step of 1 h, while the MPC prediction horizon is one day.

Assuming that renewable hydrogen is produced during the German summer months, the hydrogen storage is considered to be full, reaching its maximum capacity $E_{\mathrm{H_2,max}}$ at the beginning of the winter-period simulation. Moreover, the SOC is set to 50% at the beginning of the simulation.

[13] The forecasting models incorporate PV, HESS, fuel cell, DHW storage, heat pump, and thermal building model.
[14] The forecasting profiles include weather-related information, DHW thermal load, and appliances' electrical load.

Input data

The demand profiles DHW demand $\dot{Q}_{\mathrm{dm,DHW}}$ is generated by DHWCalc tool (Jordan and Vajen 2005), while the electricity demand $P_{\mathrm{el,load}}$ for a four-person household is generated by LPG tool (Pflugradt et al. 2022). The hourly dynamic electricity price signal p_{buy} comprises the constant base part and a variable part retrieved from aWATTar GmbH. The reimbursement price signal p_{sell} has a constant value of 7.94 $\mathrm{cent/kWh}$, as reported by the German Federal Network Agency (Bundesnetzagentur). The weather-related data are obtained from the German Weather Service (Deutscher Wetterdienst - DWD) for the city of Rheinstetten, the nearest available weather station to the case study location.

Occupancy schedule and thermal building parameters: The occupancy schedule is specified by temperature constraints $T_{\mathrm{air,min}}$ and $T_{\mathrm{air,max}}$ within which the controller should operate. The profile utilized for ComEMS4Build and MPC is one profile for the entire building depicted in Figure 4.9 under the parameter names $T_{\mathrm{air,min,R1/R2}}$ and $T_{\mathrm{air,max,R1/R2}}$. Since the RBC does not consider future information, the temperature constraints are kept constant to ensure that comfort is not violated: $T_{\mathrm{air,min}} = 21\,^{\circ}\mathrm{C}$ and $T_{\mathrm{air,max}} = 24\,^{\circ}\mathrm{C}$. The parameters of the gray-box thermal building model are identified and validated for the LLEC building during the German winter months and are detailed in Langner et al. (2024).

DHW storage and heat pump parameters: For the DHW storage size of 300 l and A+ efficiency level, the standing losses are $\dot{Q}_{\mathrm{l,DHW}} = 35\,\mathrm{W}$ based to EU regulation 814/2013 (German Environment Agency). The DHW storage is used as heat storage, where heated water is not directly used but rather the heat is transferred via a heat exchanger to the fresh water supply. In this way, hygiene-related issues are avoided, and the temperature of the DHW is maintained at $45°\mathrm{C}$ (Dengiz et al. 2019). In addition, the heat recovered by the fuel cell can be used to heat the technical water (Suissetec). The overview of the DHW parameters is given in Table 5.2. The air/water heat pump Therma V Monobloc type HM051M U43 (LG Electronics) with heating capacity of 5 kW is chosen for the present case study. Besides heating up to the DHW temperature of $45\,^{\circ}\mathrm{C}$ (with COP variation 1.93–5.16), heat pump is also utilized for underfloor heating on $55\,^{\circ}\mathrm{C}$ (COP[15] variation 1.6–4.15).

Renewable energy system parameters: The parameters of the PV system and the BESS are derived from the equipment installed in the LLEC experimental building and presented in Table 5.2. The fuel cell used is the Horizon Educational H-2000 (Horizon Fuel Cell Europe, s.r.o). The restriction factor $\zeta = 80\%$ is introduced to limit the fuel cell's operation to 80% of its maximum

[15] Note that both COP variations for supply temperature of $45\,^{\circ}\mathrm{C}$ and $55\,^{\circ}\mathrm{C}$ are for the following outside temperature range: -15 °C–20 °C.

power output. This restriction is necessary because operating at maximum power significantly accelerates fuel-cell degradation (Fletcher et al. 2016, Andrade et al. 2025). Achieving full autarky would require a significantly larger HESS, as the system would need to cover demand peaks in worst-case scenarios. Therefore, the hydrogen storage is dimensioned to supply roughly half of the daily electricity demand during the winter months. Using the average electrical fuel cell efficiency, the corresponding hydrogen demand was calculated and is summarized in Table 5.2. The fuel cell system efficiency with heat recovery $\eta_{\mathrm{FC,sys}}$ is assumed to be 75% (Gandiglio et al. 2014). In addition, the heat recovery is discussed when the system achieves 90% efficiency (Ellamla et al. 2015, Nguyen and Shabani 2020). The operation of the electrolyzer is not considered in the present case study, as it is assumed that its operation would not be optimal during the German winter period when the demand is at its peak and PV generation is relatively small.

Table 5.2: Parameters used in the present case study for the following energy components: PV, BESS, DHW storage, fuel cell, and hydrogen storage.

Component	Variable	Value	Variable	Value
PV	n_{module}	30	η_{STC}	0.19
	a_{module}	1.685 m^2	$NOTC$	50 °C
	η_{T}	0.005 $°\mathrm{C}^{-1}$	T_{STC}	25 °C
	$\eta_{\mathrm{L\&T}}$	0.9		
BESS	$E_{\mathrm{BESS,max}}$	6.5 kWh	$P_{\mathrm{d,max}}$	1 kW
	η_{ch}	0.93	$\mathrm{SOC}_{\mathrm{min}}$	0.1
	η_{d}	0.93	$\mathrm{SOC}_{\mathrm{max}}$	0.9
	$P_{\mathrm{ch,max}}$	1 kW	$\mathrm{SOC}_{\mathrm{init}}$	0.5
DHW Storage	$V_{\mathrm{DHW,max}}$	300 l	$V_{\mathrm{DHW,min}}$	40 l
	$\dot{Q}_{\mathrm{l}}$	35 W	T_{DHW}	45 °C
Fuel cell	$P_{\mathrm{FC,max}}$	2441.6 W	$P_{\mathrm{FC,nom}}$	2000 W
	$P_{\mathrm{FC,min}}$	399.2 W	$\eta_{\mathrm{FC,sys}}$	0.75
Hydrogen storage	$E_{\mathrm{H_2,max}}$	1800 kWh	$\mathrm{LOH}_{\mathrm{max}}$	1

HESS degradation costs: The main degradation drivers for hydrogen system components relevant to supervisory EMS are on–off cycling and power fluctuations (Stropnik et al. 2022). Maintaining steady-state fuel-cell operation can extend its lifetime by a factor of 12–18 compared to dynamic operation. Table 5.3 shows the parameters related to the degradation costs of the fuel cell and BESS. The parameters are further derived from NKON B.V., The Fuel Cell Store and Wang et al. (2024). The operation and maintenance, and on/off costs of the battery are assumed to be negligible relative to those defined for the fuel cell.

Table 5.3: Degradation costs of fuel cell and BESS.

Component	Variable	Value	Variable	Value
Fuel cell	$\sigma_{\mathrm{in,FC}}$	10908 EUR	$\sigma_{\mathrm{om,FC}}$	0.038 EUR/h
	L_{FC}	35000 h	$\sigma_{\mathrm{FC,on}}$	0.10 EUR
	$\sigma_{\mathrm{FC,off}}$	0.053 EUR		
BESS	$\sigma_{\mathrm{in,BESS}}$	900 EUR	DoD	6000 cycles

Evaluation metrics

The weekly thermal discomfort d_{we} (see Equations (2.15)-(2.16)) and weekly operation σ_{buy} and reimbursement energy costs σ_{sell} (see Equation (2.17)) are used for an evaluation. HESS and grid usage are evaluated weekly, by discussing the following: (i) battery charged energy $E_{\mathrm{BESS,ch}}$, (ii) fuel cell energy generation E_{FC}, (iii) purchased and sold energy E_{buy} and E_{sell} respectively and (iv) heat recovered $E_{\mathrm{FC,hr}}$.

Furthermore, total working hours and the number of times the fuel cell is switched on and off are evaluated, based on the following equations:

$$\mathrm{WH} = t_{\mathrm{s}} \cdot \sum_{k=1}^{N} s_{\mathrm{FC},k} \tag{5.50}$$

$$\mathrm{TOG} = \sum_{k=1}^{N} s_{\mathrm{FC,on},k} \tag{5.51}$$

The working hours WH are correlated with the fuel cell binary variable s_{FC} and the sampling time t_{s}, while the number of times the fuel cell is switched on and off depends on the fuel cell toggling state $s_{\mathrm{FC,on}}$.

5.1.3 Results and discussion

Figures 5.6 and 5.7 illustrate the performance of all three controllers in two cases: (i) low solar radiation and high electricity price peaks, and (ii) relatively high solar radiation in winter and low electricity price signals, respectively. The controllers are organized into columns, with the first row showing the indoor air temperature, temperature constraints, and the volume of the DHW storage. The second row shows the PV generation and the total electricity load, denoted by $P_{\mathrm{el,load}} + P_{\mathrm{el,HP}}$. Furthermore, the exchange with the grid and the dynamic electricity price signal are shown in the third row, while the latter two rows depict HESS utilization.

When solar radiation is low, and electricity price signals exhibit high peaks, the MPC controls the indoor air temperature to remain at the lower temperature constraint $T_{\mathrm{air,min}}$, as illustrated in Figure 5.6. While the RBC exhibits hysteresis behavior with large fluctuations in indoor air temperature, the ComEMS4Build maintains a temperature, typically in the middle range. Throughout the entire simulation, all three controllers fulfill the DHW demand at each time step. Furthermore, the DHW storage volume controlled by the ComEMS4Build and RBC is usually kept at higher levels as the consumption prediction is not known to the controller. On the other hand, MPC, with a perfect DHW demand forecast, keeps the storage volume only as high as needed to satisfy short-term demand, thereby reducing energy consumption. However, these MPC actions are unrealistic, as DHW consumption is fundamentally stochastic. Furthermore, all three controllers aim to use the grid when electricity prices are low (see third row Figure 5.6). In contrast, when electricity price signals peak, controllers use HESS to relieve the grid. During periods of low demand, such as at midday on Dec. 3, when electricity prices are high, the RBC drives the fuel cell at maximum power. Because consumption is low, the surplus electricity is charged to the BESS, and any remaining power is sold. The MPC, however, does not find it optimal to sell energy to the grid. Rather, it prefers to store the energy in BESS, a logic that is also followed by ComEMS4Build.

In contrast to the unfavorable grid and weather situation from Figure 5.6, when the solar radiation is higher, and electricity price signals are lower, the MPC and ComEMS4Build use thermal building mass to store the thermal energy, as illustrated in Figure 5.7. This behavior cannot be observed by RBC, as it only controls indoor air temperature via hysteresis. Notably, MPC minimizes grid utilization and relies only on PV generation and HESS. After 10 weeks of the simulation period, ComEMS4Build has slightly less than 30% of the hydrogen left, while the RBC has almost depleted the hydrogen storage.

Electricity costs and thermal comfort

Figure 5.8 outlines weekly electricity and reimbursement costs for all three controllers. The ComEMS4Build and RBC achieve similar distribution of weekly operational electricity costs. However, the ComEMS4Build has median of 26.94 EUR while the RBC has median higher for 9.17 EUR compared to ComEMS4Build. The MPC has the lowest operational costs, with a median of 12.96 EUR, which is around half of ComEMS4Build costs. The MPC reaches two outliers with high weekly operational costs of 64.35 EUR and 61.24 EUR. Respectively, in these two weeks ComEMS4Build reaches also high costs of 78.92 EUR and 87.96 EUR and RBC of 77.9 EUR and 91.67 EUR. These two weeks are characterized by low PV generation and high electricity prices, with short, low-price periods. Because the controllers cannot purchase sufficient energy during low-price periods, they must also purchase energy during periods of

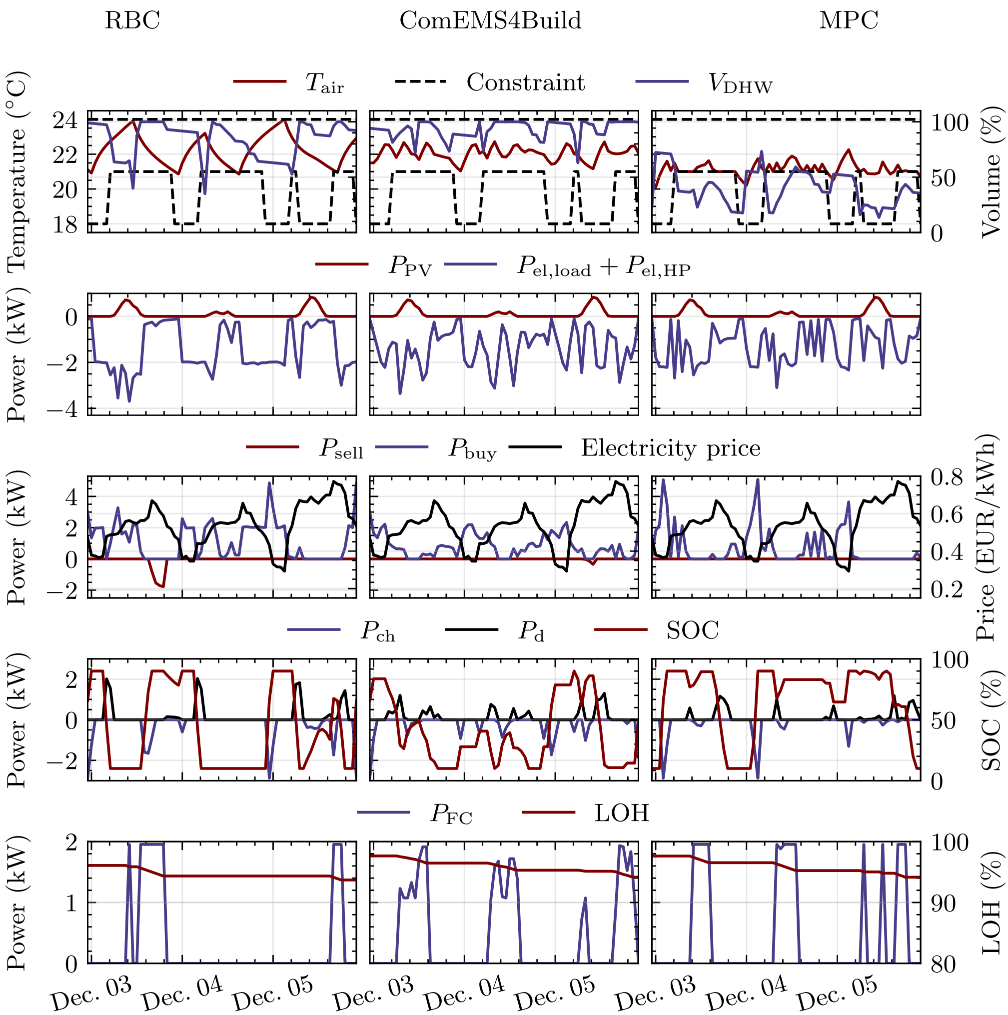

Figure 5.6: Performance comparison for all three controllers, when the solar radiation is relatively low. The figure is adapted from Kovačević et al. (2025b).

higher electricity prices. The increased electricity costs of RBC and ComEMS4Build are also affected by the increased heating demand for DHW storage. Since these two controllers lack a forecast of DHW demand, they keep DHW storage usually above 50% full, thereby increasing the demand and, consequently, the electricity costs. Conversely, MPC uses ideal forecasting to manage demand, ensuring that storage is sufficiently filled to cover short-term demand. While this makes the ComEMS4Build and RBC more robust to changes in DHW demand, the MPC can be sensitive to forecast errors.

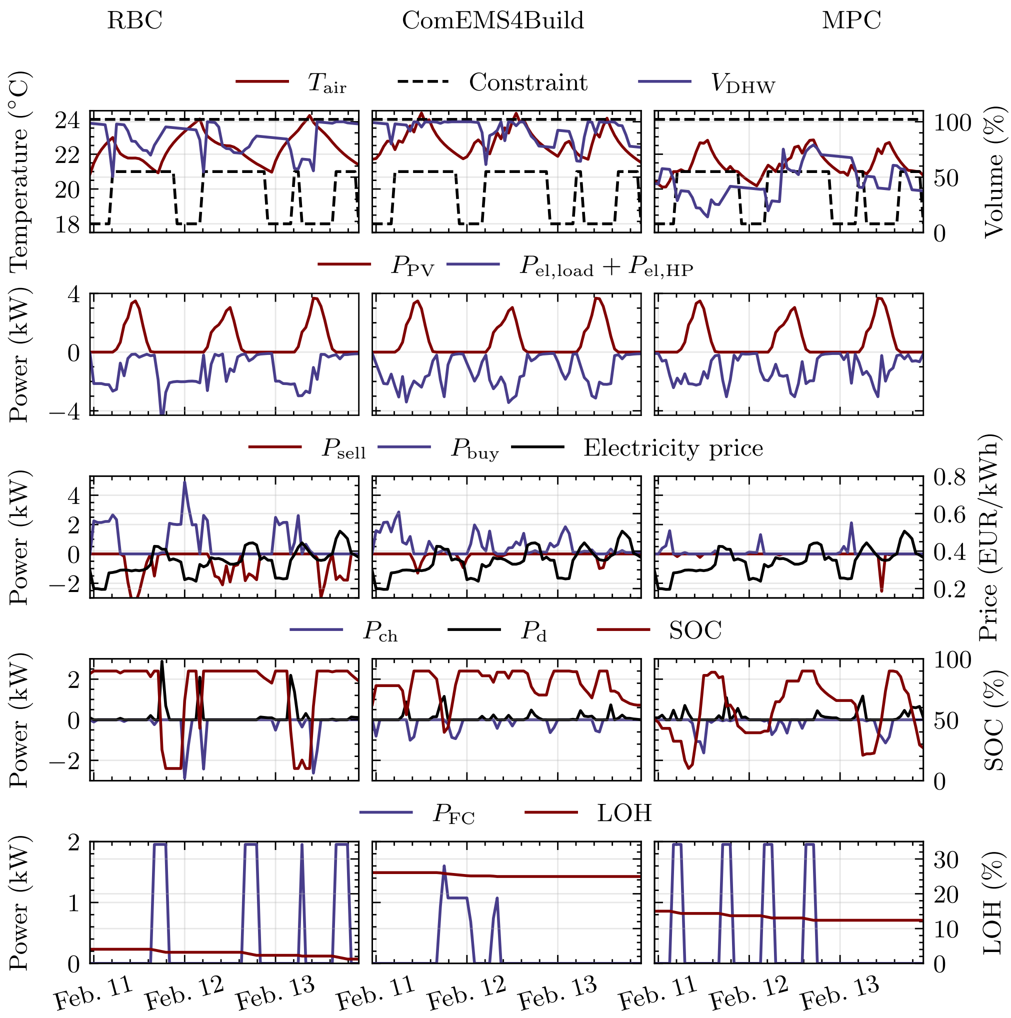

Figure 5.7: Performance comparison for all three controllers on winter days with relatively high solar radiation.

Selling the energy does not yield a notable revenue for any of the three controllers. Based on the median values, MPC does not sell energy to the grid. Rather, it tries to store the generated power within the system, since it does not find it optimal to sell at the reimbursement price of $7.94\,\mathrm{cent/kWh}$. The ComEMS4Build has slightly higher median of $0.51\,\mathrm{EUR}$, while the RBC has median of $2.71\,\mathrm{EUR}$.

The operational costs can also be reduced by minimizing energy consumption alone, but this would violate occupants' thermal comfort (as discussed in Section 4.1), which should not be

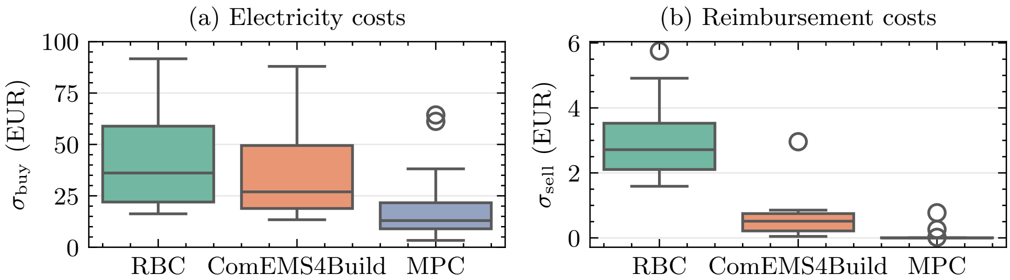

Figure 5.8: Weekly electricity (a) costs and (b) reimbursement. Figure is adapted from Kovačević et al. (2025b).

compromised. Thus, the weekly thermal discomfort is evaluated and illustrated in Figure 5.9. The RBC exhibits the largest weekly discomfort with a median of 0.68 Kh. On the other hand, the MPC achieves the best performance without violating comfort. Similarly, the ComEMS4Build does not violate the comfort in 10 out of 12 weeks. In the remaining two weeks, the comfort violation arises from the excess energy stored in the thermal mass of the building. Over these two weeks, the discomfort has been 0.9 Kh and 2 Kh. These deviations are caused by the ComEMS4Build's soft temperature constraints, which are used to locate the indoor air temperature within the specified range (see Equation (5.29)). Since these constraints are not strict, periods of high solar gain can result in slight overheating above the upper temperature constraint (see Figure 5.7).

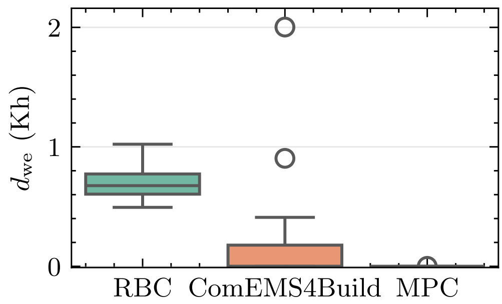

Figure 5.9: Weekly discomfort evaluated for all three controllers. Figure is adapted from Kovačević et al. (2025b).

HESS and grid utilization

The weekly HESS utilization is illustrated in Figure 5.10, by considering the BESS charging and hydrogen consumption in kWh. The ComEMS4Build and MPC have similar distribution of the weekly BESS charged energy, with the medians of 26.90 kWh and 27.15 kWh, respectively. The RBC uses the BESS the most, with weekly charged energy of 49.04 kWh. Since the RBC controls the fuel cell at its maximum permissible power, any surplus power after the demand has been met is directed to charging the BESS. Conversely, the ComEMS4Build does not control the fuel cell at maximum power, thereby facilitating smarter power control decisions.

Hydrogen consumption, illustrated in Figure 5.10b, shows that the ComEMS4Build has the lowest weekly difference in consumption, while the MPC largely differs in the weekly consumed hydrogen. The median values lists 69.17 kWh, 74.64 kWh and 79.11 kWh for ComEMS4Build, MPC and RBC, respectively. The RBC exhibits an outlier because it has already depleted its hydrogen storage, and thus, hydrogen is not consumed in the last week of the simulation.

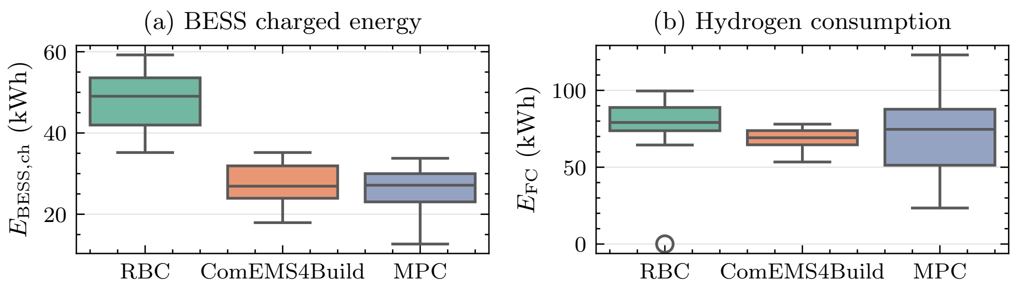

Figure 5.10: Weekly HESS usage. Figure is adapted from Kovačević et al. (2025b).

Figure 5.11 illustrates the influence of the electricity price signal on hydrogen consumption during the entire simulation period. The weekly MPC hydrogen variation is mostly affected by electricity price signals. Indeed, MPC consumes less hydrogen in periods when electricity price signals are very low (less than 0.2 $\mathrm{EUR/kWh}$). In contrast, when the electricity prices are higher, MPC relies more on fuel cell power generation and thus consumes more hydrogen. The ComEMS4Build, on the other hand, only obtains the information of the relative electricity price signal based on ECDF (see Section 2.3.3). Thus, the absolute value of the electricity price signal does not affect weekly hydrogen consumption, which is relatively constant.

Furthermore, the RBC depletes the hydrogen storage before the end of the evaluation period because it lacks information about the allowable daily hydrogen consumption. The MPC ends the simulation with 5.21% and the ComEMS4Build with 16.92% LOH. The rest of the hydrogen could potentially save for MPC 36.04 EUR and for ComEMS4Build 116.96 EUR when considering the average electricity price signal of the observed evaluation period, i.e., 0.39 $\mathrm{EUR/kWh}$.

Figure 5.12 depicts the fuel cell's toggling counts and working hours, as these have a significant impact on the fuel cell degradation. Compared to the MPC, RBC increases working hours by 2.7% and toggling counts by 8.7%. The small difference between the MPC and RBC stems from the fact that both operate the fuel cell primarily at the maximum allowable power, MPC as it finds

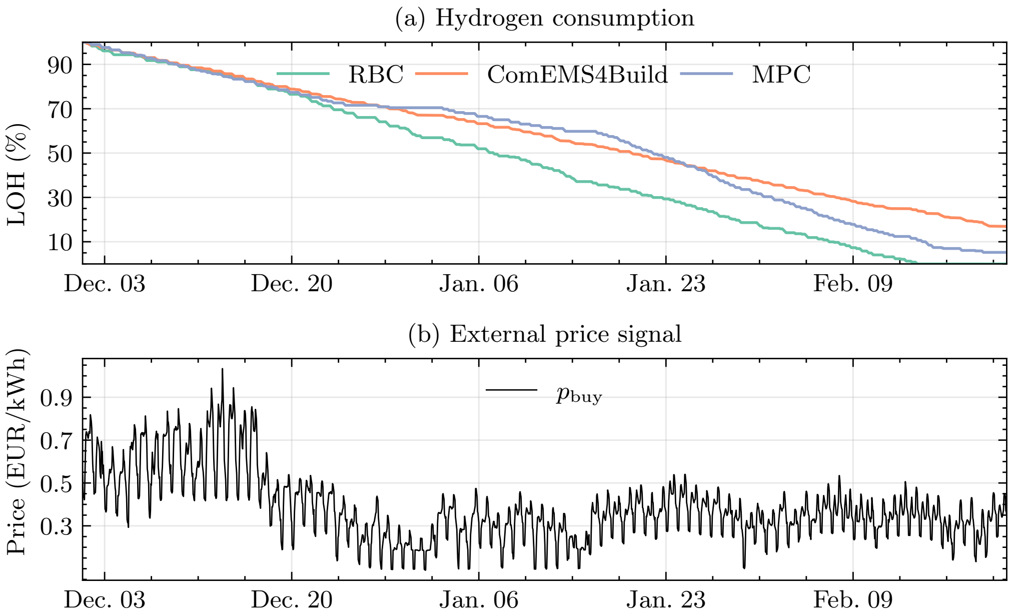

Figure 5.11: The influence of the (b) electricity price signal on (a) hydrogen consumption.

it optimal, and RBC due to its design. On the other hand, ComEMS4Build increases the working hours by almost half and toggling counts for 1.7% compared to MPC. The ComEMS4Build does not necessarily operate the fuel cell at the maximum allowable load, which increases the working hours.

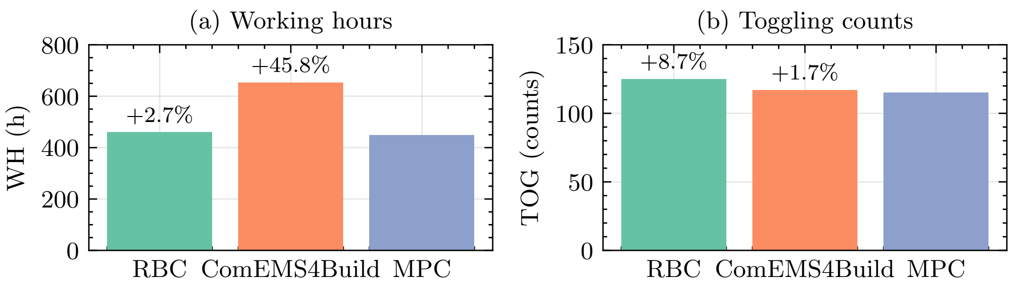

Figure 5.12: Total working hours and toggling counts of the fuel cell operation.

The grid usage is presented as weekly purchased energy Figure 5.13a and weekly sold energy Figure 5.13b. Purchased energy and sold energy comparison correlate with the electricity costs (see Figure 5.8a) and reimbursement costs (see Figure 5.8b), respectively. The following median values are observed: (i) RBC – for purchased energy 121.89 kWh and for sold energy 34.19 kWh, (ii) ComEMS4Build – for purchased energy 96.28 kWh and for sold energy 6.48 kWh, and (iii) MPC – for purchased energy 70.19 kWh and no sold energy. Comparing the median reimbursement costs and the sold energy, RBC receives only 2.2 EUR more weekly than ComEMS4Build, while it sells weekly notably more energy, i.e. 27.71 kWh.

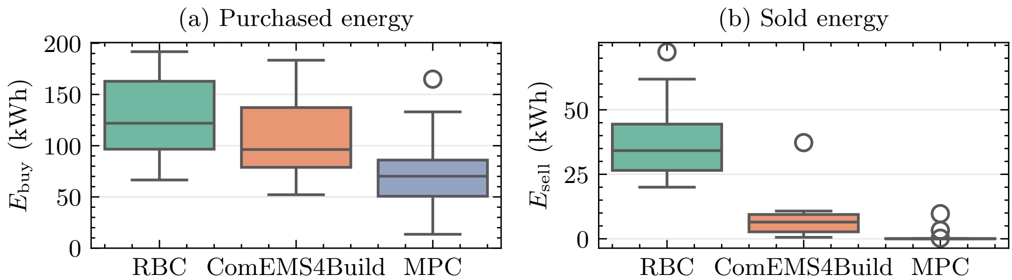

Figure 5.13: Weekly grid utilization. Figure is adapted from Kovačević et al. (2025b).

Heat recovery from fuel cell

Comparison of the weekly fuel cell heat recovery with weekly DHW demand is illustrated in Figure 5.14. The initial fuel cell system efficiency undertaken throughout the present study is 75% (Gandiglio et al. 2014). However, the heat recovery is also evaluated for a fuel cell system efficiency of 90%, as reported in the literature (Nguyen and Shabani 2020, Ellamla et al. 2015). Results for 75% of fuel cell system efficiency are shown without transparency, whereas those for 90% of fuel cell system efficiency are presented with transparent bars in the Figure 5.14. Considering a fuel cell system efficiency of 75%, none of the controllers can meet the DHW demand solely from recovered heat. On the other hand, when the fuel cell system efficiency reaches 90%, and the RBC is utilized, the heat recovery in weeks 4, 6, 7, and 8 would be sufficient to cover the weekly DHW demand. Moreover, MPC covers the weekly DHW demand only by operating the fuel cell in weeks 8 and 9. Conversely, the ComEMS4Build does not meet the DHW demand solely by fuel cell operation at any efficiency, as it does not always operate the fuel cell at its maximum allowable load, where thermal efficiency is usually highest.

Figure 5.15 illustrates three days controller comparison in week 8 when the fuel cell system efficiency is 90%. During the considered period, the discrepancy between electricity price signals is low, and periods when the electricity price signal is in the upper quartile last longer. In this case, RBC utilizes the fuel cell to meet demand during longer intervals. MPC also uses the fuel cell during longer periods when electricity price signals are highest, compared to the day-ahead

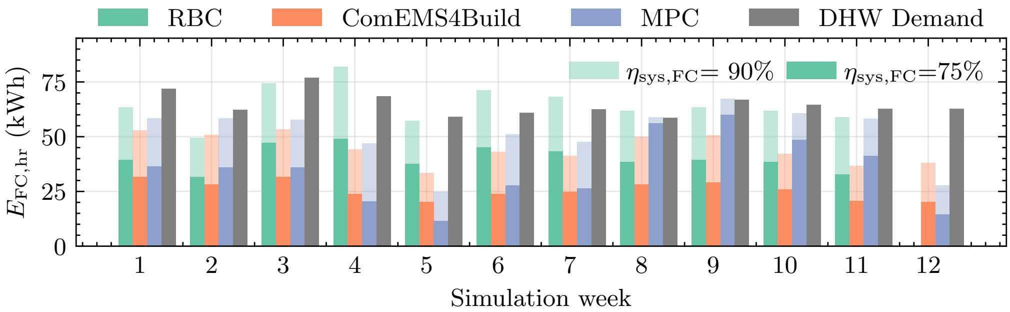

Figure 5.14: Weekly fuel cell heat recovery when the fuel cell operates with 75% and 90% system efficiency. Figure is adapted from Kovačević et al. (2025b).

period, and utilizes the grid in only short periods when the electricity prices are the lowest, compared to the day-ahead period. This behavior of the electricity price signal also affects the amount of recovered heat, which in this case would be sufficient to cover the DHW demand on a weekly basis.

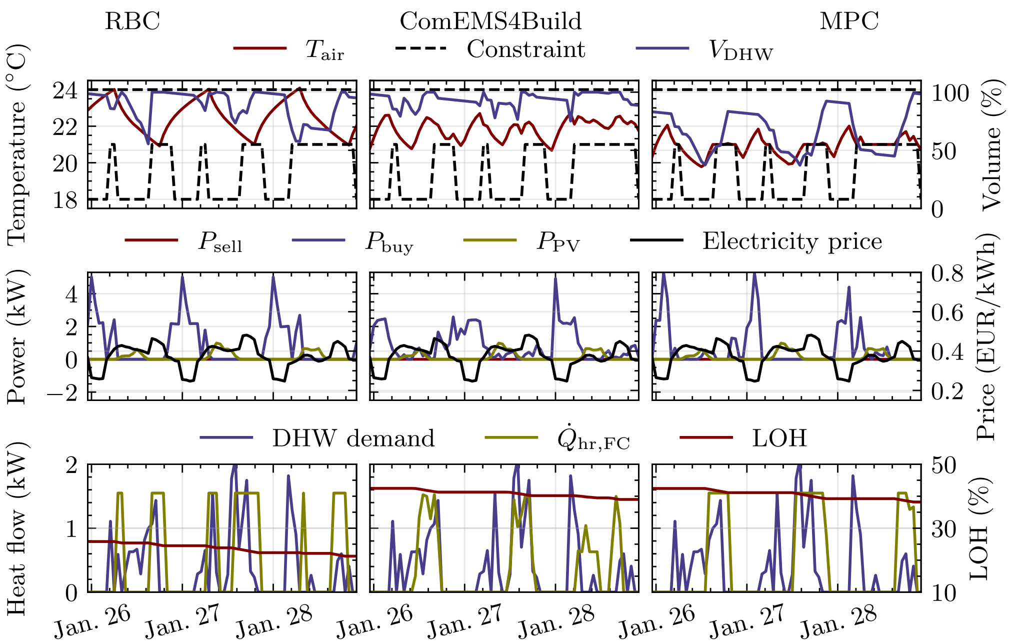

Figure 5.15: Performance comparison for all three controllers during week 8 with fuel cell system efficiency of 90%.

Interestingly, the MPC utilizes the fuel cell the least in weeks 5 and 12 (see Figure 5.14). These weeks are characterized by low electricity price valleys (reaching values under $0.2\,\mathrm{EUR/kWh}$). Purchased power is prioritized over heat recovered from the fuel cell, even though this recovered heat directly impacts electricity costs by reducing the heat pump's workload.

Summary

The results indicate that ComEMS4Build outperforms RBC in comfort-oriented metrics, showing no thermal discomfort in 10 of the 12 evaluated weeks and maintaining more stable indoor temperatures. The ComEMS4Build increases the indoor air temperature when grid conditions are favorable, or PV generation is high, effectively storing energy in the thermal building mass and shifting load from peak to off-peak periods (see Figure 5.7). In contrast, RBC operates as a hysteresis controller, cycling between temperature constraints.

Regarding power flows, RBC exports considerably more electricity to the grid than both ComEMS4Build and MPC, because it consistently operates the fuel cell at its maximum allowable power. After meeting building demand, it charges the BESS and exports the remaining energy. Conversely, MPC avoids exporting energy due to low reimbursement prices. Instead, it smartly retains energy within the building.

In terms of fuel cell operation, MPC has the lowest operating hours and toggling counts compared to the other two control strategies. ComEMS4Build slightly increases toggling counts and nearly doubles operating hours compared with MPC, as it operates the fuel cell for longer durations at lower loads, thereby achieving a higher fuel cell electrical efficiency. Potential enhancements for ComEMS4Build include introducing constraints to enforce longer uninterrupted operating periods or considering additional input signals related to the fuel cell's degradation costs.

For thermal performance, none of the controllers can meet the DHW demand solely from recovered fuel-cell heat at a cogeneration efficiency of 75%. With a higher efficiency of 90%, RBC can meet the demand using only recovered heat in weeks 4, 6, 7, and 8. However, RBC consumes hydrogen more actively early in the evaluation period, depleting storage before the end of the simulation period. ComEMS4Build generally recovers less heat than MPC and RBC because its lower fuel cell loads yield higher electrical efficiencies but reduced heat output.

A summary of the comparison of all three controllers is presented in Table 5.4. Although MPC can achieve cost-optimal operation, it relies on accurate forecasting models and predicted demand profiles, making it fragile to forecasting errors, particularly for highly stochastic profiles such as the DHW demand. Consequently, MPC requires the largest number of input signals. Beyond additional sensor installations, MPC also needs model training and periodic retraining, e.g., for

Table 5.4: Summary of the controllers' performance and features. A poor performance is indicated by 🔴, average performance by 🟡 and good performance by 🟢.

Controller	Model-free	Forecast-free	Number of inputs	HESS utilization	Thermal build. mass utilization	Exchange with grid
RBC	🟢	🟢	🟢	🔴	🔴	🔴
ComEMS4Build	🟢	🟢	🟡	🟡	🟢	🟡
MPC	🔴	🔴	🔴	🟢	🟢	🟢

Controller	Discomfort	Electricity costs	Reimbursement costs	Fuel cell working hours	Fuel cell toggling counts	Heat recovery
RBC	🔴	🔴	🔴	🟡	🔴	🟡
ComEMS4Build	🟡	🟡	🟡	🔴	🟡	🔴
MPC	🟢	🟢	🟢	🟢	🟢	🟢

the thermal building model. In contrast, ComEMS4Build is more robust because it does not rely on forecasting models or future profiles. While it does not guarantee an optimal solution, it reliably provides "sufficiently good" performance with lower input requirements than MPC. Compared with ComEMS4Build, the RBC further reduces the required inputs, making it the simplest of the evaluated control algorithms.

5.2 Contributions

By developing and evaluating a building with distributed energy resources that incorporates photovoltaics, a battery energy storage system, hydrogen storage, and thermal building mass as an additional storage medium, this work contributes to **RQ4**. In this configuration, both the fuel cell and the heat pump enable effective load shifting from on-peak to off-peak periods, thereby contributing to demand response programs.

Furthermore, the design and assessment of a soft-computing control strategy based on fuzzy logic addresses **RQ5**. The developed controller, Comfort-Oriented Energy Management System for Residential Buildings (ComEMS4Build), is positioned as a model- and forecast-free alternative that reduces input requirements and avoids the fragility associated with forecast-driven approaches. Through both these contributions, **research gap 4** is addressed. A comparative evaluation is conducted between the proposed ComEMS4Build, a RBC that represents a simplified, low-input strategy, and a MPC that requires extensive model knowledge and forecasting inputs. This comparison examines both performance and implementation requirements, providing a holistic assessment of the trade-offs among the three control approaches.

The analysis demonstrates that the building, when operated with the aforementioned distributed energy resources, successfully shifts its grid electricity purchases to periods with low price signals, while the hybrid energy storage system compensates during periods of unfavorable grid conditions. In terms of overall performance and functional attributes, the ComEMS4Build consistently positions itself between the RBC and the MPC, assuming equal weighting of all performance indicators and controller features. However, if some features are more prioritized, for example, the model- and forecast-free requirements, MPC would be ranked lower, while the other two would be ranked higher.

6 Conclusions and outlook

Reducing global warming requires primarily decreasing carbon dioxide emissions. The green energy transition emerges as a viable solution for decarbonization, which is essential for addressing climate change. In terms of energy production, the shift is from fossil fuels to renewable energy generation. Integrating renewable energy poses a challenge for ensuring a secure supply. As renewable energy is highly dependent on the weather, generation cannot always meet demand. Thus, it is necessary to unlock demand-side flexibility to achieve alignment between generation and consumption.

Given that the building sector accounts for a substantial share of global energy consumption, electrifying building loads and unlocking energy flexibility can contribute to the green energy transition. The management of energy use in buildings requires advanced control strategies that account for external signals, such as weather data and dynamic day-ahead electricity prices. Providing the controller with additional data, models, and forecasts that affect the building's performance increases the potential to achieve optimal behavior aligned with specific performance objectives. However, this usually requires additional equipment and sensors, making the controller more dependent on the provided data. Thus, this dissertation addresses research gaps in the field of building energy modeling and control as presented in Section 1.1. The first part of the thesis examines the impact of uncertainty and model complexity reduction on model accuracy in building energy modeling (see Chapter 3). This is followed by the development and evaluation of fuzzy logic-based control strategies for building demand response (see Chapters 4 and 5). The main motivation for the chosen control strategy is its independence from models and forecasting profiles.

6.1 Conclusions

Thermal building models simulate the indoor air temperature dynamics depending on external conditions and building properties. These models are fundamental for developing, testing, and evaluating new control strategies. One of the greatest uncertainties in the accuracy of the thermal building model stems from occupant behavior. This raises the following research questions:

Research question 1: What impact does the occupant behavior, defined as the interaction of the occupants with energy control systems and building components (windows, lighting, and related components) and the heat emitted by the occupants, have on the thermal building model forecasts? How can the accuracy of the indoor air temperature forecast be improved?

Section 3.1 analyzes the impact of occupant behavior and introduces a novel approach for gray-box thermal building models, designed to enhance robustness against occupant-related heat loads. To address variability in occupancy patterns and their influence on indoor temperature, this dissertation proposes an ensemble model that distinguishes between weekday and weekend occupancy patterns. This strategy delivers significantly improved forecasts over five validation weeks with minimal additional effort compared to the classic model identification approach.

Motivated by the advantages and widespread applications of simplified models, such as the aforementioned thermal building model, this thesis analyzes the impact of model reduction on complex white-box building energy models, posing the following question:

Research question 2: How does model order reduction influence the dynamic behavior of the multi-physics building heating system model validated on a real-world facility?

The impact of complexity reduction on the dynamics of residential heating systems using the Modelica language and the open-source AixLib library is examined in Section 3.2. A detailed reference model of a building heating system is first developed and validated. Subsequently, complexity is reduced through neglecting and simplifying heating system components. Despite the reference model being parameterized with high-level details, it does not necessarily result in better alignment with the actual facility. The most simplified model achieves significant savings in central processing unit time, with a slight improvement in power-consumption accuracy.

While previous research questions focused on energy building modeling, the remaining research questions concentrate on developing forecast- and model-free control algorithms based on fuzzy logic to enhance building energy flexibility and enable demand response in buildings.

Research question 3: How can fuzzy logic control be designed to exploit building thermal flexibility for demand response programs utilizing thermal building mass in simulation and real-world applications?

To address this, two fuzzy control strategies, each focusing on a different objective, are compared and analyzed in the simulation-based environment (see Section 4.1). One fuzzy logic controller focuses on occupants' thermal comfort, while another focuses on the heat pump's operation costs. None of the developed controllers can shift the load or reduce the peak load when high-peak electricity price signals occur in unfavorable grid conditions. However, additional inputs, such as future occupancy or day-ahead electricity price signals, have the potential to enhance performance.

Thus, the improved strategy is presented in Section 4.2, where the room-individual fuzzy logic controller is investigated in a real-world experimental setup with underfloor heating connected to the district heating network. The results show that the developed fuzzy logic controller unlocks the energy flexibility and reduces the energy costs compared to the considered baseline control strategy.

To further improve the building's flexibility, the case study is enriched with distributed energy resources, which, in addition to the building's thermal mass, include photovoltaics, a battery energy storage system, a hydrogen storage, a fuel cell, and domestic hot water storage. Distributed energy resources help mitigate peak electricity demand and can positively affect the security of supply. The battery energy storage system enables the energy shift from daily to weekly timescales. However, seasonal energy shifting demands storage solutions with high energy density and a low leakage rate. Thus, hydrogen comes into play, fulfilling the long-term storage requirements. Given the variety of energy resources in the building setup, the following research question arises:

Research question 4: How can the coupling of a heat pump and a hydrogen fuel cell contribute to the demand response in buildings with distributed energy resources comprising photovoltaics and electrical, thermal, and hydrogen energy storage systems?

Since the performance of the present building setup highly depends on how the energy systems are managed, this research question is intertwined with the research question concerning the development of a forecast- and model-free control strategy for a building with distributed energy resources:

Research question 5: How can a fuzzy logic controller be implemented as a forecast- and model-free energy management system for residential buildings with distributed energy resources, as listed in research question 4?

A novel energy management system, Comfort-Oriented Energy Management System for Residential Buildings (ComEMS4Build), is developed and evaluated on the residential building with distributed energy resources in Section 5.1. The fuzzy logic-based control strategy is enhanced to manage thermal energy storage, the battery energy storage system, the hydrogen storage system, and photovoltaics generation, where the coupling of the heat pump and fuel cell is investigated. The proposed energy management system is compared with the model predictive controller, the optimal benchmark, and a rule-based controller developed based on ComEMS4Build as a simplified version with minimal input requirements. ComEMS4Build improves storage and thermal mass management in buildings, occupants' comfort, and energy and cost exchange with the grid compared to the rule-based control algorithm, while maintaining lower input requirements than the model-predictive control strategy.

6.2 Outlook

By answering the research questions, listed in Section 1.2, this dissertation addresses the challenges of energy transition in the building sector. However, addressing the research gaps also identifies potential improvements in the proposed methodologies, highlighting avenues for further development. From a building energy modeling perspective, the methodologies can be further analyzed and validated using new data and different conditions. The gray-box thermal building ensemble model can further be evaluated across heating and cooling seasons and explored for year-round ensemble configurations using minimal model sets (e.g., seasonal or vacation-specific modes). Investigating various reduced-order gray-box structures for periods when occupancy patterns vary may further improve prediction accuracy. Considering the white-box heating model reduction, the following avenues are recognized: (i) detailed circulation pumps parameterization for accuracy improvement, (ii) integration of new strategies to mitigate temporal shift for real-time applications, and (iii) further analysis of complexity–CPU time interplay.

From a control perspective, Section 4.1 evaluates a fuzzy logic for thermal building control, providing an overview and suggestions for improvements that are later on implemented in a real-world experiment Section 4.2. The wider the indoor air temperature range is, the more flexibility and load shifting can be achieved. Thus, the optimal ranges of indoor air temperature and its rate of change that do not violate occupant thermal comfort should be further investigated and evaluated. Moreover, incorporating the absolute dynamic price signals, as well as the absolute range of day-ahead prices, may further support the controller by providing absolute, rather than purely relative, indications of grid conditions. In this way, no additional physical signal is introduced to the controller. Rather, the existing signal better describes the grid conditions.

Considering fuzzy logic for an energy management system of buildings with distributed energy resources, the proposed setup should be further developed and evaluated for the German summer period, since the current research assumes green hydrogen production during that season. As investment costs for hydrogen systems remain high, the optimal scale (building, building cluster, or district level) should be further investigated to determine which could be economically beneficial. In general, when developing fuzzy logic algorithms, automatic rule generation and rule base size reduction, while preserving the most important properties, require development and investigation, as the number of comprehensive rule sets grows exponentially with the addition of new inputs.

Appendix

A Fundamentals: Fuzzy logic example

Figure A.1 gives an example of the simple FLC reasoning with two inputs, temperature T and solar radiation $\dot{q}$ and one output heat pump control signal α_{HP}. Suppose that in a time step k the indoor air temperature is $T_k = 20\,°\mathrm{C}$ and $\dot{q}_k = 50\,\mathrm{W/m^2}$. The following rules will be activated based on the values of input variables:

1. IF temperature is “comfortable” AND solar radiation is “small” THEN heat pump control signal is “positive”.
2. IF temperature is “comfortable” AND solar radiation is “average” THEN heat pump control signal is “zero”.
3. IF temperature is “cold” AND solar radiation is “small” THEN heat pump control signal is “positive”.
4. IF temperature is “cold” AND solar radiation is “average” THEN heat pump control signal is “positive”.

As the two inputs are combined with an AND operator in all four rules, the minimum function is utilized to integrate the antecedent part of the corresponding rule (see Table 2.1). For deriving the fuzzy conclusion, the Mamdani implication is chosen, which is characterized by clipping the corresponding output membership function to the $\min(\mu_{\mathrm{A}}(T_k), \mu_{\mathrm{B}}(\dot{q}_k))$. All the fuzzy conclusions from individual activated fuzzy rules are aggregated. They are shown in the Figure A.1 in gray areas. To obtain crisp output from the fuzzy conclusion surface, a defuzzification method must be applied (see Section 2.2). In this example, the lower maximum method is chosen.

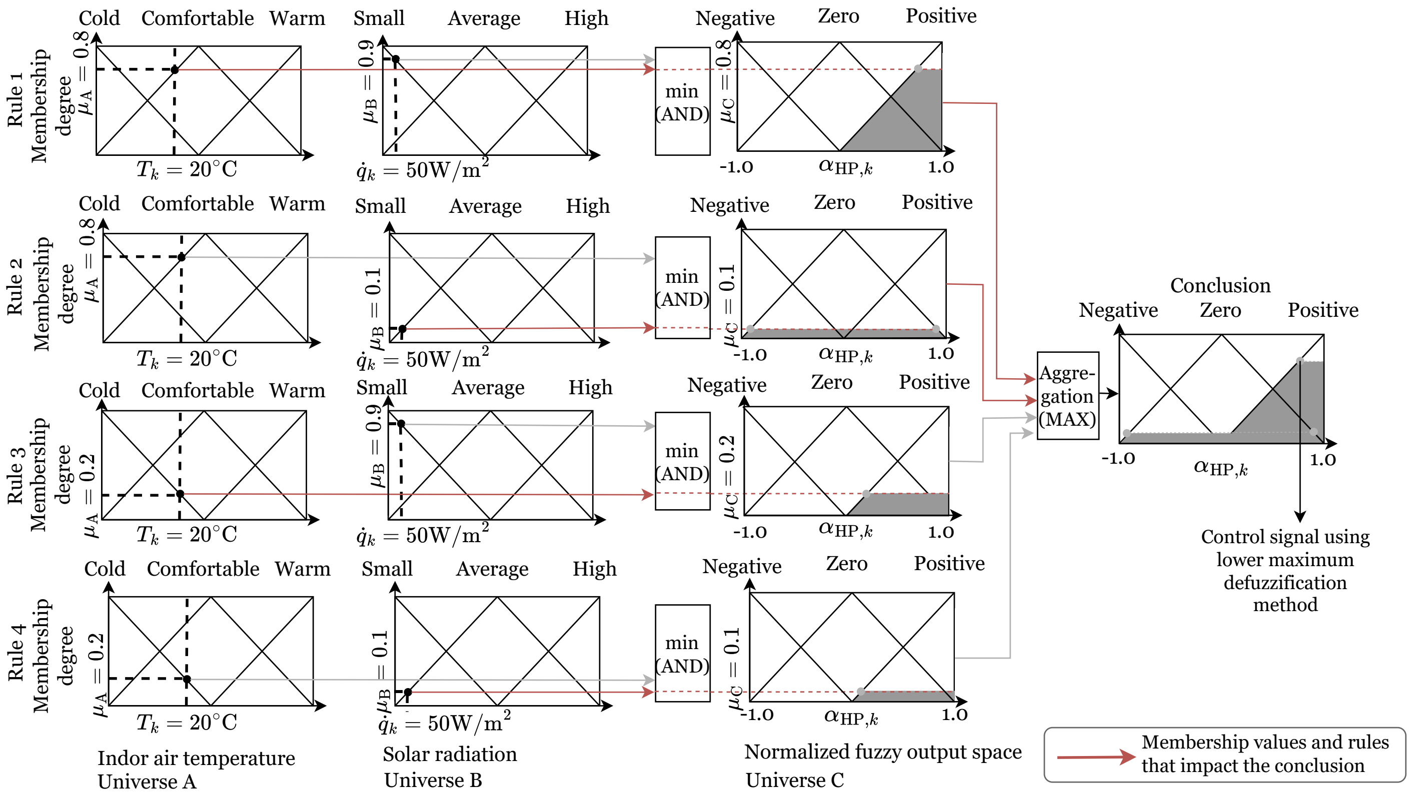

Figure A.1: Fuzzy reasoning example with two inputs indoor air temperature T_k and solar radiation $\dot{q}_k$ and one output heat pump power $\alpha_{\mathrm{HP},k}$. The figure is inspired by Altas (2017).

B Building energy modeling

B.1 Integrating occupant patterns into reduced-order building models to improve forecasting accuracy

To quantify histogram similarity, a Euclidean-norm metric is introduced and visualized as a heatmap in Figure B.1. The resulting distance matrix is symmetric by construction and omits self-comparisons. In general, histograms belonging to the same model category, either ensemble models (EM_i, EM_j) or classical models (CM_i, CM_j), demonstrate strong mutual resemblance, whereas comparisons across categories (EM_i, CM_j) yield the largest deviations.

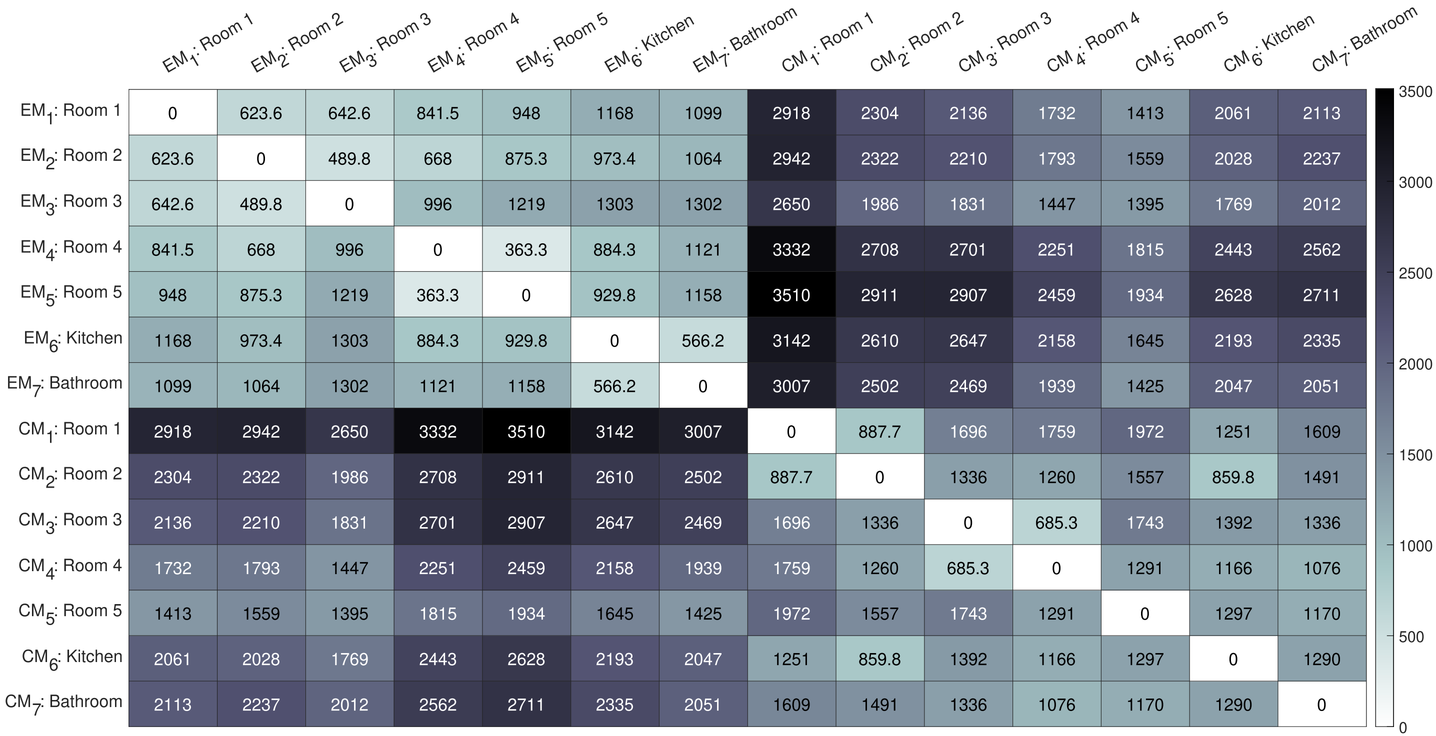

Figure B.1: Heatmap showing the similarity indices of two models across all zones. Abbreviations: EM - ensemble model; CM - classic model. The figure is from Kovačević et al. (2024a).

C Heating flexibility in buildings

C.1 Comfort- and economic-oriented thermal building control: FLCs design

Tables C.1 and C.2 present the rule bases of two FLC controllers, namely the comfort- and the economic-oriented controller. The comfort-oriented controller is designed to prioritize occupants' thermal comfort by focusing primarily on the indoor air temperature error $e_{\mathrm{com},k}$ and its rate of change $\Delta e_{\mathrm{com},k}$ at time step k. In contrast, the economic-oriented controller places greater emphasis on external dynamic signals, specifically the dynamic electricity price $p_{\mathrm{buy},k}$ and the dynamic COP_k.

The eleventh rule of comfort-oriented controller in Table C.1 and 67-73 rules in Table C.2 illustrate how the controllers behave differently under varying COP and p_{buy} conditions. When the indoor air temperature error $e_{\mathrm{com},k} = e_{\mathrm{eco},k}$ is "small cold", the rate of change of the temperature error $\Delta e_{\mathrm{com},k} = \Delta e_{\mathrm{eco},k}$ is "slower warmer", no matter how the external signals $p_{\mathrm{buy},k}$ and COP_k are the comfort-oriented controller will increase the control signal for small increment, i.e. for "small positive". When it comes to the economic-oriented controller, it chooses between no change, i.e. "zero" and a small increment, i.e. "small positive" based on the COP_k efficiency of the heat pump and dynamic electricity prices $p_{\mathrm{buy},k}$.

Table C.1: Rule base table for comfort-oriented FLC controller. Abbreviations: Z – zero; SP – small positive; MP – medium positive; BP – big positive; SN – small negative; MN – medium negative; BN – big negative. The term "all" means for all membership functions of corresponding value. Table is derived from Kovačević et al. (2024b).

Rule	$e_{\mathrm{com},k}$	$\Delta e_{\mathrm{com},k}$	p_{buy}	COP	α_{com}
1	zero	zero	all	all	Z
2	zero	slower colder	all	all	SP
3	zero	faster colder	low	all	BP
4	zero	faster colder	average	low	MP
5	zero	faster colder	average	average	MP
6	zero	faster colder	average	optimal	BP
7	zero	faster colder	high	low	MP
8	zero	faster colder	high	average	MP
9	zero	faster colder	high	optimal	BP
10	small cold	faster warmer	all	all	SP

Rule	$e_{\mathrm{com},k}$	$\Delta e_{\mathrm{com},k}$	p_{buy}	COP	α_{com}
11	small cold	slower warmer	all	all	SP
12	small cold	zero	all	all	SP
13	small cold	slower colder	all	low	SP
14	small cold	slower colder	all	optimal	MP
15	small cold	slower colder	low	average	MP
16	small cold	slower colder	average	average	MP
17	small cold	slower colder	high	average	SP
18	small cold	faster colder	high	all	MP
19	small cold	faster colder	low	low	MP
20	small cold	faster colder	low	average	MP
21	small cold	faster colder	low	optimal	BP
22	small cold	faster colder	average	low	MP
23	small cold	faster colder	average	average	MP
24	small cold	faster colder	average	optimal	BP
25	very cold	faster warmer	all	optimal	BP
26	very cold	faster warmer	all	low	MP
27	very cold	faster warmer	low	average	BP
28	very cold	faster warmer	average	average	MP
29	very cold	faster warmer	high	average	MP
30	very cold	slower warmer	all	low	MP
31	very cold	slower warmer	all	optimal	BP
32	very cold	slower warmer	low	average	BP
33	very cold	slower warmer	average	average	BP
34	very cold	slower warmer	high	average	MP
35	very cold	zero	all	optimal	BP
36	very cold	zero	all	average	BP
37	very cold	zero	all	low	MP
38	very cold	slower colder	all	all	BP
39	very cold	faster colder	all	all	BP
40	zero	slower warmer	all	all	SN
41	zero	faster warmer	all	all	MN

Rule	$e_{\text{com},k}$	$\Delta e_{\text{com},k}$	p_{buy}	COP	α_{com}
42	small warm	faster colder	all	all	SN
43	small warm	slower colder	all	all	SN
44	small warm	zero	all	all	SN
45	small warm	slower warmer	all	all	MN
46	small warm	faster warmer	all	all	MN
47	very warm	faster colder	all	all	MN
48	very warm	slower colder	all	all	MN
49	very warm	zero	all	all	BN
50	very warm	slower warmer	all	all	BN
51	very warm	faster warmer	all	all	BN

Table C.2: Rule base table for economic-oriented FLC controller. Abbreviations: Z – zero; SP – small positive; MP – medium positive; BP – big positive; SN – small negative; MN – medium negative; BN – big negative. The term “all” means for all membership functions of corresponding value. Table is derived from Kovačević et al. (2024b).

Rule	$e_{\text{eco},k}$	$\Delta e_{\text{eco},k}$	p_{buy}	COP	α_{eco}
1	zero	slower warmer	low	all	SN
2	zero	slower warmer	average	low	MN
3	zero	slower warmer	average	average	SN
4	zero	slower warmer	average	optimal	SN
5	zero	slower warmer	high	low	MN
6	zero	slower warmer	high	average	MN
7	zero	slower warmer	high	optimal	SN
8	zero	faster warmer	low	low	BN
9	zero	faster warmer	low	average	MN
10	zero	faster warmer	low	optimal	MN
11	zero	faster warmer	average	low	BN
12	zero	faster warmer	average	average	BN
13	zero	faster warmer	average	optimal	MN
14	zero	faster warmer	high	all	BN
15	small warm	faster colder	low	all	SN

Rule	$e_{\mathrm{eco},k}$	$\Delta e_{\mathrm{eco},k}$	p_{buy}	COP	α_{eco}
16	small warm	faster colder	average	low	SN
17	small warm	faster colder	average	average	SN
18	small warm	faster colder	average	optimal	MN
19	small warm	faster colder	high	all	MN
20	small warm	slower colder	low	low	MN
21	small warm	slower colder	low	average	SN
22	small warm	slower colder	low	optimal	SN
23	small warm	slower colder	average	low	MN
24	small warm	slower colder	average	average	MN
25	small warm	slower colder	average	optimal	SN
26	small warm	slower colder	high	all	MN
27	small warm	zero	average	all	MN
28	small warm	slower warmer	low	low	BN
29	small warm	slower warmer	low	average	MN
30	small warm	slower warmer	low	optimal	MN
31	small warm	slower warmer	average	low	BN
32	small warm	slower warmer	average	average	BN
33	small warm	slower warmer	average	optimal	MN
34	small warm	slower warmer	high	all	BN
35	small warm	faster warmer	all	all	BN
36	very warm	faster colder	all	all	BN
37	very warm	slower colder	all	all	BN
38	very warm	zero	all	all	BN
39	very warm	slower warmer	all	all	BN
40	very warm	faster warmer	all	all	BN
41	small warm	zero	low	all	MN
42	small warm	zero	high	low	BN
43	small warm	zero	high	average	BN
44	small warm	zero	high	optimal	MN
45	zero	zero	low	all	Z
46	zero	zero	average	low	SN

Rule	$e_{\mathrm{eco},k}$	$\Delta e_{\mathrm{eco},k}$	p_{buy}	COP	α_{eco}
47	zero	zero	average	average	Z
48	zero	zero	average	optimal	Z
49	zero	zero	high	low	MN
50	zero	zero	high	average	SN
51	zero	zero	high	optimal	SN
52	zero	slower colder	all	all	Z
53	zero	faster colder	low	low	Z
54	zero	faster colder	low	average	SP
55	zero	faster colder	low	optimal	SP
56	zero	faster colder	average	low	Z
57	zero	faster colder	average	average	Z
58	zero	faster colder	average	optimal	SP
59	zero	faster colder	high	all	Z
60	small cold	faster warmer	low	all	Z
61	small cold	faster warmer	average	low	SN
62	small cold	faster warmer	average	average	Z
63	small cold	faster warmer	average	optimal	Z
64	small cold	faster warmer	high	low	SN
65	small cold	faster warmer	high	average	SN
66	small cold	faster warmer	high	optimal	Z
67	small cold	slower warmer	low	low	Z
68	small cold	slower warmer	low	average	SP
69	small cold	slower warmer	low	optimal	SP
70	small cold	slower warmer	average	low	Z
71	small cold	slower warmer	average	average	Z
72	small cold	slower warmer	average	optimal	SP
73	small cold	slower warmer	high	all	Z
74	small cold	zero	low	all	SP
75	small cold	zero	average	low	Z
76	small cold	zero	average	average	SP
77	small cold	zero	average	optimal	SP

Rule	$e_{\mathrm{eco},k}$	$\Delta e_{\mathrm{eco},k}$	p_{buy}	COP	α_{eco}
78	small cold	zero	high	low	SN
79	small cold	zero	high	average	SN
80	small cold	zero	high	optimal	SP
81	small cold	slower colder	low	all	SP
82	small cold	slower colder	average	low	Z
83	small cold	slower colder	average	average	SP
84	small cold	slower colder	average	optimal	SP
85	small cold	slower colder	high	low	Z
86	small cold	slower colder	high	average	Z
87	small cold	slower colder	high	optimal	SP
88	small cold	faster colder	low	low	SP
89	small cold	faster colder	low	average	SP
90	small cold	faster colder	low	optimal	MP
91	small cold	faster colder	average	all	SP
92	small cold	faster colder	high	low	Z
93	small cold	faster colder	high	average	Z
94	small cold	faster colder	high	optimal	SP
95	very cold	faster warmer	all	all	Z
96	very cold	slower warmer	low	low	SP
97	very cold	slower warmer	low	average	SP
98	very cold	slower warmer	low	optimal	MP
99	very cold	slower warmer	average	all	SP
100	very cold	slower warmer	high	low	Z
101	very cold	slower warmer	high	average	Z
102	very cold	slower warmer	high	optimal	SP
103	very cold	zero	low	low	SP
104	very cold	zero	low	average	MP
105	very cold	zero	low	optimal	MP
106	very cold	zero	average	low	SP
107	very cold	zero	average	average	SP
108	very cold	zero	average	optimal	MP

Rule	$e_{\mathrm{eco},k}$	$\Delta e_{\mathrm{eco},k}$	p_{buy}	COP	α_{eco}
109	very cold	zero	high	all	SP
110	very cold	slower colder	low	low	MP
111	very cold	slower colder	low	average	BP
112	very cold	slower colder	low	optimal	BP
113	very cold	slower colder	average	all	MP
114	very cold	slower colder	high	all	SP
115	very cold	faster colder	low	all	BP
116	very cold	faster colder	average	low	MP
117	very cold	faster colder	average	average	MP
118	very cold	faster colder	average	optimal	BP
119	very cold	faster colder	high	low	SP
120	very cold	faster colder	high	average	SP
121	very cold	faster colder	high	optimal	MP

C.2 Experiment: Real-world evaluation of the fuzzy logic control for demand response in buildings

Tables C.3 and C.4 show the FLC rule bases developed for the experimental setup under two different lower temperature constraints.

Table C.3: Rule base table for experimental setup for case when the $T_{\mathrm{min}} = 21\,^{\circ}\mathrm{C}$. Abbreviations stand for: SP – small positive, MP – medium positive, BP – big positive, LB – lower constraint. Table is derived from Langner and Kovačević et al. (2025).

Rule	e_j	Δo_j	$\Delta T_{\mathrm{air},j}$	$\hat{F}(p_{\mathrm{buy}})$	$T_{\mathrm{air,ref,j}}$	$\alpha_{\mathrm{s,j}}$
1	zero	zero	zero	low	T_{SP}	SP
2	zero	zero	zero	average	T_{LC}	zero
3	zero	zero	zero	high	T_{LC}	zero
4	zero	zero	colder	low	T_{BP}	BP
5	zero	zero	colder	average	T_{MP}	MP
6	zero	zero	colder	high	T_{LC}	SP
7	zero	zero	warmer	all	T_{LC}	zero

Rule	e_j	Δo_j	$\Delta T_{\text{air},j}$	$\hat{F}(p_{\text{buy}})$	$T_{\text{air,ref,j}}$	$\alpha_{\text{s,j}}$
8	zero	warmer	all	low	T_{MP}	MP
9	zero	warmer	all	average	T_{SP}	SP
10	zero	warmer	all	high	T_{LC}	zero
11	zero	colder	zero	all	T_{LC}	zero
12	zero	colder	warmer	all	T_{LC}	zero
13	zero	colder	colder	low	T_{BP}	BP
14	zero	colder	colder	average	T_{MP}	MP
15	zero	colder	colder	high	T_{LC}	SP
16	warm	all	all	all	T_{LC}	zero
17	hot	all	all	all	T_{LC}	zero
18	cold	all	all	all	T_{LC}	BP

Table C.4: Rule base table for experimental setup for case when the $T_{\min} = 18\,°\text{C}$. Abbreviations stand for: SP – small positive, MP – medium positive, BP – big positive, LB – lower constraint. Table is derived from Langner and Kovačević et al. (2025).

Rule	$e_{j,k}$	$\Delta o_{j,k}$	$\Delta T_{\text{air}j,k}$	$\hat{F}(p_{\text{buy}})_k$	$T_{\text{air,ref,j,k+1}}$	$\alpha_{\text{s,j,k+1}}$
1	all	zero	all	all	T_{off}	zero
2	all	colder	all	all	T_{off}	zero
3	cold	warmer	all	all	T_{LC}	BP
4	zero	warmer	zero	low	T_{SP}	SP
5	zero	warmer	zero	average	T_{LC}	zero
6	zero	warmer	zero	high	T_{LC}	zero
7	zero	warmer	colder	low	T_{MP}	BP
8	zero	warmer	colder	average	T_{SP}	MP
9	zero	warmer	colder	high	T_{LC}	SP
10	zero	warmer	warmer	all	T_{LC}	zero
11	warm	warmer	all	low	T_{SP}	SP
12	warm	warmer	all	average	T_{LC}	zero
13	warm	warmer	all	high	T_{LC}	zero
14	hot	warmer	all	low	T_{SP}	SP
15	hot	warmer	all	average	T_{LC}	zero

Rule	$e_{j,k}$	$\Delta o_{j,k}$	$\Delta T_{\text{air}j,k}$	$\hat{F}(p_{\text{buy}})_k$	$T_{\text{air,ref,j,k+1}}$	$\alpha_{\text{s,j,k+1}}$
16	hot	warmer	all	high	T_{LC}	zero

Figure C.1 presents the controller comparison on Feb 16, 2025, during experiment 3. The figure illustrates indoor air temperatures in the heated rooms, total heat demand, and heating price signals of both buildings.

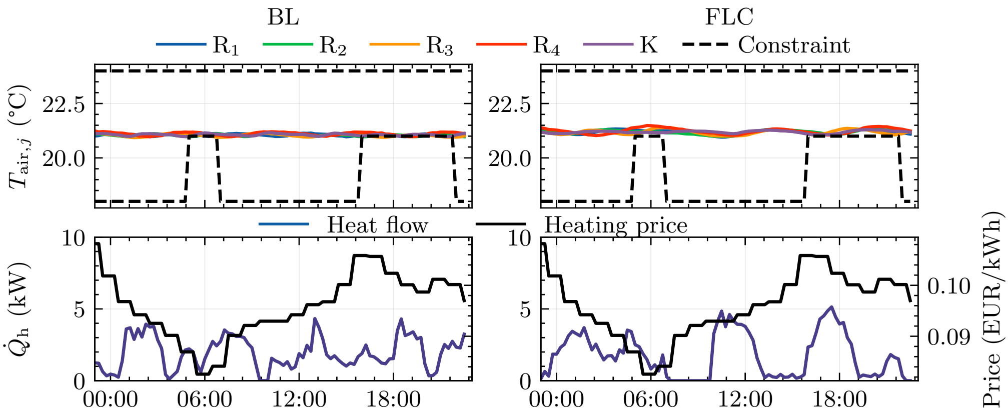

Figure C.1: Indoor air temperature of the rooms, corresponding heat flows, and heating price on Feb. 16, 2025, during experiment 3.

D Fuzzy logic energy management system

D.1 Comfort-oriented energy management using hydrogen seasonal storage

Tables D.1, D.2 and D.3 show the rule bases for the FLC_{flex}, FLC_{FC} and FLC_{BESS}, respectively. Concretely, FLC_{flex} defines the magnitude of the modulation factor η_{HP} based on increment or decrement α_{HP}. For example, if the LOH and SOC are indicating “empty” storage systems and the electricity price signal is relatively “low” at time step k, the increment α_{HP} will be “big positive”, as the purchasing from the grid is favorable (see rule 1 in Table D.1). On the other hand, when the electricity price signal is “average” or “high”, compared to the day-ahead price signals, the magnitude of increment α_{HP} will also depend on current solar radiation $\dot{q}_{\text{sol}}$ (see rules 2–7 in Table D.1).

Table D.1: Rule base table for FLC_{flex}. The abbreviations stand for: SN – small negative, MN – medium negative, BN – big negative, SP – small positive, MP – medium positive, and BP – big positive. The term "all" means for all membership functions of the corresponding set. The table is derived from Kovačević et al. (2025b).

Rule	$\min(\chi_{\text{SH}}, \chi_{\text{DHW}})$	LOH	SOC	$\hat{F}(p_{\text{buy}})$	$\dot{q}_{\text{sol}}$	α_{HP}
1	low	empty	empty	low	all	BP
2	low	empty	empty	average	low	SP
3	low	empty	empty	average	average	MP
4	low	empty	empty	average	high	BP
5	low	empty	empty	high	low	zero
6	low	empty	empty	high	average	SP
7	low	empty	empty	high	high	BP
8	low	empty	average	low	all	BP
9	low	empty	average	average	low	MP
10	low	empty	average	average	average	BP
10	low	empty	average	average	high	BP
11	low	empty	average	high	low	SP
12	low	empty	average	high	average	MP
13	low	empty	average	high	high	BP
14	low	empty	full	all	all	MP
15	low	average	empty	low	all	BP
16	low	average	empty	average	low	MP
17	low	average	empty	average	average	BP
18	low	average	empty	average	high	BP
19	low	average	empty	high	low	SP
20	low	average	empty	high	average	MP
21	low	average	empty	high	high	BP
22	low	average	average	low	all	BP
23	low	average	average	average	low	MP
24	low	average	average	average	average	BP
24	low	average	average	average	high	BP
25	low	average	average	high	low	MP
26	low	average	average	high	average	BP

Rule	$\min(\chi_{\mathrm{SH}}, \chi_{\mathrm{DHW}})$	LOH	SOC	$\hat{F}(p_{\mathrm{buy}})$	$\dot{q}_{\mathrm{sol}}$	α_{HP}
26	low	average	average	high	high	BP
27	low	average	full	all	all	MP
28	low	full	empty	low	all	BP
29	low	full	empty	average	low	MP
30	low	full	empty	average	average	BP
30	low	full	empty	average	high	BP
31	low	full	empty	high	low	MP
32	low	full	empty	high	average	MP
33	low	full	empty	high	high	BP
34	low	full	average	low	all	BP
35	low	full	average	average	low	MP
36	low	full	average	average	average	BP
36	low	full	average	average	high	BP
37	low	full	average	high	low	SP
38	low	full	average	high	average	BP
38	low	full	average	high	high	BP
39	low	full	full	all	all	BP
40	average	empty	empty	low	low	SP
41	average	empty	empty	low	average	MP
42	average	empty	empty	low	high	MP
43	average	empty	empty	average	low	BN
44	average	empty	empty	average	average	SP
45	average	empty	empty	average	high	SP
46	average	empty	empty	high	low	BN
47	average	empty	empty	high	average	zero
48	average	empty	empty	high	high	SP
49	average	empty	average	low	low	SP
50	average	empty	average	low	average	MP
51	average	empty	average	low	high	BP
52	average	empty	average	average	low	zero
53	average	empty	average	average	average	MP

Rule	$\min(\chi_{\mathrm{SH}}, \chi_{\mathrm{DHW}})$	LOH	SOC	$\hat{F}(p_{\mathrm{buy}})$	$\dot{q}_{\mathrm{sol}}$	α_{HP}
54	average	empty	average	average	high	BP
55	average	empty	average	high	low	zero
56	average	empty	average	high	average	MP
57	average	empty	average	high	high	BP
58	average	empty	full	low	low	SP
59	average	empty	full	low	average	MP
60	average	empty	full	low	high	BP
61	average	empty	full	average	low	SP
62	average	empty	full	average	average	MP
63	average	empty	full	average	high	BP
64	average	empty	full	high	low	SP
65	average	empty	full	high	average	MP
66	average	empty	full	high	high	BP
67	average	average	empty	low	low	MP
68	average	average	empty	low	average	MP
69	average	average	empty	low	high	BP
70	average	average	empty	average	low	zero
71	average	average	empty	average	average	zero
72	average	average	empty	average	high	SP
73	average	average	empty	high	low	SN
74	average	average	empty	high	average	zero
75	average	average	empty	high	high	SP
76	average	average	average	low	low	SP
77	average	average	average	low	average	MP
78	average	average	average	low	high	BP
79	average	average	average	average	low	zero
80	average	average	average	average	average	SP
81	average	average	average	average	high	MP
82	average	average	average	high	low	SP
83	average	average	average	high	average	SP
84	average	average	average	high	high	MP

Rule	$\min(\chi_{\mathrm{SH}}, \chi_{\mathrm{DHW}})$	LOH	SOC	$\hat{F}(p_{\mathrm{buy}})$	$\dot{q}_{\mathrm{sol}}$	α_{HP}
85	average	average	full	low	low	SP
86	average	average	full	low	average	MP
87	average	average	full	low	high	BP
88	average	average	full	average	low	zero
89	average	average	full	average	average	SP
90	average	average	full	average	high	MP
91	average	average	full	high	low	zero
92	average	average	full	high	average	SP
93	average	average	full	high	high	MP
94	average	full	empty	low	low	zero
95	average	full	empty	low	average	SP
96	average	full	empty	low	high	MP
97	average	full	empty	average	low	zero
98	average	full	empty	average	average	SP
99	average	full	empty	average	high	MP
100	average	full	empty	high	low	zero
101	average	full	empty	high	average	zero
102	average	full	empty	high	high	SP
103	average	full	average	low	low	SP
104	average	full	average	low	average	MP
105	average	full	average	low	high	BP
106	average	full	average	average	low	SP
107	average	full	average	average	average	MP
108	average	full	average	average	high	MP
109	average	full	average	high	low	SP
110	average	full	average	high	average	SP
111	average	full	average	high	high	MP
112	average	full	full	low	low	SP
113	average	full	full	low	average	MP
114	average	full	full	low	high	BP
115	average	full	full	average	low	SP

Rule	$\min(\chi_{\mathrm{SH}}, \chi_{\mathrm{DHW}})$	LOH	SOC	$\hat{F}(p_{\mathrm{buy}})$	$\dot{q}_{\mathrm{sol}}$	α_{HP}
116	average	full	full	average	average	MP
117	average	full	full	average	high	BP
118	average	full	full	high	low	SP
119	average	full	full	high	average	SP
120	average	full	full	high	high	MP
121	high	empty	empty	all	all	BN
122	high	empty	average	low	low	SN
123	high	empty	average	low	average	zero
124	high	empty	average	low	high	SP
125	high	empty	average	average	low	MN
126	high	empty	average	average	average	zero
127	high	empty	average	average	high	SP
128	high	empty	average	high	low	BN
129	high	empty	average	high	average	zero
130	high	empty	average	high	high	SP
131	high	empty	full	low	low	SN
132	high	empty	full	low	average	zero
133	high	empty	full	low	high	SP
134	high	empty	full	average	low	SN
134	high	empty	full	high	low	SN
135	high	empty	full	average	average	zero
135	high	empty	full	high	average	zero
136	high	empty	full	average	high	SP
136	high	empty	full	high	high	SP
137	high	average	empty	all	all	BN
138	high	average	average	low	low	SN
139	high	average	average	low	average	SP
140	high	average	average	low	high	MP
141	high	average	average	average	low	BN
141	high	average	average	high	low	BN
142	high	average	average	average	average	SP

Rule	$\min(\chi_{\mathrm{SH}}, \chi_{\mathrm{DHW}})$	LOH	SOC	$\hat{F}(p_{\mathrm{buy}})$	$\dot{q}_{\mathrm{sol}}$	α_{HP}
142	high	average	average	high	average	SP
143	high	average	average	average	high	MP
143	high	average	average	high	high	MP
144	high	average	full	low	low	SN
145	high	average	full	low	average	SP
146	high	average	full	low	high	MP
147	high	average	full	average	low	BN
147	high	average	full	high	low	BN
148	high	average	full	average	average	SP
148	high	average	full	high	average	SP
149	high	average	full	average	high	MP
149	high	average	full	high	high	MP
150	high	full	empty	all	all	BN
151	high	full	average	all	all	BN
152	high	full	full	low	all	MN
153	high	full	full	average	all	BN
154	high	full	full	high	all	BN

The controller $\mathrm{FLC}_{\mathrm{FC}}$ determines the control signal α_{FC}, where rule base is defined in Table D.2. In addition to the current HESS state and the load magnitude, the behavior of the fuel cell is influenced by the ECDF of the electricity price signal as well as by the fuel cell's previous operation state. When the load is categorized as "small negative", the allowable daily hydrogen consumption $\Delta\mathrm{LOH}$ is defined as "full", and the SOC indicates an "empty" level, the resulting value of α_{FC} depends on the former toggling state for the ECDF price signal "average" (see rules 16–17 in Table D.2). However, if the ECDF price signal is classified as "high", the control signal α_{FC} will be set to "medium positive" regardless of the prior switching state (see rule 18 in Table D.2). As the electricity price signal is relatively high, this rule will trigger the fuel cell to meet the demand.

Table D.2: Rule base table for $\mathrm{FLC}_{\mathrm{FC}}$. The abbreviations stand for: SN – small negative, MN – medium negative, BN – big negative, SP – small positive, MP – medium positive, and BP – big positive. The term “all” means for all membership functions of the corresponding set. The table is derived from Kovačević et al. (2025b).

Rule	ΔP	ΔLOH	SOC	$\hat{F}(p_{\mathrm{buy}})$	$s_{\mathrm{on,off}}$	α_{FC}
1	positive	all	all	all	all	off
2	SN	empty	all	all	all	off
3	MN	empty	all	all	all	off
4	BN	empty	all	all	all	off
5	SN	average	empty	low	off	off
6	SN	average	empty	low	on	off
7	SN	average	empty	average	off	off
8	SN	average	empty	average	on	MP
9	SN	average	empty	high	all	MP
10	SN	average	average	all	off	off
11	SN	average	average	all	on	MP
12	SN	average	full	all	off	off
13	SN	average	full	all	on	MP
14	SN	full	empty	low	off	off
15	SN	full	empty	low	on	off
16	SN	full	empty	average	off	off
17	SN	full	empty	average	on	MP
18	SN	full	empty	high	all	MP
19	SN	full	average	all	off	off
20	SN	full	average	all	on	MP
21	SN	full	full	all	off	off
22	SN	full	full	all	on	MP
23	MN	average	empty	low	off	off
24	MN	average	empty	low	on	off
25	MN	average	empty	average	off	BP
26	MN	average	empty	average	on	BP
27	MN	average	empty	high	all	BP
28	MN	average	average	low	off	off

Rule	ΔP	ΔLOH	SOC	$\hat{F}(p_{\text{buy}})$	$s_{\text{on,off}}$	α_{FC}
29	MN	average	average	low	on	off
30	MN	average	average	average	off	off
31	MN	average	average	average	on	BP
32	MN	average	average	high	all	BP
33	MN	average	full	low	off	off
34	MN	average	full	low	on	off
35	MN	average	full	average	off	off
36	MN	average	full	average	on	BP
37	MN	average	full	high	on	BP
38	MN	average	full	high	off	BP
39	MN	full	empty	low	off	off
40	MN	full	empty	low	on	off
41	MN	full	empty	average	on	BP
42	MN	full	empty	average	off	BP
43	MN	full	empty	high	all	BP
44	MN	full	average	low	off	off
45	MN	full	average	low	on	off
46	MN	full	average	average	off	off
47	MN	full	average	average	on	MP
48	MN	full	average	high	all	MP
49	MN	full	full	low	all	off
50	MN	full	full	average	on	MP
51	MN	full	full	high	on	MP
52	MN	full	full	high	off	MP
53	MN	full	full	average	off	off
54	BN	average	empty	low	off	off
55	BN	average	empty	low	on	off
56	BN	average	empty	average	all	BP
57	BN	average	empty	high	all	BP
58	BN	average	average	low	off	off
59	BN	average	average	low	on	off

Rule	ΔP	ΔLOH	SOC	$\hat{F}(p_{\text{buy}})$	$s_{\text{on,off}}$	α_{FC}
60	BN	average	average	average	off	MP
61	BN	average	average	average	on	MP
62	BN	average	average	high	all	BP
63	BN	average	full	low	all	off
64	BN	average	full	average	off	off
65	BN	average	full	average	on	BP
66	BN	average	full	high	on	BP
67	BN	average	full	high	off	BP
68	BN	full	empty	low	off	off
69	BN	full	empty	low	on	off
70	BN	full	empty	average	all	BP
71	BN	full	empty	high	all	BP
72	BN	full	average	low	off	off
73	BN	full	average	low	on	off
74	BN	full	average	average	off	BP
75	BN	full	average	average	on	BP
76	BN	full	average	high	all	BP
77	BN	full	full	low	off	off
78	BN	full	full	low	on	MP
79	BN	full	full	average	all	BP
80	BN	full	full	high	all	BP

Hierarchically, the last controller is FLC$_{\text{BESS}}$, which defines control signal α_{BESS}, based on the residual load (negative) or the residual generation (positive) ΔP_{new}, SOC and ECDF of electricity price signal $\hat{F}(p_{\text{buy}})$. For example, if the ECDF of electricity price signal $\hat{F}(p_{\text{buy}})$ is "low", SOC is "empty" and demand exists ($\Delta P_{\text{new}} \in \{\text{SN}, \text{MN}, \text{BN}\}$), the control signal will be "big positive" (see rules 2–4 in Table D.3). This indicates that the demanded power will be purchased from the grid and the battery will be charged (see Equations (5.35)–(5.36)).

Table D.3: Rule base table for FLC$_{\mathrm{BESS}}$. The abbreviations stand for: SN – small negative, MN – medium negative, BN – big negative, SP – small positive, MP – medium positive, and BP – big positive. The term "all" means for all membership functions of the corresponding set. The table is derived from Kovačević et al. (2025b).

Rule	ΔP_{new}	SOC	$\hat{F}(p_{\mathrm{buy}})$	α_{BESS}
1	zero	all	all	off
2	SN	empty	low	BP
3	MN	empty	low	BP
4	BN	empty	low	BP
5	SN	empty	average	off
6	MN	empty	average	off
7	BN	empty	average	off
8	SN	empty	high	off
9	MN	empty	high	off
10	BN	empty	high	off
11	SN	average	low	MP
12	SN	full	low	off
13	SN	average	average	off
14	SN	average	high	SN
15	SN	full	average	off
16	SN	full	high	MN
17	MN	average	low	off
18	MN	full	low	off
19	MN	average	average	SN
20	MN	average	high	MN
21	MN	full	average	MN
22	MN	full	high	BN
23	BN	average	low	off
24	BN	full	low	off
25	BN	average	average	MN
26	BN	full	average	MN
27	BN	average	high	BN
28	BN	full	high	BN

Rule	ΔP_{new}	SOC	$\hat{F}(p_{\mathrm{buy}})$	α_{BESS}
29	SP	empty	all	BP
30	SP	average	all	BP
31	MP	empty	all	BP
32	MP	average	all	BP
33	BP	empty	all	MP
34	BP	average	all	MP
35	SP	full	all	off
36	MP	full	all	off
37	BP	full	all	off

List of acronyms and symbols

Acronyms

BESS	Battery Energy Storage System
BL	Baseline
B	Bathroom
COP	Coefficient of Performance
CPU	Central Processing Unit
C	Corridor
DAE	Differential-Algebraic System of Equations
DHW	Domestic Hot Water
DoD	Depth of Discharge
ECDF	Empirical Cumulative Distribution Function
EMS	Energy Management System
FLC	Fuzzy Logic Control
HESS	Hybrid Energy Storage System
HP	Heat Pump
HVAC	Heating Ventilation and Air Conditioning
IEA	International Energy Agency
KIT	Karlsruhe Institute of Technology
K	Kitchen
LLEC	Living Lab Energy Campus
LOH	Level of Hydrogen
MAE	Mean Absolute Error
MAPE	Mean Absolute Percentage Error
MPC	Model Predictive Control
OB	Occupants’ Behavior

OTS	Occupants' Thermal Satisfaction
PID	Proportional–Integral–Derivative
PI	Proportional–Integral
PLC	Programmable Logic Controller
PMV	Predicted Mean Vote
PPD	Predicted Percentage Dissatisfied
PV	Photovoltaics
RBC	Rule Based Control
RC	Resistance-Capacitance
RES	Renewable Energy Sources
RL	Reinforcement Learning
RMSE	Root Mean Square Error
RQ	Research Question
R	Room
SH	Space Heating
SOC	State Of Charge

Indices

air	Indoor air temperature
amb	Ambient
ch	Charging
com	Comfort-oriented
cond	Conductive heat transfer
conv	Convective share
d	Discharging
dm	Demand
eco	Economic-oriented
el	Electrical
FC	Fuel cell
flex	Flexible
h	Heating
H_2	Hydrogen

H_2O	Water
HC	Heating curve
hr	Heat recovery
ig	Internal heat gains
in	Investment
inf	Infiltration
l	Standing losses
m	Thermal building mass
om	Operation and maintenance
on/off	Toggling
ref	Reference
s	Supply
SH	Space heating
sol	Solar
STC	Standard test condition
sys	System
th	Thermal
w	Wall

Parameters

β	Scaling factor
Δo	Change in the lower temperature constraint in $^\circ\mathrm{C}$
$\dot{q}$	Radiation in $\mathrm{W/m^2}$
η	Efficiency factor
μ	Membership value
ϕ	Flexibility factor
ρ	Density in $\mathrm{kg/m^3}$
σ	Costs in EUR, $\mathrm{EUR/kWh}$ and $\mathrm{EUR/h}$
ζ	Restriction factor
c	Specific heat capacity $\mathrm{J/kgK}$
d	Discomfort in $\mathrm{K\,h}$
g	Heat gain factor in $\mathrm{m^2}$

H	Horizon time
j	Room
k	Time step
L	Component lifespan in h
N	Number of time step
t_{s}	Sample time in s
$\hat{F}(\cdot)$	Empirical cumulative distribution function
p	Price signal in $\mathrm{EUR/kWh}$
C	Thermal capacitance in $\mathrm{J/K}$
LHV	Lower heating value in $\mathrm{J/kg}$
NOCT	Nominal operating cell temperature in $^{\circ}\mathrm{C}$
R	Thermal resistance in $\mathrm{K/W}$
TOG	Toggling counts
WH	Working hours in h
Variables	
α	Fuzzy control signal
χ	Thermal state relative to constraints
$\dot{n}$	Molar flow in $\mathrm{mol/s}$
E	Energy in kWh
e	Error
P	Power in W
s	Binary variable
$\dot{Q}$	Heat flow in W
T	Temperature in $^{\circ}\mathrm{C}$
V	Volume in m^3

List of figures

List of tables

List of publications

The publications are organized by publication type and, within each category, ordered according to their relevance to this dissertation.

Journal articles

Jovana Kovačević, Felix Langner, Erfan Tajalli-Ardekani, Marvin Dorn, Simon Waczowicz, Ralf Mikut, Jörg Matthes, Hüseyin K. Çakmak, and Veit Hagenmeyer. ComEMS4Build: Comfort-Oriented Energy Management System for Residential Buildings using Hydrogen for Seasonal Storage. *Preprint*, 2025b. doi: 10.48550/arXiv.2511.04293.

Felix Langner, Jovana Kovačević, Luigi Spatafora, Stefan Dietze, Simon Waczowicz, Hüseyin K. Çakmak, Jörg Matthes, and Veit Hagenmeyer. Experimental evaluation of model predictive control and fuzzy logic control for demand response in buildings. *Applied Energy*, 401:126666, 2025. ISSN 0306-2619. doi: 10.1016/j.apenergy.2025.126666.

Felix Langner*, Jovana Kovačević*, Philipp Zwickel, Thomas Dengiz, Moritz Frahm, Simon Waczowicz, Hüseyin K. Çakmak, Jörg Matthes, and Veit Hagenmeyer. Coordinated price-based control of modulating heat pumps for practical demand response and peak shaving in building clusters. *Energy and Buildings*, 324:114940, 2024. doi: 10.1016/j.enbuild.2024.114940.

Xinliang Dai, Alexander Kocher, Jovana Kovačević, Burak Dindar, Yuning Jiang, Colin Jones, Hüseyin K. Çakmak, and Veit Hagenmeyer. Ensuring data privacy in AC optimal power flow with a distributed co-simulation framework. *Electric Power Systems Research*, 235:110710, 2024. doi: 10.1016/j.epsr.2024.110710.

Chang Li, Gina Brecher, Jovana Kovačević, Hüseyin K. Çakmak, Kevin Förderer, Jörg Matthes, and Veit Hagenmeyer. Gossen's first law in the modeling for demand side management: a

*These authors contributed equally to this work.

thorough heat pump case study with deep learning based partial time series data generation. *Energy Informatics*, 7(1):47, 2024. doi: 10.1186/s42162-024-00353-z.

Carsten Hoyer-Klick, Philipp C. Böttcher, Hüseyin K. Çakmak, Manuel Dahmen, Kevin Förderer, Jakob Geiges, Veit Hagenmeyer, Ludwig Hülk, Theresa Klütz, Wolfgang Köppel, Jovana Kovačević, Patrick Kuckertz, Yifei Lu, Wided Medjroubi, Ralf Mikut, Tristan Pelser, Thiemo Pesch, Thorsten Schlachter, Martin Stoffers, Wolfgang Süß, Simon Waczowicz, Jann M. Weinand, Dirk Witthaut, and André Xhonneux. Implementing Open Science in Energy Systems Research - A Community Compendium. *In Preparation*, 2026.

Conference contributions

Jovana Kovačević, Chang Li, Kevin Förderer, Hüseyin K. Çakmak, and Veit Hagenmeyer. Improving Reduced-Order Building Modeling: Integration of Occupant Patterns for Reducing Energy Consumption. In *Proceedings of the 15th ACM International Conference on Future and Sustainable Energy Systems*, pages 569–579, 2024a. doi: 10.1145/3632775.3662163.

Jovana Kovačević, Anne-Christin Süß, Hüseyin K. Çakmak, and Veit Hagenmeyer. A fuzzy logic approach for economic energy-efficient heat pump operation in thermal building control. In *2024 IEEE PES Innovative Smart Grid Technologies Europe (ISGT EUROPE)*, pages 1–6. IEEE, 2024b. doi: 10.1109/ISGTEUROPE62998.2024.10863470.

Jovana Kovačević*, Chang Li*, Gina Brecher, Kevin Förderer, Hüseyin K. Çakmak, and Veit Hagenmeyer. The Impact of Model Complexity Reduction on System Dynamics: A Modelica Case Study of a Residential Heating System. In *2025 IEEE Conference on Technologies for Sustainability (SusTech)*, pages 1–8. IEEE, 2025a. doi: 10.1109/SusTech63138.2025.11025706.

Erfan Tajalli-Ardekani, Haozhen Cheng, Alexander Kocher, Jovana Kovačević, Simon Waczowicz, Hüseyin K. Çakmak, Giovanni Delibra, Alessandro Corsini, and Veit Hagenmeyer. GIS-AWBEM: GIS-based Automated White-Box Building Energy Modeling. In *2026 Open Source Modelling and Simulation of Energy Systems (OSMSES)*, pages 1–6, 2026. doi: 10.1109/OSMSES69376.2026.11457217.

*These authors contributed equally to this work.

Alexander Kocher, Jovana Kovačević, Anne-Christin Süß, Can Berk Saner, Burak Dindar, Md Amimul Ehsan, Hüseyin K. Çakmak, and Veit Hagenmeyer. Privacy protection in collaborative geographically distributed co-simulation of multimodal energy systems. In *Proceedings of the 15th ACM International Conference on Future and Sustainable Energy Systems*, pages 639–647, 2024. doi: 10.1145/3632775.3661990.

Data publications

Erfan Tajalli-Ardekani, Felix Langner, Jovana Kovačević, Stefan Dietze, Malte Holzhäuer, Tobias Moser, Abdulrahman Seddiqi, Luigi Spatafora, Simon Waczowicz, Hüseyin K. Çakmak, Jörg Matthes, and Veit Hagenmeyer. Experimental data of three identical residential buildings controlled with different controllers for heating demand response. 2025. doi: 10.5281/zenodo.17455075.

Publications supporting the dissertation chapters

This dissertation is based on the above-listed publication. This section describes mapping the corresponding chapters with publications that contain identical phrases.

Representative number of the publication:

[1] Kovačević et al. (2024a)

[2] Kovačević et al. (2025a)

[3] Kovačević et al. (2024b)

[4] Langner and Kovačević et al. (2025)

[5] Kovačević et al. (2025b)

Relation between the publications and dissertation chapters:

Chapter	Publications
Chapters 1 - 2, 6	[1], [2], [5]
Chapter 3	[1], [2]
Chapter 4	[3], [4]
Chapter 5	[5]
Appendix	[1], [3], [4], [5]

List of supervised theses

Master theses

Jadzia Brecher. Investigation of the Effects of Model Simplification in the Modeling of Heat Pump Systems in Modelica. Master's thesis, Karlsruhe Institute of Technology, 2024.

Salome Hohl. Untersuchung der Sektorkopplung Wärme und Strom in einer modularen Co-Simulation auf Grundlage realer Experimentalgebäude des Energy Lab 2.0 und deren Komponenten der Technischen Gebäudeausrüstung. Master's thesis, Karlsruhe Institute of Technology, 2023.

Niels Modry. Integrating Model Predictive and Fuzzy Control Systems for Thermal Building Control. Master's thesis, Karlsruhe Institute of Technology, 2025.

Eliott Samuel. Optimization of energy management in a multi-building microgrid with combined battery-hydrogen storage using a hybrid MPC and Fuzzy Logic approach. Master's thesis, Karlsruhe Institute of Technology, 2026.

Bibliography

Marwan Abugabbara, Jonas Lindhe, Saqib Javed, Hans Bagge, and Dennis Johansson. Modelica-based simulations of decentralised substations to support decarbonisation of district heating and cooling. *Energy Reports*, 7:465–472, 2021. doi: 10.1016/j.egyr.2021.08.081.

Canan Acar, Ercan Erturk, and Irem Firtina-Ertis. Performance analysis of a stand-alone integrated solar hydrogen energy system for zero energy buildings. *International Journal of Hydrogen Energy*, 48(5):1664–1684, 2023. doi: 10.1016/j.ijhydene.2022.10.051.

Zakia Afroz, GM Shafiullah, Tania Urmee, and Gary Higgins. Modeling techniques used in building HVAC control systems: A review. *Renewable and sustainable energy reviews*, 83: 64–84, 2018. doi: 10.1016/j.rser.2017.10.044.

Carsten Agert, Alexander Dyck, Nadine Jacobs, Patrick Jochem, Michael Kröner, Karsten von Maydell, Sunke Schlüters, Frank Schuldt, Martin Vehse, Manuel Dahmen, Sonja Germscheid, Alexander Mitsos, Maximilian Mork, Dirk Müller, Ariana Ojeda, André Xhonneux, Moritz Frahm, Karl-Heinz Häfele, Veit Hagenmeyer, Jörg Matthes, and Markus Vogelbacher. Technical report on the flexibility potentials and solutions of buildings, districts, transport, and energy-intensive industries. Technical report, Helmholtz, 2023. URL `https://energy.helmholtz.de/assets/energy/user_upload/Bericht_zu_Flexibilit%C3%A4tspotenzialen.pdf`.

Mohammed Jasim M Al Essa. Home energy management of thermostatically controlled loads and photovoltaic-battery systems. *Energy*, 176:742–752, 2019. doi: 10.1016/j.energy.2019.04.041.

Ismail H. Altas. Fuzzy logic control in energy systems with design applications in MatLab/Simulink. Technical report, IET, 2017.

V. Amato, R.E. Hedegaard, M.D. Knudsen, and S. Petersen. Room-level load shifting of space heating in a single-family house–A field experiment. *Energy and Buildings*, 281:112750, 2023. doi: 10.1016/j.enbuild.2022.112750.

Tatiana Santos Andrade, Sindhu Kanya Nalini Ramakrishna, and Torbjörn Thiringer. Integrating a fuel cell with a heat pump: An energy-saving system for residential housing. *Energy Conversion and Management*, 326, 2025. doi: 10.1016/j.enconman.2025.119509.

Carlos Andrade-Cabrera, Mattia De Rosa, Anjukan Kathirgamanathan, Dimitrios-Stavros Kapetanakis, and Donal Finn. A study on the trade-off between energy forecasting accuracy and computational complexity in lumped parameter building energy models, 2018.

Krzysztof Arendt, Muhyiddine Jradi, Hamid Reza Shaker, and Christian Veje. Comparative analysis of white-, gray-and black-box models for thermal simulation of indoor environment: Teaching building case study. In *Proceedings of the 2018 Building Performance Modeling Conference and SimBuild co-organized by ASHRAE and IBPSA-USA, Chicago, IL, USA*, pages 26–28, 2018.

aWATTar GmbH. Electricity tariff with hourly price adjustment. URL `https://www.awattar.at/`. Last accessed: June 2, 2025.

Gaby Baasch, Paul Westermann, and Ralph Evins. Identifying whole-building heat loss coefficient from heterogeneous sensor data: An empirical survey of gray and black box approaches. *Energy and Buildings*, 241:110889, 2021. doi: 10.1016/j.enbuild.2021.110889.

Yasaman Balali, Adrian Chong, Andrew Busch, and Steven O'Keefe. Energy modelling and control of building heating and cooling systems with data-driven and hybrid models—A review. *Renewable and Sustainable Energy Reviews*, 183:113496, 2023. doi: 10.1016/j.rser.2023.113496.

Anaïs Berkes and Srinivasan Keshav. SOPEVS: Sizing and Operation of PV-EV-Integrated Modern Homes. In *Proceedings of the 15th ACM International Conference on Future and Sustainable Energy Systems*, pages 14–26, 2024. doi: 10.1145/3632775.3661941.

Piero Bevilacqua. The effectiveness of green roofs in reducing building energy consumptions across different climates. A summary of literature results. *Renewable and Sustainable Energy Reviews*, 151:111523, 2021. doi: 10.1016/j.rser.2021.111523.

Max Bird, Camille Daveau, Edward O'Dwyer, Salvador Acha, and Nilay Shah. Real-world implementation and cost of a cloud-based MPC retrofit for HVAC control systems in commercial buildings. *Energy and Buildings*, 270:112269, 2022. doi: 10.1016/j.enbuild.2022.112269.

Ali Rifat Boynuegri and Burak Tekgun. Real-time energy management in an off-grid smart home: Flexible demand side control with electric vehicle and green hydrogen production. *International Journal of Hydrogen Energy*, 48(60):23146–23155, 2023. doi: 10.1016/j.ijhydene.2023.01.239.

Jadzia Brecher. Investigation of the Effects of Model Simplification in the Modeling of Heat Pump Systems in Modelica. Master's thesis, Karlsruhe Institute of Technology, 2024.

Thea Hauge Broholt, Michael Dahl Knudsen, and Steffen Petersen. The robustness of black and grey-box models of thermal building behaviour against weather changes. *Energy and Buildings*, 275:112460, 2022. doi: 10.1016/j.enbuild.2022.112460.

Bundesnetzagentur. Remuneration for electricity fed into the grid. URL https://www.bundesnetzagentur.de/DE/Fachthemen/ElektrizitaetundGas/ErneuerbareEnergien/EEG_Foerderung/start.html. Last accessed: June 12, 2025.

Giorgio Cau, Daniele Cocco, Mario Petrollese, Søren Knudsen Kær, and Christian Milan. Energy management strategy based on short-term generation scheduling for a renewable microgrid using a hydrogen storage system. *Energy Conversion and Management*, 87:820–831, 2014. doi: 10.1016/j.enconman.2014.07.078.

Yongbao Chen, Zhisen Chen, Zhe Chen, and Xiaolei Yuan. Dynamic modeling of solar-assisted ground source heat pump using Modelica. *Applied Thermal Engineering*, 196:117324, 2021. doi: 10.1016/j.applthermaleng.2021.117324.

John Clauß, Johannes Brozovsky, and Laurent Georges. Demonstrating the load-shifting potential of a schedule-based control in a real-life educational building. *Energy and Buildings*, 316: 114321, 2024. doi: 10.1016/j.enbuild.2024.114321.

Austin R. Coffman and Prabir Barooah. Simultaneous identification of dynamic model and occupant-induced disturbance for commercial buildings. *Building and Environment*, 128: 153–160, 2018. doi: 10.1016/j.buildenv.2017.10.020.

Borui Cui, Cheng Fan, Jeffrey Munk, Ning Mao, Fu Xiao, Jin Dong, and Teja Kuruganti. A hybrid building thermal modeling approach for predicting temperatures in typical, detached, two-story houses. *Applied energy*, 236:101–116, 2019. doi: 10.1016/j.apenergy.2018.11.077.

Jacques A. de Chalendar, Aditya Keskar, Jeremiah X. Johnson, and Johanna L. Mathieu. Living laboratories can and should play a greater role to unlock flexibility in United States commercial buildings. *Joule*, 8(1):13–28, 2024. doi: 10.1016/j.joule.2023.11.009.

Roel De Coninck, Fredrik Magnusson, Johan Åkesson, and Lieve Helsen. Toolbox for development and validation of grey-box building models for forecasting and control. *Journal of building performance simulation*, 9(3):288–303, 2016. doi: 10.1080/19401493.2015.1046933.

Thomas Dengiz, Patrick Jochem, and Wolf Fichtner. Demand response with heuristic control strategies for modulating heat pumps. *Applied Energy*, 238:1346–1360, 2019. doi: 10.1016/j.apenergy.2018.12.008.

Franck Dernoncourt. Introduction to fuzzy logic. *Massachusetts institute of technology*, 21(3): 50–56, 2013.

Deutscher Wetterdienst - DWD. German Weather Service. URL `https://www.wetterdienst.de/`. Last accessed: June 2, 2025.

Paul E. Dodds, Iain Staffell, Adam D. Hawkes, Francis Li, Philipp Grünewald, Will McDowall, and Paul Ekins. Hydrogen and fuel cell technologies for heating: A review. *International Journal of Hydrogen Energy*, 40(5):2065–2083, 2015. doi: 10.1016/j.ijhydene.2014.11.059.

Ján Drgoňa, Javier Arroyo, Iago Cupeiro Figueroa, David Blum, Krzysztof Arendt, Donghun Kim, Enric Perarnau Ollé, Juraj Oravec, Michael Wetter, Draguna L. Vrabie, et al. All you need to know about model predictive control for buildings. *Annual Reviews in Control*, 50: 190–232, 2020. doi: 10.1016/j.arcontrol.2020.09.001.

A. Can Duman, Hamza Salih Erden, Ömer Gönül, and Önder Güler. A home energy management system with an integrated smart thermostat for demand response in smart grids. *Sustainable Cities and Society*, 65:102639, 2021. doi: 10.1016/j.scs.2020.102639.

Harikishan R. Ellamla, Iain Staffell, Piotr Bujlo, Bruno G. Pollet, and Sivakumar Pasupathi. Current status of fuel cell based combined heat and power systems for residential sector. *Journal of Power Sources*, 293:312–328, 2015. doi: 10.1016/j.jpowsour.2015.05.050.

Luca Esposito, Mark Van Der Wiel, and Canan Acar. Hydrogen storage solutions for residential heating: A thermodynamic and economic analysis with scale-up potential. *International Journal of Hydrogen Energy*, 79:579–593, 2024. doi: 10.1016/j.ijhydene.2024.06.279.

Poul O Fanger. Thermal comfort. analysis and applications in environmental engineering., 1970.

Hooman Farzaneh. Energy systems modeling. *Energy Systems Modeling; Springer: Singapore*, 2019. doi: 10.1007/978-981-13-6221-7.

Irem Firtina-Ertis, Canan Acar, and Ercan Erturk. Optimal sizing design of an isolated stand-alone hybrid wind-hydrogen system for a zero-energy house. *Applied Energy*, 274:115244, 2020. doi: 10.1016/j.apenergy.2020.115244.

Tom Fletcher, Rob Thring, and Martin Watkinson. An Energy Management Strategy to concurrently optimise fuel consumption & PEM fuel cell lifetime in a hybrid vehicle. *International Journal of Hydrogen Energy*, 41(46):21503–21515, 2016. doi: 10.1016/j.ijhydene.2016.08.157.

Moritz Frahm, Felix Langner, Philipp Zwickel, Jörg Matthes, Ralf Mikut, and Veit Hagenmeyer. How to Derive and Implement a Minimalistic RC Model from Thermodynamics for the Control of Thermal Parameters for Assuring Thermal Comfort in Buildings. In *2022 Open Source Modelling and Simulation of Energy Systems (OSMSES)*, pages 1–6. IEEE, 2022a. doi: 10.1109/OSMSES54027.2022.9769134.

Moritz Frahm, Stefan Meisenbacher, Elena Klumpp, Ralf Mikut, Jörg Matthes, and Veit Hagenmeyer. Multi-zone grey-box thermal building identification with real occupants. In *Proceedings of the 9th ACM International Conference on Systems for Energy-Efficient Buildings, Cities, and Transportation*, pages 484–487, 2022b. doi: 10.1145/3563357.3567403.

Moritz Frahm, Thomas Dengiz, Philipp Zwickel, Heiko Maaß, Jörg Matthes, and Veit Hagenmeyer. Occupant-oriented demand response with multi-zone thermal building control. *Applied Energy*, 347:121454, 2023. doi: 10.1016/j.apenergy.2023.121454.

Peter Fritzson. *Principles of object-oriented modeling and simulation with Modelica 3.3: a cyber-physical approach*. John Wiley & Sons, 2015. doi: 10.1002/9781118989166.

Marta Gandiglio, Andrea Lanzini, Massimo Santarelli, and Pierluigi Leone. Design and optimization of a proton exchange membrane fuel cell CHP system for residential use. *Energy and Buildings*, 69:381–393, 2014. doi: 10.1016/j.enbuild.2013.11.022.

Hao Gao, Christian Koch, and Yupeng Wu. Building information modelling based building energy modelling: A review. *Applied energy*, 238:320–343, 2019. doi: 10.1016/j.apenergy.2019.01.032.

Linas Gelazanskas and Kelum A.A. Gamage. Demand side management in smart grid: A review and proposals for future direction. *Sustainable Cities and Society*, 11:22–30, 2014. doi: 10.1016/j.scs.2013.11.001.

Clark W. Gellings. The concept of demand-side management for electric utilities. *Proceedings of the IEEE*, 73(10):1468–1470, 1985. doi: 10.1109/PROC.1985.13318.

German Environment Agency. Ökodesign-Richtlinie und Energieverbrauchskennzeichnung1. URL `https://www.umweltbundesamt.de/sites/default/files/medien/376/dokumente/oekodesignrichtlinie_und_energieverbrauchskennzeichnung_warmwasserbereiter.pdf`. Last accessed: June 1, 2025.

Michael Anthony Giovanniello and Xiao-Yu Wu. Hybrid lithium-ion battery and hydrogen energy storage systems for a wind-supplied microgrid. *Applied Energy*, 345:121311, 2023. doi: 10.1016/j.apenergy.2023.121311.

Jaehyun Go, Jiwook Byun, Kristina Orehounig, and Yeonsook Heo. Battery-H2 storage system for self-sufficiency in residential buildings under different electric heating system scenarios. *Applied Energy*, 337:120742, 2023. doi: 10.1016/j.apenergy.2023.120742.

Hessam Golmohamadi, Kim Guldstrand Larsen, Peter Gjøl Jensen, and Imran Riaz Hasrat. Optimization of power-to-heat flexibility for residential buildings in response to day-ahead electricity price. *Energy and buildings*, 232:110665, 2021. doi: 10.1016/j.enbuild.2020.110665.

Francesco Massa Gray and Michael Schmidt. Thermal building modelling using Gaussian processes. *Energy and Buildings*, 119:119–128, 2016. doi: 10.1016/j.enbuild.2016.02.004.

Francesco Massa Gray and Michael Schmidt. A hybrid approach to thermal building modelling using a combination of Gaussian processes and grey-box models. *Energy and Buildings*, 165:56–63, 2018. doi: 10.1016/j.enbuild.2018.01.039.

Gurobi Optimization LLC. Gurobi. URL `https://docs.gurobi.com/current/`. Last accessed: October 10, 2025.

Sascha Hammes, Philipp Zech, David Geisler-Moroder, Johannes Weninger, Gernot Steindl, Martin Hauer, Josef Miller, and Rainer Pfluger. Ten questions concerning building information modeling (bim): Energy-efficiency in design, construction, and operation. *Building and Environment*, 296:114497, 2026. doi: https://doi.org/10.1016/j.buildenv.2026.114497.

Hassan Harb, Neven Boyanov, Luis Hernandez, Rita Streblow, and Dirk Müller. Development and validation of grey-box models for forecasting the thermal response of occupied buildings. *Energy and Buildings*, 117:199–207, 2016. doi: 10.1016/j.enbuild.2016.02.021.

Ion Hazyuk, Christian Ghiaus, and David Penhouet. Optimal temperature control of intermittently heated buildings using Model Predictive Control: Part I–Building modeling. *Building and Environment*, 51:379–387, 2012. doi: 10.1016/j.buildenv.2011.11.009.

Tianzhen Hong, Da Yan, Simona D'Oca, and Chien-fei Chen. Ten questions concerning occupant behavior in buildings: The big picture. *Building and Environment*, 114:518–530, 2017. doi: 10.1016/j.buildenv.2016.12.006.

Horizon Fuel Cell Europe, s.r.o. Horizon Educational. URL `https://www.horizoneducational.com/`. Last accessed: June 20, 2025.

Guoqing Hu and Fengqi You. Multi-zone building control with thermal comfort constraints under disjunctive uncertainty using data-driven robust model predictive control. *Advances in Applied Energy*, 9:100124, 2023. doi: 10.1016/j.adapen.2023.100124.

Pengmin Hua, Haichao Wang, Zichan Xie, and Risto Lahdelma. Integrated demand response method for heating multiple rooms based on fuzzy logic considering dynamic price. *Energy*, 307:132577, 2024. doi: 10.1016/j.energy.2024.132577.

IEA. A Summary of IEA Annexes 16 and 17 - Building Energy Management Systems. `https://www.iea-ebc.org/Data/publications/EBC_Annex_16-17_tsr.pdf`, 1997. Last accessed: December 4, 2025.

IEA. IEA EBC - Annex 82. `https://annex82.iea-ebc.org/`, 2025a. Last accessed: November 17, 2025.

IEA. `https://www.iea.org/energy-system/buildings/heating`, 2025b. Last accessed: November 17, 2025.

ISO 7730. *Ergonomics of the Thermal Environment-Analytical Determination and Interpretation of Thermal Comfort Using Calculation of the PMV and PPD Indices and Local Thermal Comfort Criteria*. International Organization for Standardization, 2025.

Mohammad Sadegh Javadi, Matthew Gough, Mohamed Lotfi, Ali Esmaeel Nezhad, Sérgio F. Santos, and João P.S. Catalão. Optimal self-scheduling of home energy management system in the presence of photovoltaic power generation and batteries. *Energy*, 210:118568, 2020. doi: 10.1016/j.energy.2020.118568.

Z. Jiang, Q. Chen, and A. Moser. Indoor airflow with cooling panel and radiative/convective heat source., 1992.

Jaewan Joe. Investigation on pre-cooling potential of UFAD via model-based predictive control. *Energy and Buildings*, 259:111898, 2022. doi: 10.1016/j.enbuild.2022.111898.

Ulrike Jordan and Klaus Vajen. DHWcalc: Program to generate domestic hot water profiles with statistical means for user defined conditions. In *Proceedings of the ISES Solar World Congress*, 2005. URL `https://api.semanticscholar.org/CorpusID:56888001`.

Filip Jorissen, Glenn Reynders, Ruben Baetens, Damien Picard, Dirk Saelens, and Lieve Helsen. Implementation and Verification of the IDEAS Building Energy Simulation Library. *Journal of Building Performance Simulation*, 11:669–688, 2018. doi: 10.1080/19401493.2018.1428361.

Amirreza Kaabinejadian, Artur Pozarlik, and Canan Acar. A systematic review of predictive, optimization, and smart control strategies for hydrogen-based building heating systems. *Applied Energy*, 379:124994, 2025. doi: 10.1016/j.apenergy.2024.124994.

Dulakshi Santhusitha Kumari Karunasingha. Root mean square error or mean absolute error? Use their ratio as well. *Information Sciences*, 585:609–629, 2022. doi: 10.1016/j.ins.2021.11.036.

Azim Keshtkar, Siamak Arzanpour, Fazel Keshtkar, and Pouria Ahmadi. Smart residential load reduction via fuzzy logic, wireless sensors, and smart grid incentives. *Energy and buildings*, 104:165–180, 2015. doi: 10.1016/j.enbuild.2015.06.068.

Ummul Khair, Hasanul Fahmi, Sarudin Al Hakim, and Robbi Rahim. Forecasting error calculation with mean absolute deviation and mean absolute percentage error. In *journal of physics: conference series*, volume 930, page 012002. IOP Publishing, 2017. doi: 10.1088/1742-6596/930/1/012002.

M. Killian, B. Mayer, and M. Kozek. Cooperative fuzzy model predictive control for heating and cooling of buildings. *Energy and Buildings*, 112:130–140, 2016. doi: 10.1016/j.enbuild.2015.12.017.

Peter Klanatsky, François Veynandt, and Christian Heschl. Grey-box model for model predictive control of buildings. *Energy and Buildings*, 300:113624, 2023. doi: 10.1016/j.enbuild.2023.113624.

Kevin Knosala, Lukas Langenberg, Noah Pflugradt, Peter Stenzel, Leander Kotzur, and Detlef Stolten. The role of hydrogen in German residential buildings. *Energy and Buildings*, 276:112480, 2022. doi: 10.1016/j.enbuild.2022.112480.

Michael Dahl Knudsen, Laurent Georges, Kristian Stenerud Skeie, and Steffen Petersen. Experimental test of a black-box economic model predictive control for residential space heating. *Applied energy*, 298:117227, 2021. doi: 10.1016/j.apenergy.2021.117227.

Rok Lacko, Boštjan Drobnič, Mihael Sekavčnik, and Mitja Mori. Hydrogen energy system with renewables for isolated households: The optimal system design, numerical analysis and experimental evaluation. *Energy and Buildings*, 80:106–113, 2014. doi: 10.1016/j.enbuild.2014.04.009.

Felix Langner, Weimin Wang, Moritz Frahm, and Veit Hagenmeyer. Model predictive control of distributed energy resources in residential buildings considering forecast uncertainties. *Energy and Buildings*, 303, 2024. doi: 10.1016/j.enbuild.2023.113753.

Tay Son Le, Tuan Ngoc Nguyen, Dac-Khuong Bui, and Tuan Duc Ngo. Optimal sizing of renewable energy storage: A techno-economic analysis of hydrogen, battery and hybrid systems considering degradation and seasonal storage. *Applied Energy*, 336:120817, 2023. doi: 10.1016/j.apenergy.2023.120817.

J. Le Dréau and P. Heiselberg. Energy flexibility of residential buildings using short term heat storage in the thermal mass. *Energy*, 111:991–1002, September 2016. doi: 10.1016/j.energy.2016.05.076.

LG Electronics. Therma V Monobloc HM051M U43. URL `https://www.lg.com/de/klimaanlagen/hm051m/`. Last accessed: March 2, 2026.

Chang Li. *The Influence of Model Complexity on Demand Side Management with Distributed Energy Resources*. PhD thesis, Karlsruhe Institute Of Technology (KIT), 2026.

Rongling Li, Andrew J Satchwell, Donal Finn, Toke Haunstrup Christensen, Michaël Kummert, Jérôme Le Dréau, Rui Amaral Lopes, Henrik Madsen, Jaume Salom, Gregor Henze, et al. Ten questions concerning energy flexibility in buildings. *Building and Environment*, 223:109461, 2022a. doi: 10.1016/j.buildenv.2022.109461.

Wei Li, Jili Zhang, Tianyi Zhao, and Jiankang Ren. Experimental study of an indoor temperature fuzzy control method for thermal comfort and energy saving using wristband device. *Building and Environment*, 187:107432, 2021a. doi: 10.1016/j.buildenv.2020.107432.

Yanfei Li, Zheng O'Neill, Liang Zhang, Jianli Chen, Piljae Im, and Jason DeGraw. Grey-box modeling and application for building energy simulations-A critical review. *Renewable and Sustainable Energy Reviews*, 146:111174, 2021b. doi: 10.1016/j.rser.2021.111174.

Yantong Li, Natasa Nord, Henrik Halvorsen, and Inge Håvard Rekstad. Model-based sizing of a CO2 heat pump for residential use. *Sustainable Energy Technologies and Assessments*, 53: 102592, 2022b. doi: 10.1016/j.seta.2022.102592.

Fei Lu, Zhenyu Yu, Yu Zou, and Xudong Yang. Cooling system energy flexibility of a nearly zero-energy office building using building thermal mass: Potential evaluation and parametric analysis. *Energy and Buildings*, 236:110763, 2021. doi: 10.1016/j.enbuild.2021.110763.

Fengji Luo, Gianluca Ranzi, and Zhao Yang Dong. *Chapter 5 - Building energy management systems*. Elsevier, 2024. doi: 10.1016/B978-0-323-96107-3.00005-9.

Alessandro Maccarini, Artem Sotnikov, Tobias Sommer, Michael Wetter, Matthias Sulzer, and Alireza Afshari. Influence of building heat distribution temperatures on the energy performance and sizing of 5th generation district heating and cooling networks. *Energy*, 275:127457, 2023. doi: 10.1016/j.energy.2023.127457.

Henrik Madsen and Jan Holst. Estimation of continuous-time models for the heat dynamics of a building. *Energy and buildings*, 22(1):67–79, 1995. doi: 10.1016/0378-7788(94)00904-X.

Laura Maier, David Jansen, Fabian Wüllhorst, Martin Kremer, Alexander Kümpel, Tobias Blacha, and Dirk Müller. AixLib: an open-source Modelica library for compound building energy systems from component to district level with automated quality management. *Journal of Building Performance Simulation*, 17(2):196–219, 2024. doi: 10.1080/19401493.2023.2250521.

Mamdani. Application of fuzzy logic to approximate reasoning using linguistic synthesis. *IEEE transactions on computers*, 100(12):1182–1191, 1977. doi: 10.1109/TC.1977.1674779.

D. Mariano-Hernández, L. Hernández-Callejo, A. Zorita-Lamadrid, O. Duque-Pérez, and F. Santos García. A review of strategies for building energy management system: Model predictive control, demand side management, optimization, and fault detect & diagnosis. *Journal of Building Engineering*, 33:101692, 2021. doi: 10.1016/j.jobe.2020.101692.

Anita Martinčević, Mario Vašak, and Vinko Lešić. Model predictive control for energy-saving and comfortable temperature control in buildings. In *2016 24th Mediterranean Conference on Control and Automation (MED)*, pages 298–303. IEEE, 2016. doi: 10.1109/MED.2016.7536001.

Antonio José Gil Mena, Abderraouf Bouakkaz, José María Abelleira Pereira, Luis Segovia Guerrero, and Maria de la Luz Martin Rodriguez. Collective hydrogen stand-alone renewable energy systems for buildings in Spain. Towards the self-sufficiency. *International Journal of Hydrogen Energy*, 72:1274–1286, 2024. doi: 10.1016/j.ijhydene.2024.05.438.

Jan Meyer. Effiziente Wärmepumpe. `https://www.effiziente-waermepumpe.ch/`, 2013. Last accessed: October 24, 2025.

Piotr Michalak. The development and validation of the linear time varying Simulink-based model for the dynamic simulation of the thermal performance of buildings. *Energy and Buildings*, 141:333–340, 2017. doi: 10.1016/j.enbuild.2017.02.047.

Maximilian Mork, André Xhonneux, and Dirk Müller. Nonlinear Distributed Model Predictive Control for multi-zone building energy systems. *Energy and Buildings*, 264:112066, 2022. doi: 10.1016/j.enbuild.2022.112066.

Gabriel Naumann, Elke Schropp, Natascha Steegmann, Marius C Möller, and Matthias Gaderer. Environmental performance of a hybrid solar-hydrogen energy system for buildings. *International Journal of Hydrogen Energy*, 49:1185–1199, 2024. doi: 10.1016/j.ijhydene.2023.07.208.

Huy Quoc Nguyen and Bahman Shabani. Proton exchange membrane fuel cells heat recovery opportunities for combined heating/cooling and power applications. *Energy Conversion and Management*, 204, 2020. doi: 10.1016/j.enconman.2019.112328.

NIBE Systemtechnik GmbH. `https://www.nibe.eu/de-de/support/handbuecher/`. Last accessed: February 16, 2026.

NKON B.V. PYLONTECH US5000-1C 48V 4.8kWh Home Battery. URL `https://www.nkon.nl/en/pylontech-us-5000-48-v.html`. Last accessed: August 8, 2025.

Christoph Nytsch-Geusen, Jörg Huber, Manuel Ljubijankic, and Jörg Rädler. Modelica BuildingSystems- eine Modellbibliothek zur Simulation komplexer energietechnischer Gebäudesysteme. *Bauphysik*, 35(1):21–29, 2013. doi: 10.1002/bapi.201310045.

Si-Doek Oh, Ki-Young Kim, Shuk-Bum Oh, and Ho-Young Kwak. Optimal operation of a 1-kW PEMFC-based CHP system for residential applications. *Applied Energy*, 95:93–101, 2012. doi: 10.1016/j.apenergy.2012.02.019.

Kai Ou, Wei-Wei Yuan, and Young-Bae Kim. Development of optimal energy management for a residential fuel cell hybrid power system with heat recovery. *Energy*, 219:119499, 2021. doi: 10.1016/j.energy.2020.119499.

José Eduardo Pachano, Cristina Nuevo-Gallardo, and Carlos Fernández Bandera. An empirical comparison of a calibrated white-box versus multiple LSTM black-box building energy models. *Energy and Buildings*, 333, 2025. doi: 10.1016/j.enbuild.2025.115485.

Peter Palensky, Arjen A. Van Der Meer, Claudio David Lopez, Arun Joseph, and Kaikai Pan. Cosimulation of intelligent power systems: Fundamentals, software architecture, numerics, and coupling. *IEEE Industrial Electronics Magazine*, 11(1):34–50, 2017. doi: 10.1109/MIE.2016.2639825.

Linda R Petzold. Description of DASSL: a differential/algebraic system solver. Technical report, Sandia National Labs., Livermore, CA (USA), 1982.

Noah Pflugradt, Peter Stenzel, Leander Kotzur, and Detlef Stolten. Loadprofilegenerator: An agent-based behavior simulation for generating residential load profiles. *Journal of Open Source Software*, 7(71):3574, 2022. doi: 10.21105/joss.03574.

Henrik Pieper, Torben Ommen, Jonas Kjær Jensen, Brian Elmegaard, and Wiebke Brix Markussen. Comparison of COP estimation methods for large-scale heat pumps used in energy planning. *Energy*, 205:117994, 2020. doi: 10.1016/j.energy.2020.117994.

Stewart Robinson. Exploring the relationship between simulation model accuracy and complexity. *Journal of the Operational Research Society*, 74(9):1992–2011, 2023. doi: 10.1080/01605682.2022.2122740.

Ahmad Rouhani, Hossein Kord, and Mahdi Mehrabi. A comprehensive method for optimum sizing of hybrid energy systems using intelligence evolutionary algorithms. *Indian Journal of Science and Technology*, 6(6):4702–4712, 2013. doi: 10.17485/ijst/2013/v6i6.3.

Roozbeh Sangi, Pooyan Jahangiri, Freerk Klasing, Rita Streblow, and Dirk Müller. A medium model for the refrigerant propane for fast and accurate dynamic simulations. In *Proceedings of the 10th International Modelica Conference*, pages 1271–1275, 2014. doi: 10.3384/ECP140961271.

Domina Cikatić Šanić and Frano Barbir. Stand-alone micro-trigeneration system coupling electrolyzer, fuel cell, and heat pump with renewables. *International Journal of Hydrogen Energy*, 47(82):35068–35080, 2022. doi: 10.1016/j.ijhydene.2022.08.090.

Georg Ferdinand Schneider, Georg Ambrosius Peßler, and Simone Steiger. Modelling and simulation of standardised control functions from building automation. In *Modelica*, pages 132–021, 2017. doi: 10.3384/ecp17132209.

Pierluigi Siano. Demand response and smart grids—A survey. *Renewable and sustainable energy reviews*, 30:461–478, 2014. doi: 10.1016/j.rser.2013.10.022.

J. Sievers, P. Henrich, M. Beichter, R. Mikut, V. Hagenmeyer, T. Blank, and F. Simon. Federated reinforcement learning for sustainable and cost-efficient energy management. *Energy and AI*, 21:100521, 2025. doi: 10.1016/j.egyai.2025.100521.

P. Simpa, N.O. Solomon, O.A. Adenekan, and S.C. Obasi. The safety and environmental impacts of battery storage systems in renewable energy. *World Journal of Advanced Research and Reviews*, 22(2):564–580, 2024. doi: 10.30574/wjarr.2024.22.2.1398.

Smart Energy Tariff | tado°. URL `https://www.tado.com/en/energy/smart-energy-tariff`. Last accessed: February 20, 2025.

Bjorn Sohlberg. *Supervision and control for industrial processes: using grey box models, predictive control and fault detection methods*. Springer Science & Business Media, 2012. doi: 10.1007/978-1-4471-1558-8_2.

Rok Stropnik, Nejc Mlakar, Andrej Lotrič, Mihael Sekavčnik, and Mitja Mori. The influence of degradation effects in proton exchange membrane fuel cells on life cycle assessment modelling and environmental impact indicators. *International Journal of Hydrogen Energy*, 47(57): 24223–24241, 2022. doi: 10.1016/j.ijhydene.2022.04.011.

Suissetec. Fresh Water Stations. URL `https://merkblatt.suissetec.ch/de-CH/ALLE222/file/ALLE222.pdf`. Last accessed: July 28, 2025.

D Sundararajan. *Control Systems*. Springer, 2022. doi: 10.1007/978-3-030-98445-8.

Tomohiro Takagi and Michio Sugeno. Fuzzy identification of systems and its applications to modeling and control. *IEEE transactions on systems, man, and cybernetics*, SMC-15(1): 116–132, 1985. doi: 10.1109/TSMC.1985.6313399.

Ashkan Talebi and Alireza Hatami. Online fuzzy control of HVAC systems considering demand response and users' comfort. *Energy Sources, Part B: Economics, Planning, and Policy*, 15 (7-9):403–422, 2020. doi: 10.1080/15567249.2020.1825557.

Federico Tartarini, Stefano Schiavon, Toby Cheung, and Tyler Hoyt. CBE Thermal Comfort Tool: Online tool for thermal comfort calculations and visualizations. *SoftwareX*, 12:100563, 2020. doi: 10.1016/j.softx.2020.100563.

The Fuel Cell Store. Hydrogen Fuel Cell Power Generator. URL https://www.fuelcellstore.com/g-hfcs-2kw25v-1kw-hydrogen-fuel-cell-power-generator. Last accessed: August 8, 2025.

The MathWorks Inc. System identification toolbox: 9.16 (R2022a). URL https://www.mathworks.com.

Yahachiro Tsukamoto. An approach to fuzzy reasoning method. *Advances in fuzzy set theory and applications*, 1979.

Tsuyoshi Ueno and Alan Meier. A method to generate heating and cooling schedules based on data from connected thermostats. *Energy and Buildings*, 228:110423, 2020. doi: 10.1016/j.enbuild.2020.110423.

Laura Zabala Urrutia, Sergiu Crisan, Estíbaliz Pérez Iribarren, Iker González Pino, and Jesús Febres Pascual. Evaluating the interoperability of teaser and aixlib for building digital twins within modelon impact environment: A case study. In *Building Digital Twin International Congress*, pages 13–25. Springer, 2025. doi: 10.1007/978-3-032-09040-9_2.

Toon Van Puyvelde, Marie-Sophie Verwee, Gargya Gokhale, Mehran Zareh, and Chris Develder. HomeLabGym: A real-world testbed for home energy management systems. In *Proceedings of the 15th ACM International Conference on Future and Sustainable Energy Systems*, page 478–479. Association for Computing Machinery, 2024. doi: 10.1145/3632775.3661974.

F.J. Vivas, F. Segura, and J.M. Andújar. Fuzzy logic-based energy management system for grid-connected residential DC microgrids with multi-stack fuel cell systems: A multi-objective approach. *Sustainable Energy, Grids and Networks*, 32, 2022. doi: 10.1016/j.segan.2022.100909.

Shibo Wang, Lingguo Kong, Chuang Liu, and Guowei Cai. MPC-based energy optimization and regulation for zero-carbon energy supply building. *International Journal of Hydrogen Energy*, 82:1196–1210, 2024. doi: 10.1016/j.ijhydene.2024.07.397.

Xuezheng Wang and Bing Dong. Long-term experimental evaluation and comparison of advanced controls for HVAC systems. *Applied Energy*, 371:123706, 2024. doi: 10.1016/j.apenergy.2024.123706.

Michael Wetter, Wangda Zuo, Thierry S. Nouidui, and Xiufeng Pang. Modelica Buildings library. *Journal of Building Performance Simulation*, 7(4):253–270, 2014. doi: 10.1080/19401493.2013.765506.

Friedrich Wiegel, Jan Wachter, Michael Kyesswa, Ralf Mikut, Simon Waczowicz, and Veit Hagenmeyer. Smart Energy System Control Laboratory–a fully-automated and user-oriented research infrastructure for controlling and operating smart energy systems. *at-Automatisierungstechnik*, 70(12):1116–1133, 2022. doi: 10.1515/auto-2022-0018.

Brian Woo-Shem, Kaleb Pattawi, Hannah Covington, Patrick McCurdy, Chenli Wang, Thomas Roth, Cuong Nguyen, Yuhong Liu, and Hohyun Lee. Comparing economic benefits of HVAC control strategies in grid-interactive residential buildings. *Energy and Buildings*, 286:112937, 2023. ISSN 0378-7788. doi: 10.1016/j.enbuild.2023.112937.

Shiyu Yang, Man Pun Wan, Wanyu Chen, Bing Feng Ng, and Swapnil Dubey. Experiment study of machine-learning-based approximate model predictive control for energy-efficient building control. *Applied Energy*, 288:116648, 2021. doi: 10.1016/j.apenergy.2021.116648.

Yuchen Yang, Zhen Wu, Jing Yao, Tianlei Guo, Fusheng Yang, Zaoxiao Zhang, Jianwei Ren, Liangliang Jiang, and Bo Li. An overview of application-oriented multifunctional large-scale stationary battery and hydrogen hybrid energy storage system. *Energy Reviews*, 3(2):100068, 2024. doi: 10.1016/j.enrev.2024.100068.

Meysam Yari, Rasool Kalbasi, N.H. Thi, and Masoud Afrand. Incorporating PCMs and thermal insulation into building walls and their competition in building energy consumption reduction. *Case Studies in Thermal Engineering*, 63:105398, 2024. doi: 10.1016/j.csite.2024.105398.

Lotfi A. Zadeh. Fuzzy sets. *Information and Control*, 8(3):338–353, 1965. doi: https://doi.org/10.1016/S0019-9958(65)90241-X.

Lotfi A. Zadeh. Outline of a new approach to the analysis of complex systems and decision processes. *IEEE Transactions on Systems, Man, and Cybernetics*, SMC-3(1):28–44, 1973. doi: 10.1109/TSMC.1973.5408575.

Zhaoyun Zeng, Wanni Zhang, Kaiyu Sun, Max Wei, and Tianzhen Hong. Investigation of pre-cooling as a recommended measure to improve residential buildings' thermal resilience during heat waves. *Building and Environment*, 210:108694, 2022. doi: 10.1016/j.buildenv.2021.108694.

Kun Zhang and Michaël Kummert. Evaluating the impact of thermostat control strategies on the energy flexibility of residential buildings for space heating. In *Building Simulation*, volume 14, pages 1439–1452. Springer, 2021. doi: 10.1007/s12273-020-0751-x.

Xiang Zhang, Christoffer Rasmussen, Dirk Saelens, and Staf Roels. Time-dependent solar aperture estimation of a building: Comparing grey-box and white-box approaches. *Renewable and Sustainable Energy Reviews*, 161:112337, 2022. doi: 10.1016/j.rser.2022.112337.

Xiangjun Zhao, Lan Luo, Qi Zhu, Peixian Li, Maohui Luo, and Xing Shi. Increasing Demand-Response Flexibility for Office Buildings: A Multi-Scenario Strategy Integrating Thermal

Tolerance and Adaptive Behaviors. *Building and Environment*, page 113974, 2025. doi: 10.1016/j.buildenv.2025.113974.

Yalun Zhu, Ming Wang, Dongrun Yang, Mingyuan Wang, Qianchuan Zhao, Xuehan Zheng, and He Gao. Collaborative optimization scheduling strategy for HVAC with a three-layer optimization architecture. *Energy and Buildings*, 335:115565, 2025. doi: 10.1016/j.enbuild.2025.115565.

Statement regarding the use of generative AI in the writing process

During the writing of this thesis, Microsoft Copilot was used to assist with text rephrasing. After using this tool, the content was reviewed and revised as necessary. The author takes full responsibility for the entire content of this work.